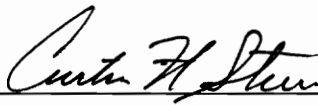


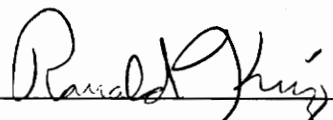
**MODELING THE MICROWAVE FREQUENCY PERMITTIVITY  
OF THERMOPLASTIC COMPOSITE MATERIALS**

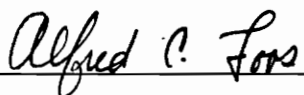
by  
Mitchell L. Jackson

Thesis Submitted to the Faculty of the  
Virginia Polytechnic Institute and State University  
in partial fulfillment of the requirements for the degree of  
Master of Science  
in  
Engineering Mechanics

APPROVED:

  
\_\_\_\_\_  
Dr. Curtis H. Stern, Chairman

  
\_\_\_\_\_  
Dr. Ronald Kriz

  
\_\_\_\_\_  
Dr. Alfred Loos

June 3, 1993  
Blacksburg, Virginia

2

C.2

LD  
5655  
V855  
1993  
J224  
C.2

# MODELING THE MICROWAVE FREQUENCY PERMITTIVITY OF THERMOPLASTIC COMPOSITE MATERIALS

by

Mitchell L. Jackson

Dr. Curtis H. Stern, Chairman

Mechanical Engineering

(ABSTRACT)

Mixture models were studied in an effort to predict the microwave frequency permittivities of unidirectional-fiber-reinforced thermoplastic-matrix composite materials as a function of fiber volume fraction, fiber orientation relative to the electric field, and temperature. The permittivities of the constituent fiber and plastic materials were measured using a resonant cavity perturbation technique at 9.4 GHz and 2.45 GHz. The permittivities of the composite specimens were measured using a reflection cavity technique at 9.4 GHz and 2.45 GHz. Simple "rule-of-mixtures" models that use the fiber and plastic permittivities have been found to approximate the complex dielectric properties of the composite for varied fiber volume fractions. The permittivities of oriented composites were successfully modeled at 9.4 GHz using a tensor rotation procedure. Composite permittivities were modeled with temperature up to the glass transition temperature of the thermoplastic matrix. Good agreement was found between the mixture model and experimental results for permittivity as a function of temperature at 9.4 GHz.

## Acknowledgments

I would like to thank the following people for their help and guidance in conducting this study, preparing this thesis, and enjoying my graduate studies:

Dr. Curtis Stern, who has shown infinite patience in awaiting the completion of this document. His support and encouragement during frustrating times have been invaluable.

Dr. R. Kriz and Dr. A. Loos for serving on my committee, giving me their support, and patiently dealing with my requests. Dr. J. Graybeal, chemistry department, for the generous use of test equipment and facilities. Dr. W. Davis, electrical engineering department, for his helpful instruction and consultation in dealing with the mysteries of electromagnetics. Ken Baker, electrical engineering, for his early experimental assistance. Hal Kimery, ORNL, for his advice and replacement waveguide.

ICI-Fiberite Corporation, Owens Corning, and Mobay Corporation for their generous donation of materials.

The National Science Foundation for funding this research.

My parents Robert G. and Jane A. Jackson for getting me to this point. Their love, support, encouragement, and faith in my abilities have been unceasing.

Brenda Holmes, for typing skills, encouragement skills, and motivational skills, but for her love and devotion most of all. Love and thanks for all of your help.

## TABLE OF CONTENTS

LIST OF FIGURES.....	vii
LIST OF TABLES.....	x
Nomenclature.....	xi
1 INTRODUCTION.....	1
1.1 Aspects of Composite Permittivity Modeling.....	2
1.2 Literature Review.....	3
1.3 Overview.....	7
2 PERMITTIVITY.....	9
2.1 Theory of Structure-Property Relationships.....	9
2.1.1 Polarization .....	9
2.1.2 Complex Permittivity .....	10
2.1.3 Loss Mechanisms in Glass .....	13
2.1.4 Loss Mechanisms in Polymers .....	14
2.1.5 Physical Models of Permittivity and Loss .....	19
2.2 Permittivity Mixture Models.....	23
2.2.1 Layered Dielectric Model .....	23
2.2.2 Averaged Field Model .....	26
2.2.3 Model Comparison and Evaluation .....	32
2.3 Orientation.....	34
2.3.1 The Permittivity Tensor and Orientation ...	34
2.3.2 Experimental Considerations .....	38
3 PERMITTIVITY MEASUREMENT.....	40
3.1 Rectangular Waveguides.....	40
3.1.1 $TE_{mn}$ Modes.....	40
3.1.2 The $TE_{10}$ Mode.....	44
3.2 Cavity Perturbation.....	46
3.2.1 The Empty Lossless Cavity Condition .....	46
3.2.2 Cavity Perturbation .....	48
3.2.3 Resonant Frequency and Q Factor Relationships .....	50
3.2.4 Material Geometry and Field Relationships .....	53
3.3 Reflection Cavity Formulation.....	57

3.3.1	Q Factor Relations .....	57
3.3.2	The TE <sub>103</sub> Cavity .....	60
3.3.3	The Empty Cavity Condition .....	63
3.3.4	The Material Loaded Cavity Condition .....	64
3.3.5	Integration of Field Quantities .....	66
3.3.6	Solution for Permittivity Components .....	72
3.4	Q and Resonant Frequency Measurement.....	78
4	EXPERIMENTAL.....	84
4.1	Equipment.....	84
4.1.1	Network Analyzer System .....	84
4.1.2	Coaxial Waveguides and Cavities .....	86
4.1.3	Heat Sources .....	87
4.1.4	Calibration Standards .....	88
4.2	Procedures.....	88
4.2.1	TRL Calibration Background .....	88
4.2.2	TRL Calibration Procedure .....	90
4.2.3	Materials and Sample Preparation .....	92
4.2.3.1	Orientation .....	93
4.2.3.2	Fiber Volume Fraction .....	93
4.2.4	Cavity Perturbation Technique .....	94
4.2.5	Cavity Perturbation Procedure .....	97
4.2.6	Reflection Cavity Technique .....	98
4.2.7	Experimental Procedure .....	100
5	RESULTS.....	103
5.1	Component Permittivity Computation.....	103
5.2	Results at 9.4 GHz.....	105
5.3	Results at 2.45 GHz.....	109
5.4	Experimental Uncertainty.....	116
6	CONCLUSIONS.....	119
6.1	Conclusions.....	119
6.2	Recommendations for Future Work.....	122
	REFERENCES.....	125
	APPENDIX A.....	131
A.1	Maxwell's Equations and EM Wave Propagation.....	131
A.2	Propagation in Dielectrics.....	135
A.3	Power and Poynting's Theorem.....	139

A.4 Plane Wave Reflection (Normal Incidence).....	141
A.5 Standing Wave Ratio and Input Impedance.....	144
A.6 Transmission Line Theory.....	147
APPENDIX B.....	152
B.1 Reflection Cavity Program.....	152
B.2 Cavity Perturbation Program.....	155
VITA.....	157

## LIST OF FIGURES

Figure 1.1.1: The process of unidirectional-fiber-reinforced composite permittivity modeling and verification.....	4
Figure 2.1.1: Polarization modes.....	12
Figure 2.1.2: Reorientation of a lattice vacancy pair .....	15
Figure 2.1.3: Effect of different dielectric loss mechanisms on $\tan \delta$ at room temperature .....	15
Figure 2.1.4: Schematic diagram of dielectric or mechanical loss at 1 Hz versus normalized temperature.....	16
Figure 2.1.5: Schematic representations of the permittivity as a function of temperature for a model linear polymer over different frequency ranges .....	18
Figure 2.1.6: Approximate frequencies where polarization modes occur in glassy polymers .....	21
Figure 2.2.1: Parallel plate capacitor analogy for permittivity modeling in fiber reinforced composite materials.....	24
Figure 2.2.2: Comparison of complex permittivity mixture models for a unidirectional continuous-fiber-reinforced polymer-matrix composite.....	33
Figure 2.3.1: The rotation of axes through an angle $\theta$ about the normal to the plane of the composite .....	36
Figure 3.1.1: Rectangular waveguide geometry and the $TE_{10}$ electromagnetic field distribution .....	42

Figure 3.2.1: Schematic of the cavity perturbation measurement configuration for a rectangular cavity resonating in the TE <sub>103</sub> mode .....	54
Figure 3.3.1: Schematic of the reflection cavity measurement configuration.....	62
Figure 3.3.2: Network model of the material loaded reflection cavity.....	65
Figure 3.3.3: Impedance matching at the material interface in the reflection cavity.....	74
Figure 3.4.1: Lumped-component circuit model for an inductively coupled resonant cavity.....	79
Figure 3.4.2: Input impedance plotted in the complex plane using frequency as a parameter.....	83
Figure 4.1.1: Schematic of the Hewlett-Packard 8510-B network analyzer and 8515A 2-port S-parameter test set system configuration.....	85
Figure 4.2.1: Apparatus configurations for elevated temperature measurements.....	89
Figure 4.2.2: Temperature correlation curve relating the specimen's surface temperature to the externally measured temperature.....	101
Figure 5.1.1: 9.4 GHz component material Q and f <sub>r</sub> data polynomial fit curves.....	104
Figure 5.2.1: Component material permittivity measured at 9.4 GHz as a function of temperature.....	106
Figure 5.2.2: Model and composite permittivity at 9.4 GHz as a function of temperature.....	108

Figure 5.2.3: Model and composite permittivity at 9.4 GHz as a function of fiber volume fraction.....110

Figure 5.2.4: Model and composite permittivity at 9.4 GHz as a function of fiber orientation.....111

Figure 5.3.1: Component material permittivity at 2.45 GHz as a function of temperature.....112

Figure 5.3.2: Model and composite permittivity at 2.45 GHz as a function of temperature.....113

Figure 5.3.3: Model and composite permittivity at 2.45 GHz as a function of fiber volume fraction.....115

Figure A.1: Current density and electric field vectors with corresponding permittivity and conductivity related components.....140

Figure A.2: Electromagnetic plane wave transmission and reflection from a planar interface.....143

Figure A.3: Section of a lumped element transmission line.....149

## LIST OF TABLES

Table 4.1.1: Cavity Components.....	87
Table 4.2.1: Rectangular Waveguide Data.....	95
Table 5.1.1: Component Material Q and $f_r$ Data Polynomial Fits .....	105

## Nomenclature

A	Arbitrary wave amplitude coefficient
$A_k$	Depolarization factor (Mixture theory)
$A_{mn}$	Amplitude coefficient for the $mn^{\text{th}}$ mode
$a_k$	Orientation angle between the electric field and the included particle axis (Mixture theory)
a	X-direction dimension of a rectangular waveguide
b	Y-direction dimension of a rectangular waveguide
c	Speed of light in free space
C	Capacitance per unit length (Transmission line)
$C_{1,2,i}$	Capacitances of component materials in a mixture
$C_{  }$	Capacitance of dielectrics layered in parallel
$C_{\perp}$	Capacitance of dielectrics layered in series
$\vec{D}$	Electric flux density vector
$\underline{\vec{D}}$	Effective electric flux density vector (Mixture theory)
$D_x$	X-component of the electric flux density
d	Z-direction length of a single period of a mode
$d_{\epsilon}$	Capacitor plate separation distance
$\vec{E}$	Electric field vector
$\vec{E}_s$	Electric field vector in phasor form
$E_x$	X-component of the electric field
$E_{xs}$	X-component of the electric field in phasor form
$E_{x0}$	X-component electric field amplitude coefficient
$E_{xi}$	Incident x-component of the electric field
$\underline{\vec{E}}$	Effective electric field vector (Mixture theory)
$\langle \vec{E}_j \rangle$	Volume averaged electric field over all included particles of the $j^{\text{th}}$ material (Mixture theory)
$\vec{E}_i$	Electric field vector for the $i^{\text{th}}$ cavity condition
$e_p$	Spheroid eccentricity (Mixture theory)
f	Linear frequency
$f_i$	Averaged field ratio (Mixture theory)

$f_{ri}$	Resonant frequency for the $i^{\text{th}}$ cavity condition
$f_c, f_{\text{Cmn}}$	Cutoff frequency (Mode dependent)
$G$	Conductance per unit length (Transmission line)
$\vec{H}$	Magnetic field vector
$\vec{H}_s$	Magnetic field vector in phasor form
$H_T$	Tangential component of the magnetic field
$H_y$	Y-component of the magnetic field
$H_{ys}$	Y-component of the magnetic field in phasor form
$H_{yi}$	Incident y-component of the magnetic field
$\vec{H}_i$	Magnetic field vector for the $i^{\text{th}}$ cavity condition
$h_z(x,y)$	Harmonic function in the xy plane, TE modes
$I$	Current
$I_L$	Complex current flowing through an inductor
$I_s$	Phasor current
$\vec{J}, \vec{J}_s$	Current density vector in phasor form
$\vec{J}_{sc}$	Conduction current density vector in phasor form
$\vec{J}_{sd}$	Displacement current density vector in phasor form
$\vec{J}_{st}$	Total current density vector in phasor form
$\vec{J}_{\text{surf}}$	Surface current density vector
$k$	Complex propagation wavenumber
$\hat{k}$	Solution to the transcendental equation resulting from equating impedances at an interface
$k_B$	Boltzmann's constant
$k_c$	Cutoff wavenumber
$L$	Inductance per unit length (Transmission line)
$l$	Arbitrary reference distance
$l_0$	Length of the empty portion of a loaded cavity
$l_\epsilon$	Dielectric sample thickness
$m, n$	Mode numbers
$m_f$	Mass fraction of fiber in a composite
$m/l_s$	Mass per length of a material strand
$\vec{n}$	Unit normal vector
$\vec{P}$	Polarization field vector
$P_{\text{in}}$	Power input into a cavity

$P_{\text{loss}}$	Power dissipated in a cavity
$P_{\text{e}}$	Power loss in a dielectric occupying a cavity
$P_{\text{w}}$	Power loss in the conductors of the cavity walls
$Q$	General quality factor
$Q_{\text{E}}$	Quality factor for losses to the external circuit
$Q_{\text{L}}$	Quality factor for all losses in a system
$Q_{\text{Li}}$	Quality factor for the losses in a system in the $i^{\text{th}}$ condition
$Q_{\text{U}}$	Quality factor for losses only within a cavity
$Q_{\text{Ui}}$	Quality factor for losses only within a cavity in the $i^{\text{th}}$ condition
$R$	Resistance; Distributed Resistance (Transmission line)
$R_{\text{e}}$	External circuit coupling resistance
$R_{\text{s}}$	Surface resistivity
$s$	Standing wave ratio
$\vec{S}$	Poynting vector; Power flux vector
$S$	Surface area
$S_{\text{c}}$	Surface area of the walls in a resonant cavity
$S_{\text{i}}$	Variables representing the $i^{\text{th}}$ integral in energy calculations in resonant cavities
$S_{\text{I}}$	Cavity wall surface area contacting air in the empty part of a sample loaded cavity
$S_{\text{e}}$	Cavity wall surface area contacting the dielectric sample
$T$	Absolute temperature
$T_{\text{m}}$	Crystal melt temperature in polymers
$T_{\text{g}}$	Glass transition temperature in polymers
$T_{\text{r}}$	Transmission coefficient
$t$	Time
$U_{\text{a}}$	Arrhenius activation energy
$U_{\text{E}}$	Time-averaged energy stored in the electric field
$U_{\text{H}}$	Time-averaged energy stored in the magnetic field
$U_{\text{T}}$	Total average energy in a system

$V$	Voltage
$V_s$	Voltage in phasor form
$V_0$	Voltage amplitude coefficient
$V_c$	Volume of the resonant cavity
$V_D$	Volume of the total dielectric (Mixture theory)
$V_\epsilon$	Volume of an arbitrary dielectric
$V_H$	Volume of the host medium (Mixture theory)
$V_j$	Volume of the $j^{\text{th}}$ inclusion (Mixture theory)
$V/\ell_s$	Volume per length of a material strand
$v_i$	Volume fraction of the $i^{\text{th}}$ component in a mixture
$v_f$	Fiber volume fraction
$X_e$	External circuit coupling susceptance
$x, y, z$	Cartesian coordinate directions
$x_i$	Semi-axes of an ellipsoid (Mixture theory)
$\hat{x}$	Roots of the impedance transcendental equation
$Y^{\text{"in}}$	Input admittance of a parallel LRC circuit
$Z_e$	External circuit coupling impedance
$Z_0$	Characteristic impedance (Transmission line)
$Z_{\text{in}}$	Input impedance (Transmission line)
$Z^{\text{"in}}$	Input impedance of a parallel LRC circuit
$Z_L$	Load impedance (Transmission line)
$Z_{L\text{f}}$	Load impedance looking left at an interface
$Z_R$	Load impedance looking right at an interface
$Z_{r0}$	Characteristic impedance of an empty resonant cavity
$Z_{r1}$	Characteristic impedance of the empty part of a sample loaded resonant cavity
$Z_{\epsilon r1}$	Characteristic impedance of a dielectric sample in a resonant cavity
$Z_{\text{TE}}$	TE mode wave impedance
$z_0$	Reference location along the $z$ axis
$\alpha$	Wave attenuation constant
$\beta$	Wave propagation phase constant
$\beta_0$	Propagation phase constant in free space

$\beta_{r0}$	Propagation phase constant of free space at resonance
$\beta_{r1}$	Propagation phase constant of the empty part of a sample loaded cavity at resonance
$\beta_{\epsilon r1}$	Propagation phase constant of the dielectric sample in a cavity at resonance
$\tan \delta$	Dielectric loss tangent
$\epsilon^*, \epsilon$	Complex permittivity
$\epsilon_0$	Free space permittivity
$[\epsilon^*]$	Complex permittivity tensor
$[\epsilon^*_p]$	Principal complex permittivity tensor
$\epsilon_{xx}$	Permittivity component in a Cartesian tensor
$\epsilon_{\theta 11}$	Rotated permittivity tensor component
$\epsilon'$	Real part of the complex permittivity; Dielectric constant
$\epsilon''$	Imaginary part of the complex permittivity; Dielectric loss factor
$\epsilon''_d$	Dielectric loss due to charge displacement
$\epsilon''_{dp}$	Dielectric loss due to dipole relaxation
$\epsilon''_e$	Dielectric loss due to electron motion
$\epsilon''_a$	Dielectric loss due to atomic distortion
$\epsilon''_{MW}$	Dielectric loss due to Maxwell-Wagner effects
$\epsilon''_{eff}$	Total dielectric loss due to charge displacement and charge conduction
$\epsilon_{r2}$	Relative complex permittivity of cavity condition 2
$\epsilon_s$	Low frequency (static) permittivity
$\epsilon_\infty$	High frequency permittivity
$\epsilon_{  }$	Effective (principal) mixture permittivity for fibers oriented parallel to the electric field
$\epsilon_{\perp}$	Effective (principal) mixture permittivity for fibers oriented perpendicular to the electric field
$\epsilon_{1,2}$	Permittivities of component materials in a mixture
$\epsilon_k$	Isotropic permittivity (Mixture theory)

$\epsilon$	Effective mixture permittivity (Mixture theory)
$\epsilon_H$	Host medium permittivity (Mixture theory)
$\epsilon_m$	Effective medium permittivity external to an inclusion (Mixture theory)
$\epsilon_i$	Permittivity of the $i^{\text{th}}$ cavity condition
$\phi$	Reflection phase shift angle
$\Gamma$	Reflection coefficient
$\gamma, \gamma_1$	Propagation wave number
$\gamma_a$	Particle aspect ratio (Mixture theory)
$\eta, \eta_1$	Complex intrinsic impedance
$\eta_0$	Intrinsic impedance of free space
$\eta_\epsilon$	Intrinsic impedance of a dielectric material
$\eta_{in}$	Input intrinsic impedance
$\lambda$	Wavelength
$\lambda_g$	Guide wavelength
$\lambda_{gr0}$	Guide wavelength in air at resonance
$\mu$	Complex permeability
$\mu_i$	Permeability of the $i^{\text{th}}$ cavity condition
$\mu_0$	Permeability of free space
$\mu_m$	Permeability of metallic waveguide walls
$\nu$	Dipole rotation frequency
$\omega$	Circular frequency
$\omega_0$	Circular resonant frequency
$\omega_i$	Circular frequency of the $i^{\text{th}}$ cavity condition
$\omega'$	Real part of the circular frequency
$\omega'_{ri}$	Real part of the circular resonant frequency for the $i^{\text{th}}$ condition of a cavity
$\omega''$	Imaginary part of the circular frequency
$\omega''_{ri}$	Imaginary part of the circular resonant frequency for the $i^{\text{th}}$ condition of a cavity
$\psi$	Arbitrary phase angle
$\rho$	Density
$\rho_f$	Fiber density
$\rho_{pc}$	Polycarbonate density

$\sigma$	Electrical conductivity
$\sigma_{\epsilon}$	Conductivity of a dielectric material
$\sigma_m$	Electrical conductivity of a metal conductor
$\tau$	Dipole relaxation time constant
$\Delta\tau$	Small time interval
$\theta$	Orientation angle between fiber axes and the electric field

## 1 INTRODUCTION

Great demands upon the advanced materials community for stronger, lighter, corrosion-resistant, economical, and easily processed material systems have created increased interest in fiber-reinforced polymer composites. The major concern facing the emerging composites industry lies in developing cost-effective, reliable, and versatile processing methods. In many cases the critical processing step of heating can be improved by using microwave power. Advantages to microwave heating include reductions in process time due to rapid heating and energy efficiency superior to that of many conventional heating methods [1]. Microwave processing also offers unique advantages in polymeric composites, such as improved fiber-resin interface properties [2] and the potential to process thick sections of material uniformly due to inherent volumetric heating.

With the growing interest in microwave heating of composites, there exists a need to model this process, taking into account the microwave application system, the material, and the interactions between the two. Therefore, it is essential that the electromagnetic constitutive property of the material, the complex permittivity  $\epsilon^*$ , be characterized. This entails modeling the relative complex permittivity  $\epsilon^* = \epsilon' - j\epsilon''$  of the composite mixture with respect to fiber orientation, fiber volume fraction, and temperature. Such a permittivity model will facilitate heat transfer computations and promote understanding of the electric field distribution in the applicator and within the material. The ability to estimate the permittivity will also assist process designers in selecting and modifying materials for optimum heating characteristics.

## 1.1 Aspects of Composite Permittivity Modeling

Prior to modeling the composite, the permittivities of the component fiber and polymer materials must be determined. While some general knowledge of  $\epsilon^*$  for some materials may be obtained from tabulated data, these values must be used carefully. Dielectric properties are functions of frequency, temperature, and moisture content, and can therefore vary greatly between different grades of the same material system. Unfortunately, there are few comprehensive sources of microwave frequency permittivity data and those that do exist seldom delineate between material grades. Very few material suppliers provide microwave frequency dielectric data for specific systems; permittivity data as a function of temperature is very rare. For these reasons a major part of this study was dedicated to constructing a measurement system to determine the complex permittivity of component materials, including the capability of elevated temperature measurements.

In order to consolidate the stacked plies of material, the composite is heated and compacted, traditionally either in a hot press or in a high-pressure autoclave oven. This pressure consolidates the plies and pushes out excess polymer, effectively enhancing the composite's strength-to-weight ratio by leaving more of the stronger fiber component to carry the load. The part of the total material volume that is fiber, known as the fiber volume fraction  $v_f$ , is an important parameter in the permittivity model. In most composites the permittivities of the fiber and polymer matrix are quite different, especially in their dielectric loss characteristics. Permittivity mixture models combine the knowledge of the properties of the component materials and  $v_f$  to predict the composite's permittivity.

Many high-performance composite materials make use of stacked plies of unidirectional-fiber-reinforced polymer in

various orientations to achieve desired mechanical properties. Thus, the permittivity model must account for the orientation of the fibers relative to the components of the electric ( $\vec{E}$ ) field. Once the permittivity of the unidirectional-fiber-reinforced composite is determined in its principal orientations, tensor rotation equations can predict its permittivity at arbitrary fiber orientations. Experimental verification of the permittivity models required the development of a system that could be used to make dielectric measurements of the composites as a function of temperature and fiber orientation. The permittivity modeling process discussed above is diagrammed in the flow chart of Figure 1.1.1.

## 1.2 Literature Review

Efforts to measure and model the permittivity of fiber-reinforced composites at microwave frequencies have increased in recent years. These efforts are attributable in large part to "stealth technology" research for high performance aircraft and other military applications. In a recent review of "stealth" composite technology, Stonier [3] provided room temperature microwave frequency (10 GHz) complex permittivity data for a variety of reinforcing fibers, common thermoset and thermoplastic matrix resins, and selected composites of these components. The permittivity data for some of the component materials and most of the composites were given as a range of values where the range varied up to 30% of the real part  $\epsilon'$  and as much as 100% of the imaginary part  $\epsilon''$ . Since no explanation was given for presentation of data as a range of values, it is possible that  $v_f$  and orientation effects were accounted for in this manner. In a follow-up article, Stonier [4] emphasized the importance of fiber orientation relative to the electric field in reflection loss, the inability of the material to absorb or transmit

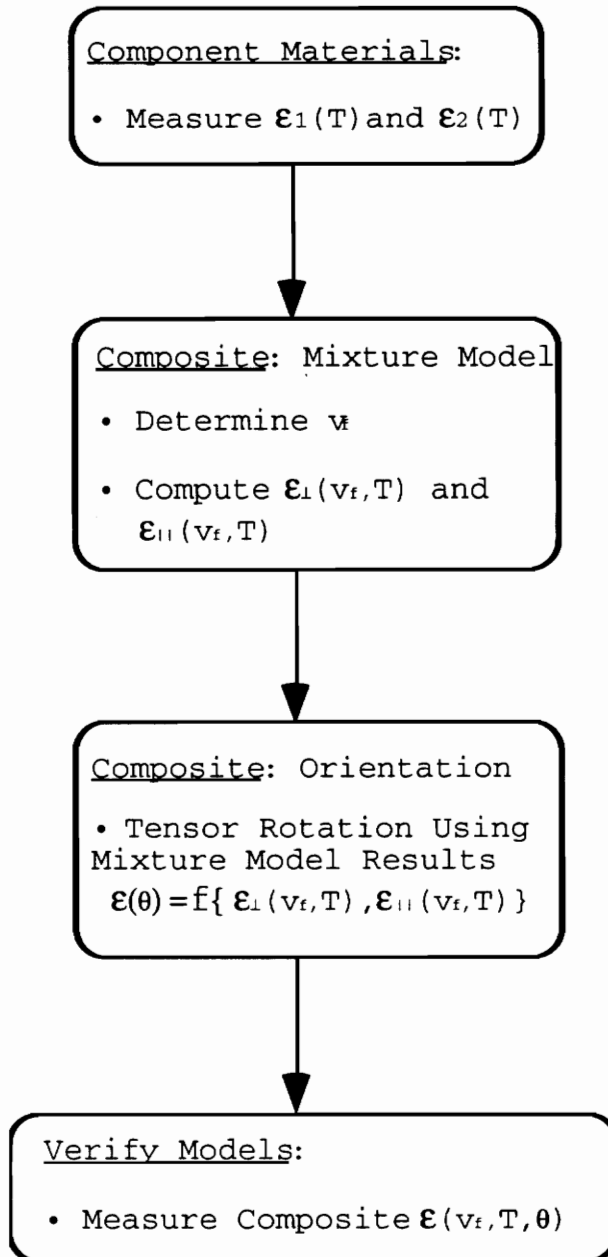


Figure 1.1.1: The process of unidirectional-fiber-reinforced composite permittivity modeling and verification.

incident electromagnetic energy. Reflection loss was tabulated at orientations of  $0^\circ$ ,  $45^\circ$  and  $90^\circ$  relative to  $\vec{E}$  in a graphite/epoxy composite.

In a recent effort to build a data base for radome designers, MacDonald and Moore [5,6] measured the microwave frequency permittivities of a large number of resins, ceramics, coatings, and composites. This study examined the effects of permittivity on several parameters including frequency (8 to 60 GHz), moisture, UV light exposure, and chemical ( $SO_2$ ) degradation. Only random fiber and honeycomb core composites were studied, so orientation effects were not important. A short section of the work referred to fiber volume fractions and mixture modeling with primary concern focused on moisture absorption effects. An Effective Medium Theory [7] approach was used for random fiber composites to successfully predict permittivity variations as a function of  $v_f$ . While this study was a valuable resource, it did not address unidirectional-fiber-reinforced composites.

Lee and Springer [8,9] conducted one of the first comprehensive studies into microwave processing of unidirectional-fiber/polymer-matrix laminates. Permittivity measurements were made in an effort to model the interaction of the electromagnetic fields and the composite laminate, i.e., the reflective, transmissive, and absorptive properties of S2 glass/epoxy and graphite/epoxy composites [8]. Permittivity data for unidirectional laminates, oriented in the principal directions parallel and perpendicular to the electric field, were measured and entered into a model for laminates consisting of many plies of arbitrary orientation. The electromagnetic model was verified experimentally using data measured from laminates of various stacking orientations and thicknesses. Permittivity was not modeled as a function of  $v_f$  and temperature.

In continued research, Lee and Springer [9] coupled the electromagnetic model with a conventional laminate consolidation/cure model to predict microwave processing profiles for the composites. Laminates of both the glass/epoxy and graphite/epoxy were cured in a 700 W multimode microwave oven using a polypropylene and teflon platen press for consolidation pressure. They concluded that glass/epoxy and unidirectional graphite/epoxy laminates could successfully be cured using microwaves. Multidirectional laminates of graphite/epoxy could not be cured successfully because the conductive fibers in the outer plies reflected or absorbed all of the incident energy. In this case fiber orientation was shown to be a critical parameter. As in the previous study, permittivity dependence on  $v_f$  was not considered. Instead, permittivity as a function of the degree of cure, as predicted by the cure model, was of primary concern; in a non-crosslinking system, temperature would be the process parameter that would most influence the composite permittivity.

In a feasibility study of microwave processing of composites Assudre et al. [10] measured the permittivities of PSP (polystyrylpyridine) thermoplastic resin and PSP/silica-glass composites as a function of temperature. There was no consideration of permittivity dependence on the fiber volume fraction, nor was orientation a factor. The composites were consolidated successfully, but no mention was made about process modeling or optimization in the thermoplastic system; a trial-and-error method was used to select the best cure cycle. Clearly the use of an electromagnetic/cure model, including a permittivity model with respect to the critical process parameters, would facilitate microwave processing of composites.

### 1.3 Overview

Chapter 2 introduces some basic concepts of permittivity physics, including dielectric loss mechanisms and several complex permittivity models for homogeneous materials. Permittivity mixture models are developed describing the dielectric properties of the fiber-reinforced composites, followed by the permittivity tensor rotation equations which form the basis of the orientation model. Chapter 3 introduces the electromagnetics of rectangular waveguides; this waveguide geometry was chosen for the permittivity measurements. The theory underlying the cavity perturbation and reflection cavity measurement techniques is also developed. The details of the specimen fabrication, dielectric measurement procedures, and a description of the test apparatus are outlined in Chapter 4. The results of the measurements are compared to the permittivity mixture and orientation models in Chapter 5 and several conclusions and recommendations for future study are presented in Chapter 6.

While the main thrust of this work centered on modeling the microwave frequency permittivity of unidirectional-fiber-reinforced polymer-matrix composites, dielectric measurements at these frequencies became a major component of the research. There are currently very few commercially available permittivity measurement systems in the GHz frequency range and these are not applicable to composite materials testing, especially at elevated temperatures. In fact, high temperature dielectric measurement techniques for low-loss materials are the subject of ongoing research in the electrical engineering community [11,12]. The need to understand the electromagnetic theory behind the dielectric measurement techniques employed in this study, including the assumptions made in and limitations of the techniques, prompted a detailed derivation of the underlying equations. Appendix A is an elementary summary of some of the important

points of electromagnetics and is often referenced in the derivations found in the body of the thesis; this summary was included as an aid to non-electrical engineers interested in microwave frequency dielectric measurements. This work provides not only a useful composite permittivity modeling approach, but also describes in detail some dielectric measurement techniques in the microwave frequency range.

## 2 PERMITTIVITY

### 2.1 Theory of Structure-Property Relationships

In order to understand how materials respond to microwave irradiation, the fundamental mechanisms of electromagnetic field-material interaction must be studied. While a more complete review of electromagnetic propagation through a general medium is presented in Appendix A, Section (A.2), the discussion presented here will be limited to complex permittivity in the cases of dielectric materials in the homogeneous phase and in heterogeneous mixtures. These cases represent conditions encountered in polymeric materials and composites containing non-conducting fibers, respectively.

#### 2.1.1 Polarization

When an electric field  $\vec{E}$  is imposed upon a material, bound charges and charged particles within the material move to align with the field. The movement, or alignment, of these particles away from an equilibrium position, due to the imposed field, is called polarization. The energy of the electric field incident upon the material is partially stored by the polarized charges or by polar molecules, called dipoles, that have separate positively and negatively charged regions. This storage phenomenon, which differentiates the material from free space, is a constitutive property of a specific material, and is described by the relative (real) permittivity, or dielectric constant  $\epsilon'$ .

The charge density arising from the aligned dipoles, known as the polarization field  $\vec{P}$ , only accounts for the bound part of the charge density in a material. The total electric charge flux density vector  $\vec{D}$  is the sum of the free and bound charge displacements due to  $\vec{E}$ :

$$\vec{D} = \epsilon_0 \vec{E} + \vec{P} \quad (2.1.1)$$

where  $\epsilon_0$  is the permittivity of free space. The constitutive relation for a general material is

$$\vec{D} = \epsilon_0 [\epsilon^*] \vec{E} \quad (2.1.2)$$

so the polarization can be found by combining Equations (2.1.1) and (2.1.2)

$$\vec{P} = \epsilon_0 \left( [\epsilon^*] - [\underline{1}] \right) \vec{E} \quad (2.1.3)$$

where  $[\epsilon^*]$  is the permittivity tensor and  $[\underline{1}]$  is the identity matrix.

There are several major polarization phenomena [13]. Dipoles fall into two categories: permanent and induced. Permanent dipoles have electrical asymmetry of charge groups in their molecular structure. Induced dipoles can result from either the shift in the electron cloud around the nucleus of an atom (electronic polarization) or from the relative displacement of nuclei because of unbalanced distribution of charge in a molecule (atomic polarization). Inhomogeneous materials can experience Maxwell-Wagner polarization which is the build-up of charges at the interfaces of dissimilar materials.

### 2.1.2 Complex Permittivity

As the electric field  $\vec{E}$  oscillates at higher frequencies, polarized groups and dipoles tend to displace in-phase with  $\vec{E}$ . These dipoles lose energy due to internal, elastic, or frictional resistance and therefore begin to lag the phase of  $\vec{E}$ . This behavior gives rise to the complex nature of the permittivity.

The fundamental quantities that relate  $\vec{E}$  and the current density  $\vec{J}$  (a measure of displaced charge due to  $\vec{E}$ ) are

conductivity  $\sigma$  and the complex relative permittivity  $\epsilon^*$ . Note that the relative permittivity is a dimensionless complex coefficient of the free space permittivity  $\epsilon_0$ ; all subsequent references in this work to the permittivity  $\epsilon^*$  imply that the quantity is relative. The derivation in Section (A.2) yields a relationship of the form

$$\begin{aligned}\bar{J} &= j\omega\epsilon_0\left(\epsilon' - j\left[\epsilon''_d + \frac{\sigma}{\omega\epsilon_0}\right]\right)\bar{E} \\ &= j\omega\epsilon_0(\epsilon' - j\epsilon''_{eff})\bar{E} \\ &= j\omega\epsilon_0\epsilon^*\bar{E}\end{aligned}\tag{A.19}$$

where the complex permittivity is defined to be

$$\epsilon^* = \epsilon' - j\epsilon''_{eff}\tag{2.1.4}$$

Again, this complex permittivity is a relative quantity, therefore  $\epsilon'$  and  $\epsilon''_{eff}$  are the dimensionless relative dielectric constant and loss factor, respectively. Note that, in Equation (A.19), the effective dielectric loss factor  $\epsilon''_{eff}$  (to be known simply as  $\epsilon''$  hereafter) accounts for both free-electron conductivity  $\sigma$  and dielectric loss mechanisms  $\epsilon''_d$ . Furthermore, if all of the loss mechanisms, including Maxwell-Wagner charging, induced polarization, and dipole rotation, are considered to contribute to dielectric loss in Equation (2.1.4), the form

$$\epsilon'' = \epsilon''_{dp} + \epsilon''_e + \epsilon''_a + \epsilon''_{mw} - (\sigma/\omega\epsilon_0)\tag{2.1.5}$$

is obtained, where the subscripts dp, e, a, and mw refer to dipolar, electronic, atomic, and Maxwell-Wagner effects, respectively. These effects are schematically illustrated in Figure 2.1.1. Equation (2.1.5) represents the total effective loss of the major polarization and conduction

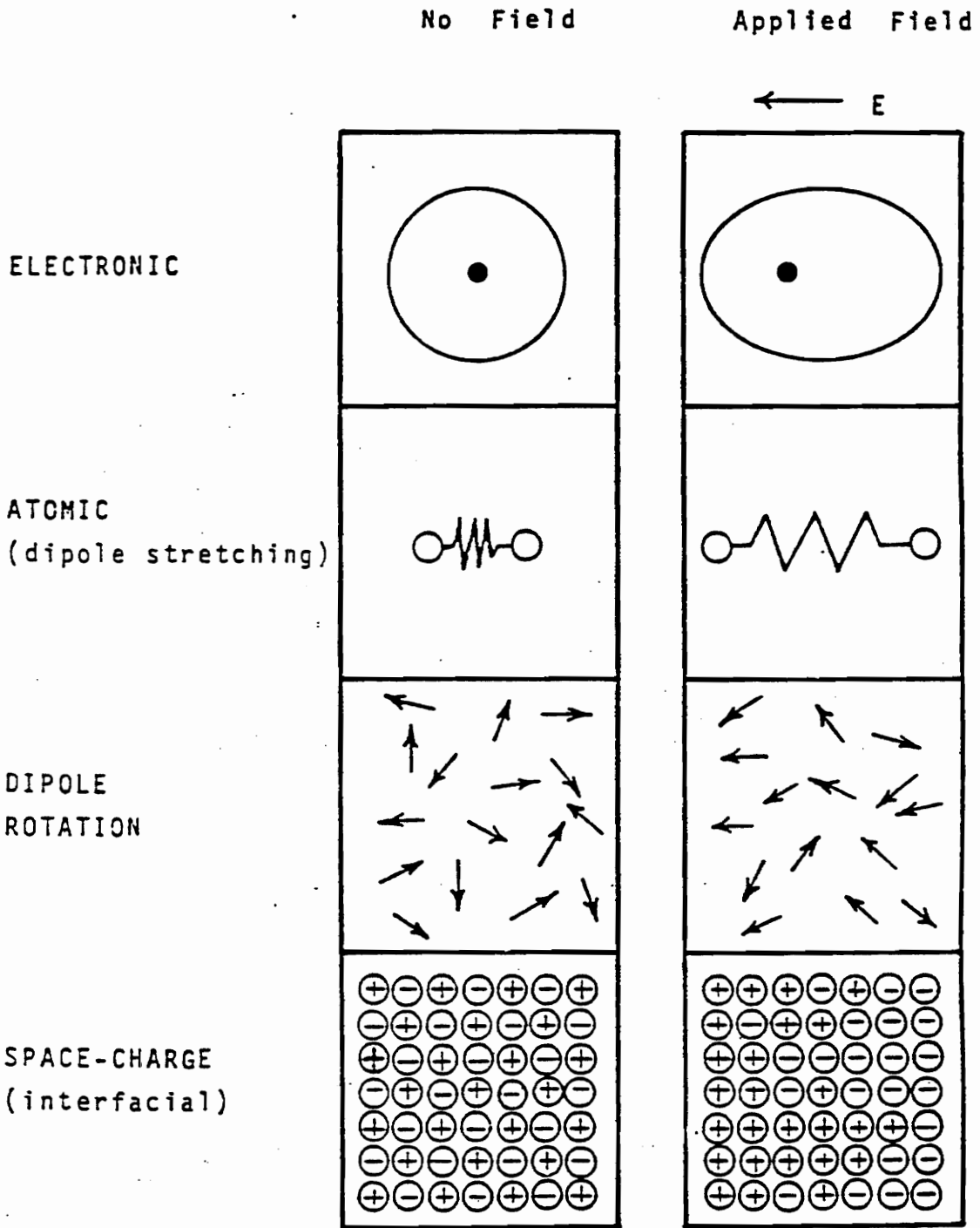


Figure 2.1.1: Polarization modes [35].

mechanisms at microwave frequencies. A commonly encountered quantity that provides insight into the "lossiness", or dissipative quality relative to the storage capability, of a material is the loss tangent  $\tan \delta$ . A discussion of  $\tan \delta$  is presented Section (A.2), leading to the definition

$$\tan \delta = \frac{\epsilon''_{\text{eff}}}{\epsilon'} = \frac{\epsilon''_d + \frac{\sigma}{\omega\epsilon'}}{\epsilon'} \quad (\text{A.26})$$

In the case of a dielectric material where  $\sigma = 0$ ,  $\tan \delta$  is the ratio of the imaginary to the real part of the permittivity.

### 2.1.3 Loss Mechanisms in Glass

The component materials used in this study, glass fibers and polymers, possess different dielectric loss mechanisms. These loss mechanisms, represented by  $\tan \delta$ , are generally a function of frequency and temperature. It is important to note that temperature and frequency effects on many loss mechanisms are fundamentally related. As temperatures increase, loss mechanisms that were more pronounced at lower frequencies shift toward higher frequencies; this is directly related to the increased mobility of molecular structures in bulk materials at higher temperatures.

The major microwave frequency dielectric loss mechanisms in glass are ion jump phenomena, ion vibrations and deformations, and dipole relaxation [14]. Ion jump mechanisms are best illustrated by the example of a substitution ion and related vacancy forming a dipole pair in a crystal lattice, as shown in Figure 2.1.2. This pair will behave like a molecular dipole and will reorient and relax under an applied electric field. Ion jump losses are important primarily at lower (kHz) frequencies, but at high temperatures they may have importance microwave frequencies.

Similarly, the effects of ion vibration and dipole relaxation will have a greater effect at higher temperatures. Ion vibration, a major loss mechanism at microwave frequencies, involves the drift of ionized dopant atoms or contaminants under an applied field. This is especially important in crystalline materials where dopant ions migrate to the grain boundaries where they can move more easily than ions locked into the atomic lattices [14]. A summary of loss mechanisms as a function of frequency is presented in Figure 2.1.3. It should be noted that, in general,  $\tan \delta$  for most glasses is very small at room temperature; those glass systems with ionic dopants or contaminants will display a higher loss.

#### 2.1.4 Loss Mechanisms in Polymers

The complex nature of polymers, which can include long chain-like structures of varied backbone segment lengths, polar side groups, and semicrystalline phases, leads to several dielectric loss mechanisms. Each of these mechanisms will have an associated peak on a plot of  $\tan \delta$  as a function of temperature or frequency. A schematic diagram of loss peaks for amorphous and semicrystalline polymers as a function of normalized temperature at 1 Hz is presented in Figure 2.1.4. A naming convention is employed where the highest temperature loss peak is denoted as the  $\alpha$  peak, the next peak in descending temperature is the  $\beta$  peak, followed by  $\gamma$ ,  $\delta$  and so on [15,16]. In semicrystalline polymers the  $\alpha$  peak occurs near the melt temperature  $T_m$  and is associated with the long range motion of chains as they gain more freedom of motion in the melt. The  $\beta$  peak is associated with chain motion near the glass transition temperature  $T_g$ . Polar side group rotation, which can occur to some degree even in the glassy state, is responsible for the  $\gamma$  peak. The  $\delta$  peak, and any subsequent peaks, are the result of increasingly

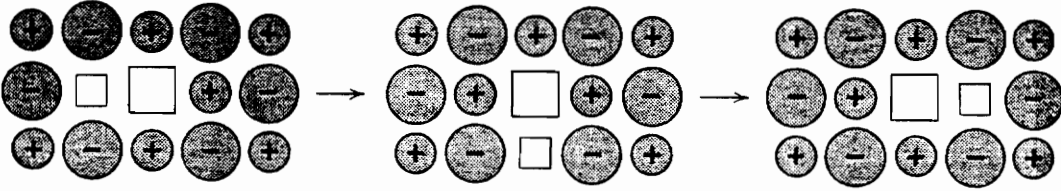


Figure 2.1.2: Reorientation of a lattice vacancy pair [14].

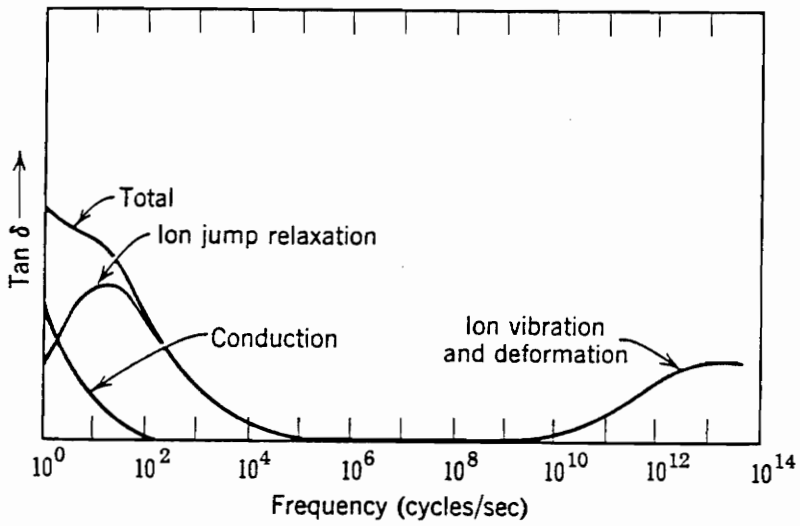


Figure 2.1.3: Effect of different dielectric loss mechanisms on  $\tan \delta$  at room temperature [14].

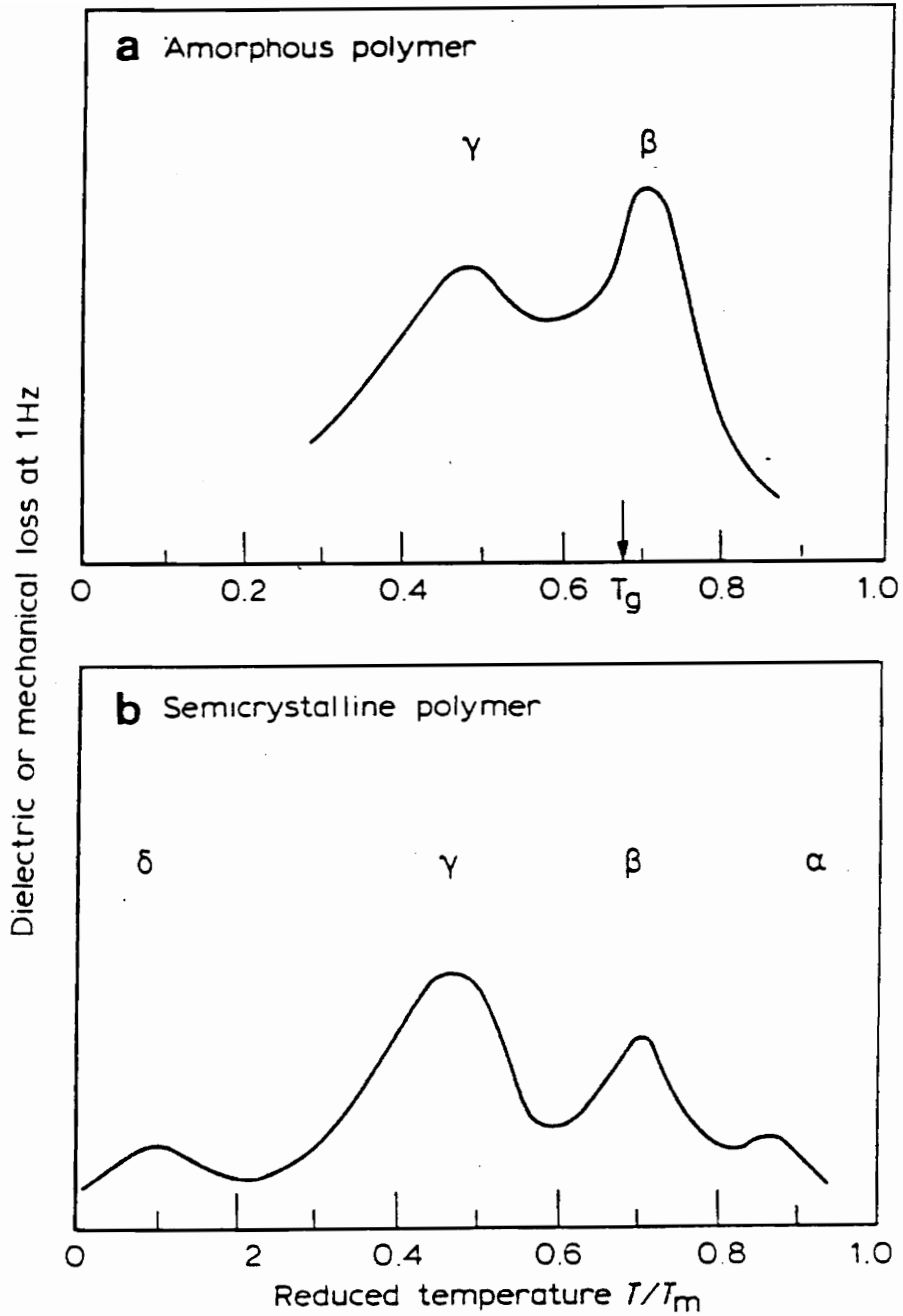


Figure 2.1.4: Schematic diagram of dielectric or mechanical loss at 1 Hz versus normalized temperature,  $T/T_m$ , where  $T_m$  is the melting point temperature for a linear polymer molecule;  $T_g$  is the glass transition temperature [17].

smaller polar group relaxation. In an amorphous polymer there is no  $\alpha$  relaxation related to crystal melting, so the first peak is the  $\beta$  peak is associated with the main chain relaxation near the glass transition temperature [17]. The  $\gamma$  peak is associated with local segment or side group motion below  $T_g$  and subsequent peaks result from smaller polar group relaxation.

The effects of temperature and frequency on loss mechanisms are directly related. Figure 2.1.5 illustrates the complex permittivity components of a polar amorphous polymer as a function of temperature in three frequency ranges. At low frequencies (DC to 1 kHz) the  $\alpha$  peak, associated with main chain motion in this figure, exists just above the main chain  $T_g$  of the polymer. A  $\beta$  relaxation peak, due to local segment motion, distinctly exists above the local chain  $T_g'$  but below  $T_g$ . At very high temperatures, in the softening region, a  $\lambda$  peak occurs associated with ionic conduction. At intermediate frequencies (1 kHz to 100 kHz), the  $\alpha$  and  $\beta$  peaks shift upward in temperature, with the separation between the peaks narrowing. The narrowing of the temperature gap between the  $\alpha$  and  $\beta$  peaks is a result of the difference in activation energy behavior in the two loss mechanisms as the frequency increases [16]. The general upward shift of loss peaks along the temperature axis is a result of the need for greater molecular mobility for chains to rotate and relax under the influence of higher frequency excitation. This increased mobility is achieved at higher temperatures. Note that the ionic loss peak  $\lambda$  is greatly diminished at higher frequencies. At microwave frequencies (GHz) the loss peaks have broadened and merged into a single relaxation peak beginning in the temperature range near  $T_g$ . This single peak is the result of increased free volume in the bulk allowing polar chain segment relaxation. Note that

ionic loss contributions at microwave frequencies are negligible.

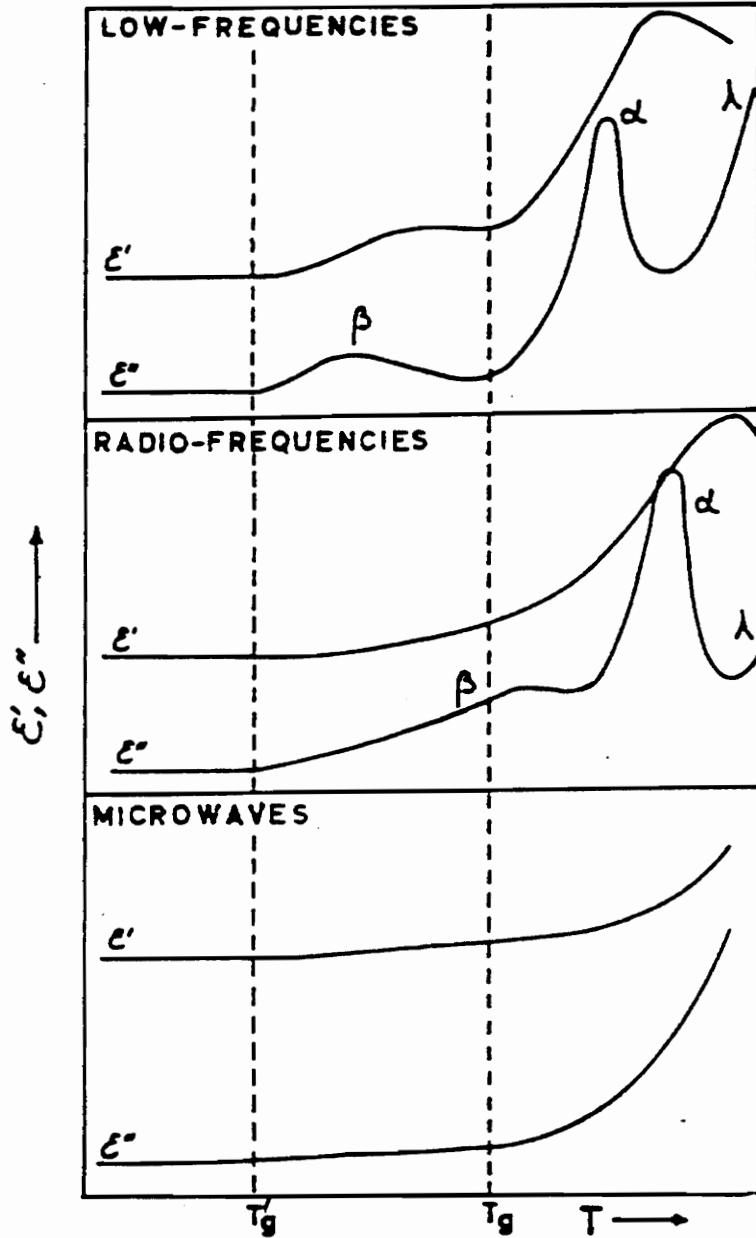


Figure 2.1.5: Schematic representations of the permittivity as a function of temperature for a model linear polymer over different frequency ranges [36].

### 2.1.5 Physical Models of Permittivity and Loss

Molecular reorientation due to polarization of dipoles, also known as Debye dipole loss, is the dominant electric field coupling mechanism at microwave frequencies [13]. The dominance of this mechanism is attributable to the fact that, for many common molecules, the time constant for rotation and relaxation (return to original position) are on the same order as the period of oscillation of  $\vec{E}$ . A quantitative approach to this phenomenon was developed by Debye in 1929, assuming spherical dipolar molecules in a viscous medium, results in

$$\epsilon' = \frac{\epsilon_{\infty} + (\epsilon_s - \epsilon_{\infty})}{(1 + \omega^2 \tau^2)} \quad (2.1.6a)$$

$$\epsilon'' = \frac{(\epsilon_s - \epsilon_{\infty})\omega\tau}{(1 + \omega^2 \tau^2)} \quad (2.1.6b)$$

where  $\epsilon_s$  and  $\epsilon_{\infty}$  are the dielectric constants at very low frequency and very high frequency, respectively,  $\omega$  is the circular frequency, and  $\tau$  is the relaxation time constant [18]. These equations will now be interpreted qualitatively.

When the electric field oscillates at very low frequency ( $\omega \rightarrow 0$ ),  $\epsilon' \approx \epsilon_s$  and  $\epsilon'' \approx 0$ . This condition implies that the low frequency rotation of dipoles allows nearly total energy conservation, since the dipole can easily remain in-phase with  $\vec{E}$ . At high frequencies ( $\omega \rightarrow \infty$ ),  $\epsilon' \approx \epsilon_{\infty}$  and  $\epsilon'' \approx 0$ . In this case,  $\vec{E}$  oscillations are so rapid that dipoles cannot begin to reorient, consequently a lower limit on the dielectric constant,  $\epsilon_{\infty}$ , is reached. This condition is analogous to diffraction in the optical region where the electric field merely changes velocity while traveling through a lossless ( $\epsilon'' \approx 0$ ) medium [13].

There must exist an intermediate frequency range where the amount of polarization-rotation phase-lag is a maximum.

This condition exists when  $\omega\tau = 1$ ; at that frequency, the dielectric loss factor is a maximum ( $\epsilon'' = \epsilon''_{\max}$ ). At this frequency, the incident energy that was "stored" by a higher  $\epsilon'$  at lower frequencies is now dissipated by loss mechanisms (i.e., a larger  $\epsilon''$ ). Figure 2.1.6, a typical plot of the components of  $\epsilon^*$  over the frequency spectrum, illustrates the preceding arguments for  $\epsilon_{\infty}$ ,  $\epsilon_s$ , and the intermediate loss range [13].

For the Debye model of Equations (2.1.6a) and (2.1.6b) to adequately model solid dielectric materials, it must account for the polarization effects due to adjacent molecules [13]. In order to apply the Debye equations to solids, one must consider the activation energy necessary to rotate a polarized molecule against the potential gradients of the surrounding molecules in the material. A Debye time constant ( $\tau_0$ ) can be introduced into Equations (2.1.6a) and (2.1.6b) in place of  $\tau$

$$\tau_0 = \frac{1}{\nu} \left( \frac{\epsilon_s - 2}{\epsilon_{\infty} + 2} \right) e^{(-U_a/k_B T)} \quad (2.1.7)$$

where  $(1/\nu)$  is the period of one oscillation in the "potential well" of the surrounding molecules,  $U_a$  is the activation energy,  $k_B$  is the Boltzmann constant, and  $T$  is absolute temperature. Note that the temperature dependence of this relaxation time constant is assumed to be statistically based and is of an Arrhenius form.

The only material specific parameter in Debye's simple model is the activation energy  $U_a$ . This single parameter limits the model to narrow and asymmetric relaxation spectra not consistent with actual polymer behavior [16]. Another well known relaxation model is that of the 2-parameter Cole-Cole equation [19]

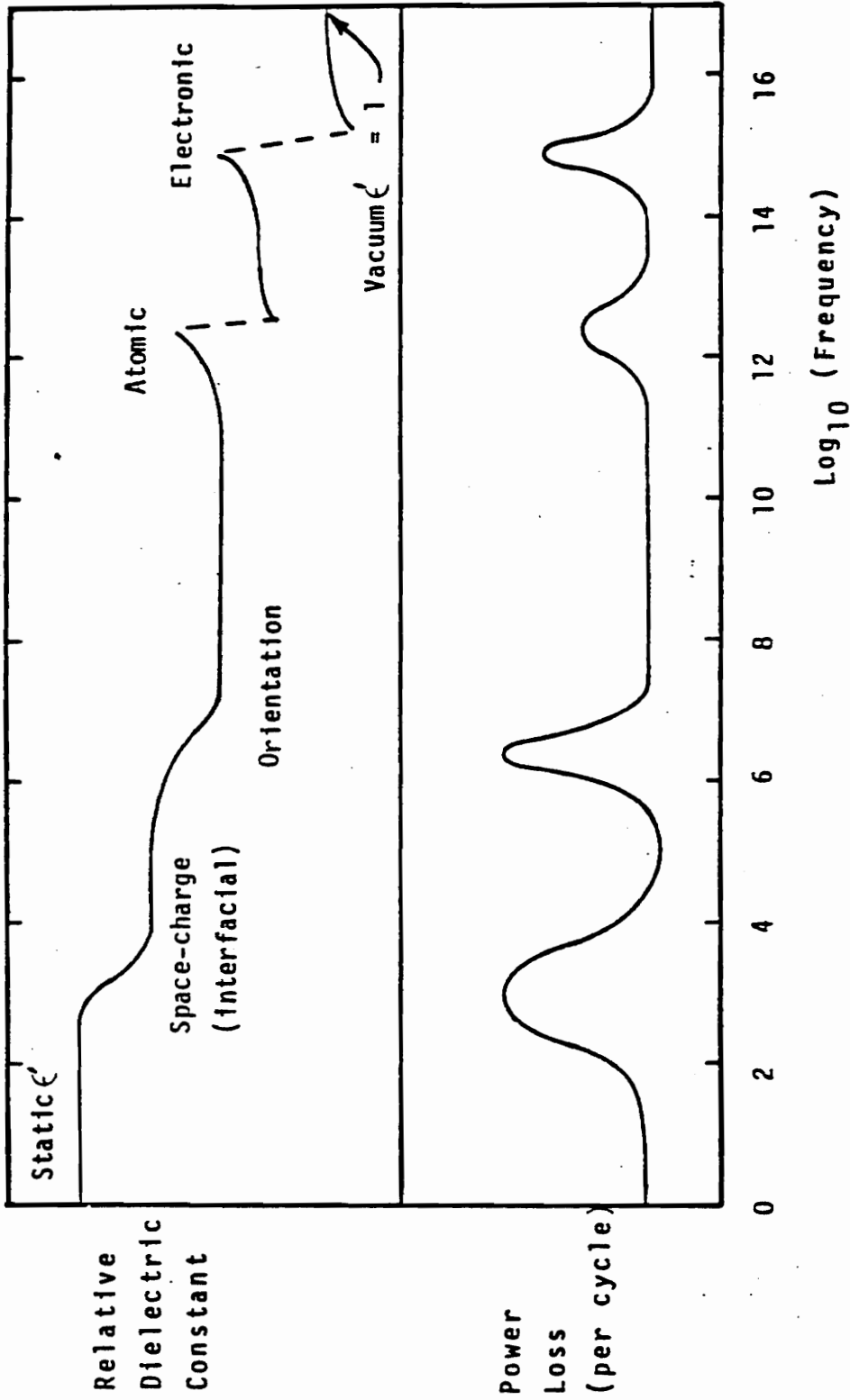


Figure 2.1.6: Approximate frequencies where polarization modes occur in glassy polymers [37].

$$\epsilon^* = \frac{\epsilon_\infty + (\epsilon_s - \epsilon_\infty)}{1 + (j\omega\tau)^{1-\sigma}} \quad (2.1.8)$$

where  $\tau$  is still the dipole relaxation time constant, and a new parameter  $\sigma$  is a measure of the interaction between the dipoles. This interaction is important in polymers where dipoles from the same chain, or from different chains, might strongly interact. This model yields more satisfactory results for polymer relaxation spectra. A more advanced model that accounts for both the width and skewness of polymer relaxation spectra is the 3-parameter Havriliak-Negami model [20]; this model accurately describes Tg relaxation spectra. The Havriliak-Negami model has the form

$$\epsilon^* = \frac{\epsilon_\infty + (\epsilon_s - \epsilon_\infty)}{(1 + (j\omega\tau)^{1-\alpha'})^{-\beta'}} \quad (2.1.9)$$

where  $\alpha'$  and  $\beta'$  are the dispersion width and skewness parameters, respectively.

## 2.2 Permittivity Mixture Models

The effective permittivity of unidirectional-fiber-reinforced composite materials can be modeled in two ways. An approach analogous to layered capacitor dielectrics provides very simple limiting values of permittivity for composites oriented parallel ( $\parallel$ ) and perpendicular ( $\perp$ ) to the electric field  $\vec{E}$ . A more rigorous averaged field approach leads to similar results having somewhat more complicated forms. An elementary description of averaged field models will be given since they are the basis for modeling a wide variety of composite material mixtures beyond unidirectional-fiber composites.

### 2.2.1 Layered Dielectric Model

Assume that the fiber/matrix mixture in a composite material behaves electrically like layered dielectrics between the plates of a capacitor, as illustrated in Figure 2.2.1. The dielectrics have dissimilar permittivities denoted by  $\epsilon_1$  and  $\epsilon_2$  and are oriented parallel and perpendicular to the applied electric field  $\vec{E}$ .

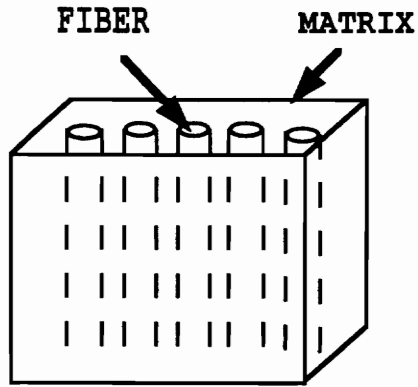
Consider first the capacitance of the layered dielectric parallel ( $C_{\parallel}$ ) to  $\vec{E}$ . The capacitance of each layer is additive, or in series, resulting in a total parallel capacitance of

$$C_{\parallel} = C_1 + C_2 \quad (2.2.1)$$

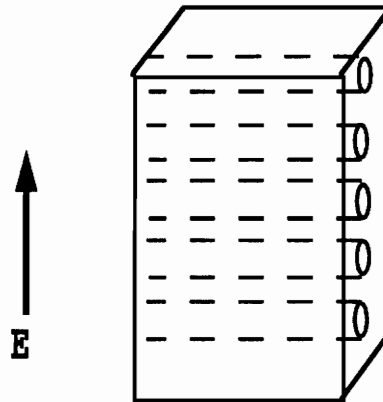
where  $C_1$  and  $C_2$  are the capacitances of the layers of permittivity 1 and 2, respectively. From elementary electrostatics of parallel plate capacitors, the overall capacitance is [21]

$$C = \epsilon S / d_{\epsilon} \quad (2.2.2)$$

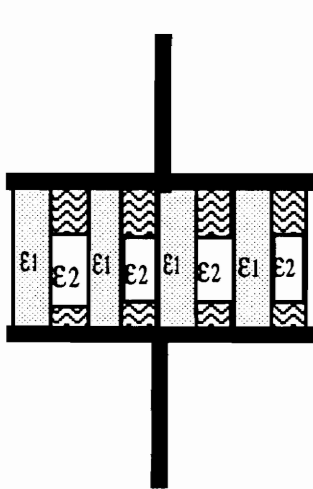
where  $S$  = the surface area of the plates



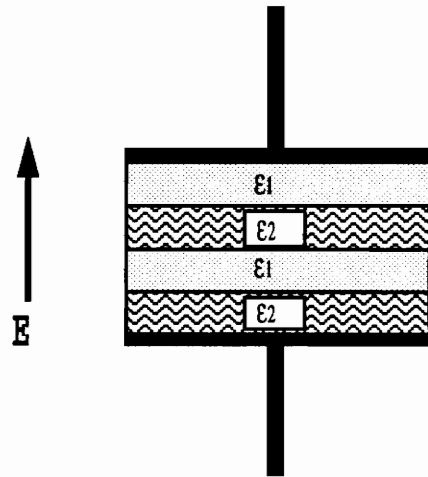
Fibers Parallel to E



Fibers Perpendicular to E



Dielectrics in Parallel



Dielectrics in Series

Figure 2.2.1: Parallel plate capacitor analogy for permittivity modeling in fiber reinforced composite materials.

$d_{\epsilon}$  = separation of the plates

$\epsilon$  = the permittivity of the dielectric between the plates

It follows that for each component dielectric, Equation (2.2.2) becomes

$$C_i = \epsilon_i S_i / d_{\epsilon i} \quad (2.2.3)$$

where  $S_i$  = the area of the surface of the  $i^{\text{th}}$  dielectric parallel to the plane of the plates

$d_{\epsilon i}$  = the thickness of each dielectric along the normal to the plates

$\epsilon_i$  = the permittivity of  $i^{\text{th}}$  dielectric

The total volume of the heterogeneous dielectric ( $V_D$ ) is

$$V_D = S d_{\epsilon} \quad (2.2.4a)$$

and the volume of the  $i^{\text{th}}$  component is

$$V_i = S_i d_{\epsilon i} \quad (2.2.4b)$$

The volume fraction of the  $i^{\text{th}}$  dielectric relative to the total dielectric is

$$v_i = V_i / V_D \quad (2.2.5)$$

An effective permittivity for this parallel orientation ( $\epsilon_{||}$ ) is computed by substituting Equation (2.2.2) and Equation (2.2.3) into Equation (2.2.1) to arrive at

$$\epsilon_{||} = \frac{d_{\epsilon}}{S} \left( \frac{\epsilon_1 S_1}{d_{\epsilon 1}} + \frac{\epsilon_2 S_2}{d_{\epsilon 2}} \right) \quad (2.2.6)$$

When Equations (2.2.4a) and (2.2.4b) are substituted into Equation (2.2.6), and the fact that  $d_{\epsilon} = d_{\epsilon 1} = d_{\epsilon 2}$  is employed, the result is

$$\epsilon_{||} = \epsilon_1 v_1 + \epsilon_2 v_2 \quad (2.2.7)$$

where Equation (2.2.5) is used to write Equation (2.2.7) in terms of volume fractions.

The layered dielectric oriented perpendicular to  $\vec{E}$ , or electrically in series, results in a total perpendicular capacitance  $C_{\perp}$  of

$$C_{\perp} = 1/C_1 + 1/C_2 \quad (2.2.8)$$

An effective permittivity of this perpendicular orientation ( $\epsilon_{\perp}$ ) can be determined using a solution method similar to that for  $\epsilon_{\parallel}$ . Substituting Equations (2.2.2) and (2.2.3) into Equation (2.2.8), solving for volumes using Equations (2.2.4a) and (2.2.4b) where  $S = S_1 = S_2$ , and using Equation (2.2.5) to convert to volume fractions, leads to

$$\epsilon_{\perp} = \frac{1}{\left(\frac{v_1}{\epsilon_1}\right) + \left(\frac{v_2}{\epsilon_2}\right)} \quad (2.2.9)$$

Equations (2.2.7) and (2.2.9), which have the well-known forms of "rule-of-mixtures" models, provide upper and lower bounds, respectively, on the permittivity of binary mixtures [22]. Each equation is easily adapted to an n-component mixture by expanding the preceding derivation.

### 2.2.2 Averaged Field Model

Consider an element of volume  $V_D$  comprised of a host medium containing particles of material with dissimilar dielectric properties, placed between the plates of a capacitor. Assume that the local electric flux density  $\vec{D}$  and local electric field  $\vec{E}$  can be defined with an isotropic permittivity ( $\epsilon_k$ ) for each component material as

$$\vec{D} = \epsilon_k \vec{E} \quad (2.2.10)$$

The effective electric flux density and electric field that could be measured in the capacitor would depend upon the

effective permittivity of the material mixture. Thus the equation

$$\bar{\underline{D}} = \underline{\epsilon} \bar{\underline{E}} \quad (2.2.11)$$

defines the effective electric field  $\bar{\underline{E}}$ , effective flux density  $\bar{\underline{D}}$ , and the effective mixture permittivity  $\underline{\epsilon}$ .

If the quantities in Equation (2.2.11) are considered over the volume of the element, then the contributions of the host medium and the particles would be evaluated separately as [23]

$$V_D \bar{\underline{D}} = \int_{V_H} \epsilon_H \bar{\underline{E}} dV + \sum_j \int_{V_j} \epsilon_j \bar{\underline{E}} dV \quad (2.2.12)$$

where

$\epsilon_H$  = permittivity of the host medium

$\epsilon_j$  = permittivity of the  $j^{\text{th}}$  material comprising the particles

$V_H$  = that part of the total volume occupied by the host medium

$V_j$  = that part of the total volume occupied by the  $j^{\text{th}}$  material

Note that  $\bar{\underline{D}}$  is the effective flux density while  $\bar{\underline{E}}$  is local. Since  $V_D = V_H + V_j$ , Equation (2.2.12) can be rewritten, employing the effective electric field for the host medium, as

$$V_D \bar{\underline{D}} = V \epsilon_H \bar{\underline{E}} + \sum_j \int_{V_j} (\epsilon_j - \epsilon_H) \bar{\underline{E}} dV \quad (2.2.13)$$

Recalling Equation (2.2.5) for volume fractions  $v_j$ , and dividing Equation (2.2.13) by  $V_D$ , leads to

$$\bar{\underline{D}} = \epsilon_H \bar{\underline{E}} + \sum_j v_j (\epsilon_j - \epsilon_H) \frac{1}{V_j} \int_{V_j} \bar{\underline{E}} dV \quad (2.2.14)$$

where  $\epsilon_H$  and  $\epsilon_j$  have been assumed to be uniform over the  $j^{\text{th}}$  material volume. Substituting  $\bar{\underline{D}}$  from Equation (2.2.11) into

Equation (2.2.14) and dividing by the effective electric field  $\bar{\underline{E}}$  leads to

$$\underline{\epsilon} = \epsilon_H + \sum_j v_j (\epsilon_j - \epsilon_H) \frac{\langle \bar{\underline{E}}_j \rangle}{\bar{\underline{E}}} \quad (2.2.15)$$

where  $\langle \bar{\underline{E}}_j \rangle$  is a volume averaged electric field over the volume of all of the  $j^{\text{th}}$  particles. This equation holds exactly for a  $j$  component system if the effective field is assumed to be uniformly imposed upon the volume  $V_D$  [22].

Since the composites used in this study are composed of only two materials, Equation (2.2.15) can be rewritten

$$\underline{\epsilon} = \epsilon_1 + (\epsilon_2 - \epsilon_1) v_2 f_2 \quad (2.2.16)$$

where  $\epsilon_1$  = host (or matrix) material permittivity  
 $\epsilon_2$  = particle material permittivity  
 $v_2$  = the volume fraction of particles  
 $f_2 = \frac{\langle \bar{\underline{E}}_2 \rangle}{\bar{\underline{E}}}$ ; the average field ratio

The averaged field factor  $f_i$  is the key quantity that differentiates between the approaches used in several models. Since  $f_i$  can be determined exactly only for regularly shaped particles in very low concentrations, approximations of the geometries and field distributions must be made in general mixtures.

The geometric approximation most often made in practice assumes that the particles have an ellipsoidal shape, since closed form field ratios can be found for this geometry. Assuming very low concentrations of ellipsoidal particles having permittivity  $\epsilon_2$  in a host medium of permittivity  $\epsilon_1$ , the field ratio (equivalent to  $f_i$  in this case) is given by [22]

$$\frac{\langle E_2 \rangle}{\langle E_1 \rangle} = \sum_{k=1}^3 \frac{\cos^2 a_k}{1 + \left(\frac{\epsilon_2}{\epsilon_1} - 1\right) A_k} \quad (2.2.17)$$

where  $a_k$  is the angle between the  $\vec{E}$  field vector and the  $k^{\text{th}}$  ellipsoidal axis, and  $A_k$  is the depolarization factor. Note that  $\langle E_1 \rangle$  has replaced  $\vec{E}$  since, for low concentrations of particles, the mean field ( $\vec{E}$ ) is assumed to be very close to the field in the matrix phase  $\langle E_1 \rangle$  [22].

The depolarization factor describes the effect of the geometry of a body on the difference between the  $\vec{E}$  fields external to that body and the internal  $\vec{E}$  field [24]. For an ellipsoidal particle, the depolarization factor is written

$$A_k = \frac{x_1 x_2 x_3}{2} \int_0^{\infty} \frac{du}{(x_k^2 + u) \left[ (x_1^2 + u)(x_2^2 + u)(x_3^2 + u) \right]^{\frac{1}{2}}} \quad (2.2.18)$$

$$k = 1, 2, 3$$

where  $x_{1,2,3}$  are the semi-axes of the ellipsoid. It can be shown that  $A_1 + A_2 + A_3 = 1$  [23]. The inclusion geometry of primary concern to those working with fiber-reinforced composites are prolate spheroids with very large aspect ratios ( $\gamma_a$ ); this geometry is very similar to that of needles. If a prolate spheroid of circular cross-section in the plane of minor dimension has an aspect ratio of  $\gamma_a > 15$ , then it can be shown that [22]

$$\begin{aligned} A_1 &\approx 0 \\ A_2 &= A_3 \approx 0.5 \end{aligned} \quad (2.2.19)$$

If the composite in question contains fibers with  $\gamma_a \leq 15$ , the depolarization factors can be computed using the following [25]:

$$A_1 = \left[ \frac{-\gamma_a (e_p - \tanh^{-1} e_p)}{(\gamma_a^2 - 1)^{\frac{3}{2}}} \right] \quad (2.2.20a)$$

where  $e_p$  is the eccentricity of the spheroid:

$$e_p = \left[ 1 - \left( \frac{1}{\gamma_a} \right)^2 \right]^{\frac{1}{2}} \quad (2.2.20b)$$

The perpendicular-direction depolarization factors can subsequently be determined from

$$A_2 = A_3 = (1 - A_1) / 2 \quad (2.2.21)$$

With the knowledge of the depolarization factors from Equation (2.2.19) or Equations (2.2.20) through (2.2.21), the field ratio  $f_2$  from Equation (2.2.17) can be determined for a specific particle orientation, and Equation (2.2.16) can be solved for an effective permittivity given component permittivities and volume fractions. The resulting formula is limited to very low concentrations of included particles since  $\bar{\mathbf{E}}$  has been assumed to be close to  $\langle \mathbf{E}_1 \rangle$ . For oriented ellipsoidal inclusions the composite permittivity is

$$\underline{\epsilon} = \epsilon_1 + (\epsilon_2 - \epsilon_1) v_2 \frac{\epsilon_1}{\epsilon_1 + (\epsilon_2 - \epsilon_1) A_k} \quad (2.2.22)$$

Equation (2.2.22) is a useful starting result; but real composite systems necessitate corrections that allow for higher inclusion volume fractions in the model.

One approach to modeling the permittivity of mixtures with higher concentrations of particles assumes that Equation (2.2.17) still holds with one further assumption:  $\langle \mathbf{E}_1 \rangle$  in Equation (2.2.17) is replaced by a weighted average  $\langle \mathbf{E} \rangle$  of the mean  $\bar{\mathbf{E}}$  fields in each component. If the weighted average relation

$$\langle E \rangle = v_1 \langle E_1 \rangle + v_2 \langle E_2 \rangle \quad (2.2.23a)$$

is employed, the effective mixture permittivity equation becomes

$$\underline{\epsilon} \langle E \rangle = v_1 \epsilon_1 \langle E_1 \rangle + v_2 \epsilon_2 \langle E_2 \rangle \quad (2.2.23b)$$

Using Equation (2.2.23), Equation (2.2.17), and the  $A_k$  definitions, Wagner derived a mixture model for spherical inclusions that was expanded to oriented ellipsoids by Sillars [22,26]:

$$\underline{\epsilon} = \epsilon_1 \frac{\epsilon_1(1 - v_2)(1 - A_k) + \epsilon_2(v_2 + A_k(1 - v_2))}{\epsilon_1 + A_k(1 - v_2)(\epsilon_2 - \epsilon_1)} \quad (2.2.24)$$

This method of approximation is known as the "mean field" method with Equation (2.2.24) known as the Wagner-Sillars formula.

Another method commonly used to model mixtures assumes that, for a two-phase system, the ellipsoidal particles are surrounded not by just a matrix phase, but by an "effective medium" that accounts for the permittivities of the matrix and other surrounding particles. This approach is therefore known as the "effective medium theory" model. If the effective medium external to the included particles has permittivity  $\epsilon_m$ , then it follows that, at low inclusion concentrations,  $\epsilon_m \approx \epsilon_1$  since the matrix predominates. Thus, for low concentrations, Equation (2.2.22) still applies. At higher concentrations, however,  $\epsilon_m$  begins to take on the appearance of the effective permittivity  $\underline{\epsilon}$  itself, hence  $\epsilon_m \approx \underline{\epsilon}$ . Substituting  $\underline{\epsilon}$  for  $\epsilon_1$  in Equation (2.2.17) and employing Equation (2.2.16) leads to, for oriented ellipsoidal inclusion,

$$\underline{\epsilon} = \epsilon_1 + (\epsilon_2 - \epsilon_1)v_2 \frac{\underline{\epsilon}}{\underline{\epsilon} + (\epsilon_2 - \underline{\epsilon})A_k} \quad (2.2.25)$$

This method was first derived for spheres by Bottcher and was extended to oriented ellipsoids by Hsu [22,27].

The mean field model of Equation (2.2.24) and effective medium model of Equation (2.2.25) have been presented here as examples of widely used, rigorously derived models, but they are only two of many approaches.

Other theories employ polarizabilities of ellipsoids in an effective medium [28], confocal ellipsoids that are analogous to inclusion/matrix interfaces [29,30], and pair-correlation methods for conductor/insulator particle composites [31]. These models, among others, are discussed and tabulated in several excellent references [22,30,32].

### 2.2.3 Model Comparison and Evaluation

The focus of this study is upon unidirectional continuous-fiber reinforced, two-phase composites. Thus, Equations (2.2.24) and (2.2.25) have been posed in oriented-particle form instead of random-particle form. Furthermore, the aspect ratio ( $\gamma_a$ ) of the fibers in these composites is very large, so that the  $A_k$  values in Equation (2.2.19) apply. It becomes apparent, upon substitution of  $A_k$  from Equation (2.2.19) into Equations (2.2.24) and (2.2.25), that the effective permittivity of parallel-oriented particles,  $\epsilon_{||}$ , reduces to the rule-of-mixtures, Equation (2.2.7). The predicted effective permittivities for perpendicular oriented particles  $\epsilon_{\perp}$  are, in general, different. The averaged field model Equations (2.2.24) and (2.2.25) predict larger values of  $\epsilon_{\perp}$  than does the reciprocal rule-of-mixtures model, Equation (2.2.9), making the latter a lower bound. The permittivity predicted by previously detailed mixture models are shown in Figure 2.2.2 for a composite with fiber permittivity of  $\epsilon^*_2 = 5.2 - j0.035$  and a matrix permittivity of  $\epsilon^*_1 = 2.72 - j0.0034$ . Because of their simplicity and their

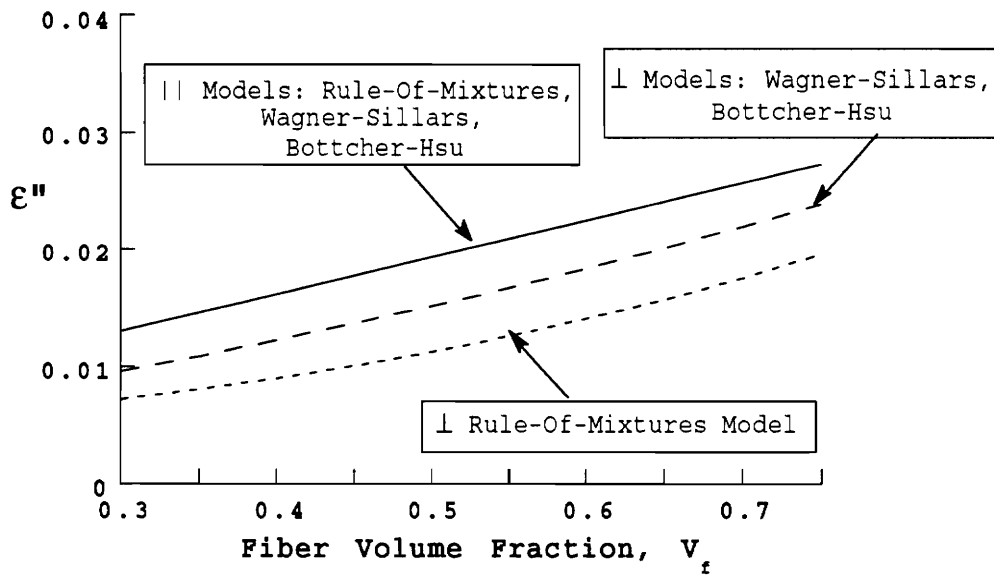
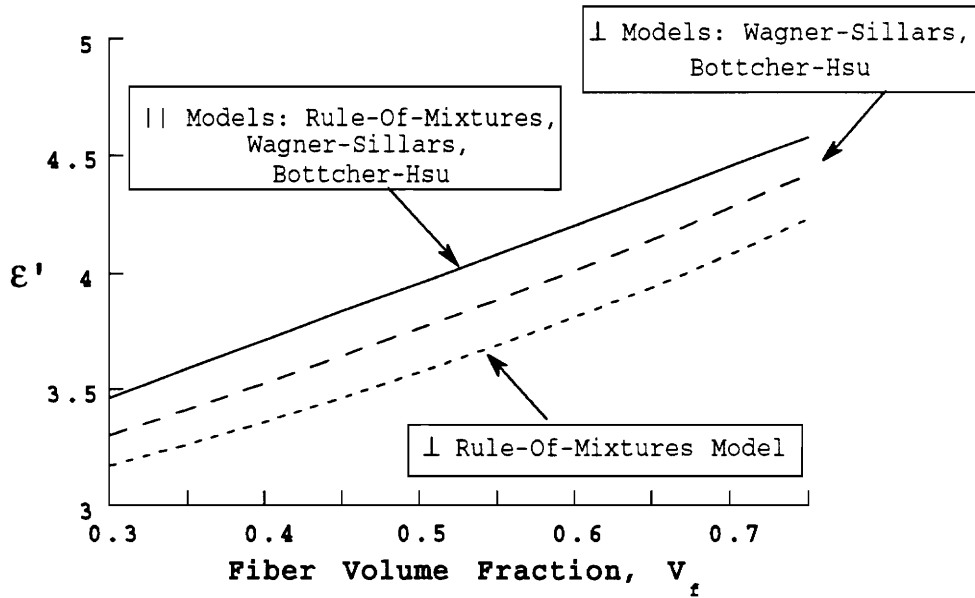


Figure 2.2.2: Comparison of complex permittivity mixture models for a unidirectional continuous-fiber-reinforced polymer-matrix composite.

prediction of bounding values for  $\epsilon^*(v_f)$ , the rule-of-mixtures models will be the primary models studied in this work.

## 2.3 Orientation

The mixture models of Section (2.2) provide a means of predicting the permittivities of a unidirectional-fiber-reinforced composite, oriented either parallel or perpendicular to an applied electric field component. The objective of this section is to model the permittivity of the composite at any orientation relative to an electric field component using principal direction permittivities. The orientation model predicts the general permittivity tensor based upon the results of the mixture models; the inputs to this model are the component permittivities,  $v_f$ , and the angle of orientation  $\theta$ .

### 2.3.1 The Permittivity Tensor and Orientation

A general anisotropic material must be characterized by a permittivity tensor  $[\epsilon^*]$  as indicated in Equation (2.1.2). This vector equation, in an arbitrary set of rectangular coordinates  $(x,y,z)$ , takes the form

$$\begin{Bmatrix} D_x \\ D_y \\ D_z \end{Bmatrix} = \begin{bmatrix} \epsilon_{xx} & \epsilon_{xy} & \epsilon_{xz} \\ \epsilon_{yx} & \epsilon_{yy} & \epsilon_{yz} \\ \epsilon_{zx} & \epsilon_{zy} & \epsilon_{zz} \end{bmatrix} \begin{Bmatrix} E_x \\ E_y \\ E_z \end{Bmatrix} \quad (2.3.1)$$

where each permittivity term may be complex. In the case of an electromagnetic wave propagating along the z-direction in an orthotropic composite plate, one in which there exist three distinct permittivities in the three orthogonal directions, the  $[\epsilon^*]$  tensor takes the form



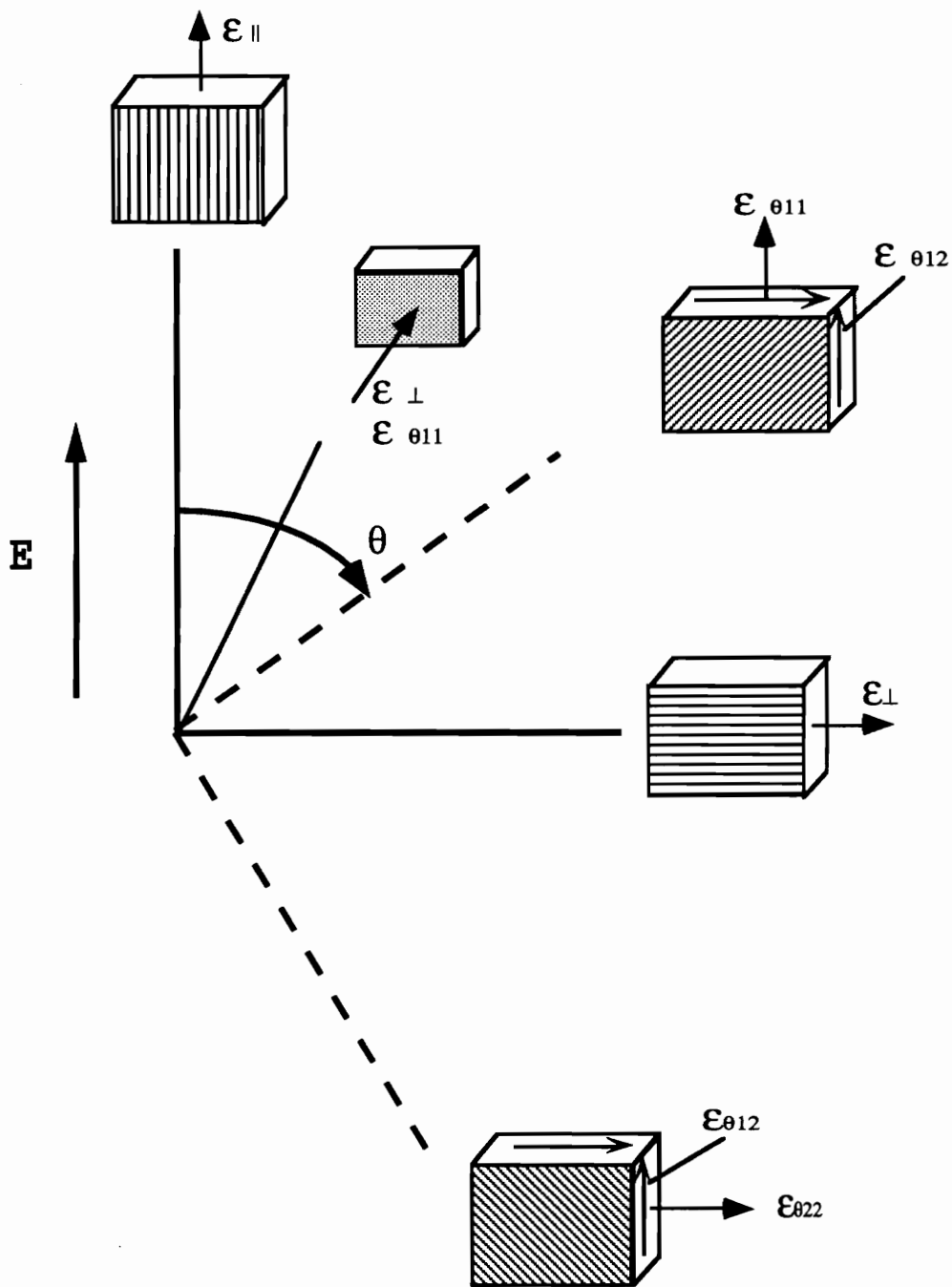


Figure 2.3.1: The rotation of axes through an angle  $\theta$  about the normal to the plane of the composite. The solid axes are those of the principal permittivity components. Fiber orientation relative to each direction is also shown.

obtained by considering the rotation of the axes corresponding to the principal permittivity tensor of Equation (2.3.3) through the angle  $\theta$  about a normal to the plane of the composite into some arbitrary orientation, as shown in Figure 2.3.1. The tensor rotation formula for this planar geometry can be written

$$\begin{Bmatrix} \epsilon_{\theta 11} \\ \epsilon_{\theta 22} \\ \epsilon_{\theta 33} \\ \epsilon_{\theta 12} \end{Bmatrix} = \begin{bmatrix} \cos^2 \theta & \sin^2 \theta & 0 \\ \sin^2 \theta & \cos^2 \theta & 0 \\ 0 & 0 & 1 \\ -\cos \theta \sin \theta & \cos \theta \sin \theta & 0 \end{bmatrix} \begin{Bmatrix} \epsilon_{\parallel} \\ \epsilon_{\perp} \\ \epsilon_{\perp} \end{Bmatrix} \quad (2.3.4)$$

where the principal permittivity tensor has been expressed in a contracted notation as a column vector [34], and  $\epsilon_{\theta 11}$ ,  $\epsilon_{\theta 22}$ , and  $\epsilon_{\theta 33}$  are the permittivities in the rotated orientation corresponding to the axes shown in Figure 2.3.1. The cross term  $\epsilon_{\theta 12}$ , which is assumed to be equal to  $\epsilon_{\theta 21}$  in this case, relates the electric flux density in the 1-direction to the electric field component in the 2-direction.

The rotated permittivity tensor of Equation (2.3.4) can be written as

$$[\epsilon_{\theta}] = \begin{bmatrix} \epsilon_{\theta 11} & \epsilon_{\theta 12} & 0 \\ \epsilon_{\theta 12} & \epsilon_{\theta 22} & 0 \\ 0 & 0 & \epsilon_{\theta 33} \end{bmatrix} = \begin{bmatrix} \epsilon_{\theta 11} & \epsilon_{\theta 12} & 0 \\ \epsilon_{\theta 12} & \epsilon_{\theta 22} & 0 \\ 0 & 0 & \epsilon_{\perp} \end{bmatrix} \quad (2.3.5)$$

This is the desired result that predicts the permittivity of an orthotropic planar material oriented at an arbitrary angle  $\theta$  relative to an electric field component, in terms of the principal permittivities. Note that Equations (2.2.7) and (2.2.9) can predict the principal permittivities  $\epsilon_{\parallel}$  and  $\epsilon_{\perp}$  based solely upon the permittivities of the fiber and matrix materials and the fiber volume fraction.

### 2.3.2 Experimental Considerations

In order to verify the tensor rotation relation given in Equation (2.3.4), a technique described in Section (3.3), known as the reflection cavity technique, has been used to measure the microwave frequency permittivity of composite material samples in various orientations. This measurement technique employs a resonant cavity that supports only a single electric field  $\vec{E}$  component considered to be oriented along a principal axis. The energy  $U_E$  stored in an orthotropic dielectric of arbitrary orientation and of volume  $V_\epsilon$  must be determined as a part of the analysis used in formulating the reflection cavity technique. Referring to Section (A.3) in Appendix A, Equation (A.28a) defines  $U_E$  as

$$U_E = \frac{1}{4} \int_{V_\epsilon} \epsilon' |\vec{E}|^2 dV \quad (\text{A.28a})$$

This definition can be written in more general terms, for a planar orthotropic dielectric material with a single  $E_x$  field imposed throughout its volume, as

$$U_E = \frac{1}{4} \int_{V_\epsilon} \begin{bmatrix} \epsilon'_{11} & \epsilon'_{12} & 0 \\ \epsilon'_{12} & \epsilon'_{22} & 0 \\ 0 & 0 & \epsilon'_{33} \end{bmatrix} \begin{Bmatrix} E_x \\ 0 \\ 0 \end{Bmatrix} \cdot \begin{Bmatrix} E_x^* \\ 0 \\ 0 \end{Bmatrix} dV \quad (\text{2.3.6})$$

where the \* superscript denotes the complex conjugate. When the permittivity tensor is multiplied by the single electric field component and the inner product is taken of the resulting vector and the conjugate electric field component, Equation (2.3.6) becomes

$$U_E = \frac{\epsilon'_{11}}{4} \int_{V_\epsilon} |E_x|^2 dV \quad (\text{2.3.7})$$

Note that only the  $\epsilon'_{11}$  term remains; the reflection cavity technique, therefore, will measure only the permittivity

component oriented in the direction of the electric field. Referring back to Equation (2.3.4) for an orientation angle of  $\theta$ ,  $\epsilon'_{11}$  from Equation (2.3.7) can be written

$$\epsilon'_{11} = \epsilon'_{\theta 11} = \epsilon'_{\parallel} \cos^2 \theta + \epsilon'_{\perp} \sin^2 \quad (2.3.8)$$

Following a development akin to Equations (2.3.6) and (2.3.7) based instead on the equation for power loss  $P_{\epsilon}$  in the dielectric,

$$P_{\epsilon} = \frac{\omega \epsilon_0}{2} \int_{V_{\epsilon}} \epsilon'' |\vec{E}|^2 dV \quad (2.3.9)$$

for a single electric field component  $E_x$ , results in

$$\epsilon''_{11} = \epsilon''_{\theta 11} = \epsilon''_{\parallel} \cos^2 \theta + \epsilon''_{\perp} \sin^2 \quad (2.3.10)$$

which is similar to Equation (2.3.8) but applies instead to the dielectric loss factor. Thus, Equations (2.3.8) and (2.3.10) are to be used to verify the tensor rotation in Equation (2.3.4) using experimentally measured permittivity data. These results are presented in Section (5.2).

### 3 PERMITTIVITY MEASUREMENT THEORY AND TECHNIQUES

#### 3.1 Rectangular Waveguides

The type of transmission line chosen for measuring dielectric properties in this study is the rectangular waveguide. While this waveguide geometry is commonly used for high-power transmission, it is also well suited to certain types of dielectric measurement techniques because of a single component dominant  $\vec{E}$  field mode, the  $TE_{10}$  mode. The development of  $TE_{10}$  mode characteristics in rectangular waveguides will provide a basis for understanding the cavity measurement techniques that follow.

##### 3.3.1 $TE_{mn}$ Modes

Transverse electric (TE) waves are a subset of TEM waves where  $E_z = 0$  and  $H_z \neq 0$ . Using these assumptions, Maxwell's curl equations (A.5a) and (A.5b) can be solved in terms of  $H_z$  as

$$H_x = -\frac{j\beta}{k_c^2} \frac{\partial H_z}{\partial x} \quad (3.1.1a)$$

$$H_y = -\frac{j\beta}{k_c^2} \frac{\partial H_z}{\partial y} \quad (3.1.1b)$$

$$E_x = -\frac{j\omega\mu}{k_c^2} \frac{\partial H_z}{\partial y} \quad (3.1.1c)$$

$$E_y = \frac{j\omega\mu}{k_c^2} \frac{\partial H_z}{\partial x} \quad (3.1.1d)$$

Where  $k_c$  is the cutoff wavenumber defined as

$$k_c^2 = k^2 - \beta^2 \quad (3.1.2a)$$

In Equation (3.1.2a)  $k$  is the complex wavenumber of the electromagnetic fields and is defined as

$$k = \omega\sqrt{\mu\epsilon} \quad (3.1.2b)$$

and  $\beta$  is the propagation phase constant. Note that, for transmission lines supporting TEM modes having no cutoff condition,  $k_c = 0$  and  $k = \beta$  in Equation (3.1.2a) [33]. Cutoff is the electromagnetic phenomenon where, in a transmission line of some geometry, propagation is supported only above some cutoff frequency  $f_c$ ; below  $f_c$  any EM wave launched into the waveguide is evanescent and decays exponentially along the axis of propagation.

In order to solve Equations (3.1.1a) through (3.1.1d),  $H_z$  must be determined from the two-dimensional wave equation [33]:

$$\left( \frac{\partial^2}{\partial x^2} + \frac{\partial^2}{\partial y^2} + k_c^2 \right) h_z = 0 \quad (3.1.3)$$

where  $H_z = h_z(x, y) e^{-j\beta z}$  for a plane wave propagating in the  $z$  direction. The geometry of a rectangular waveguide is shown in Figure 3.1.1 . The dimensions follow the convention of  $a > b$  with  $a$  in the  $x$  direction,  $b$  in the  $y$  direction, and the  $z$  direction along the waveguide axis. Assume that the waveguide is filled with some medium of permittivity  $\epsilon$  and permeability  $\mu$ . Equation (3.1.3) can be solved using the method of separation of variables and application of boundary conditions on the tangential electric fields that must vanish at the conductive waveguide walls [33]. The final result for  $H_z$  is

$$H_z = A_{mn} \cos \frac{m\pi x}{a} \cos \frac{n\pi y}{b} e^{-j\beta z} \quad (3.1.4)$$

where  $A_{mn}$  = mode dependent amplitude coefficients  
 $n, m = 0, 1, 2, \dots$  ; mode numbers

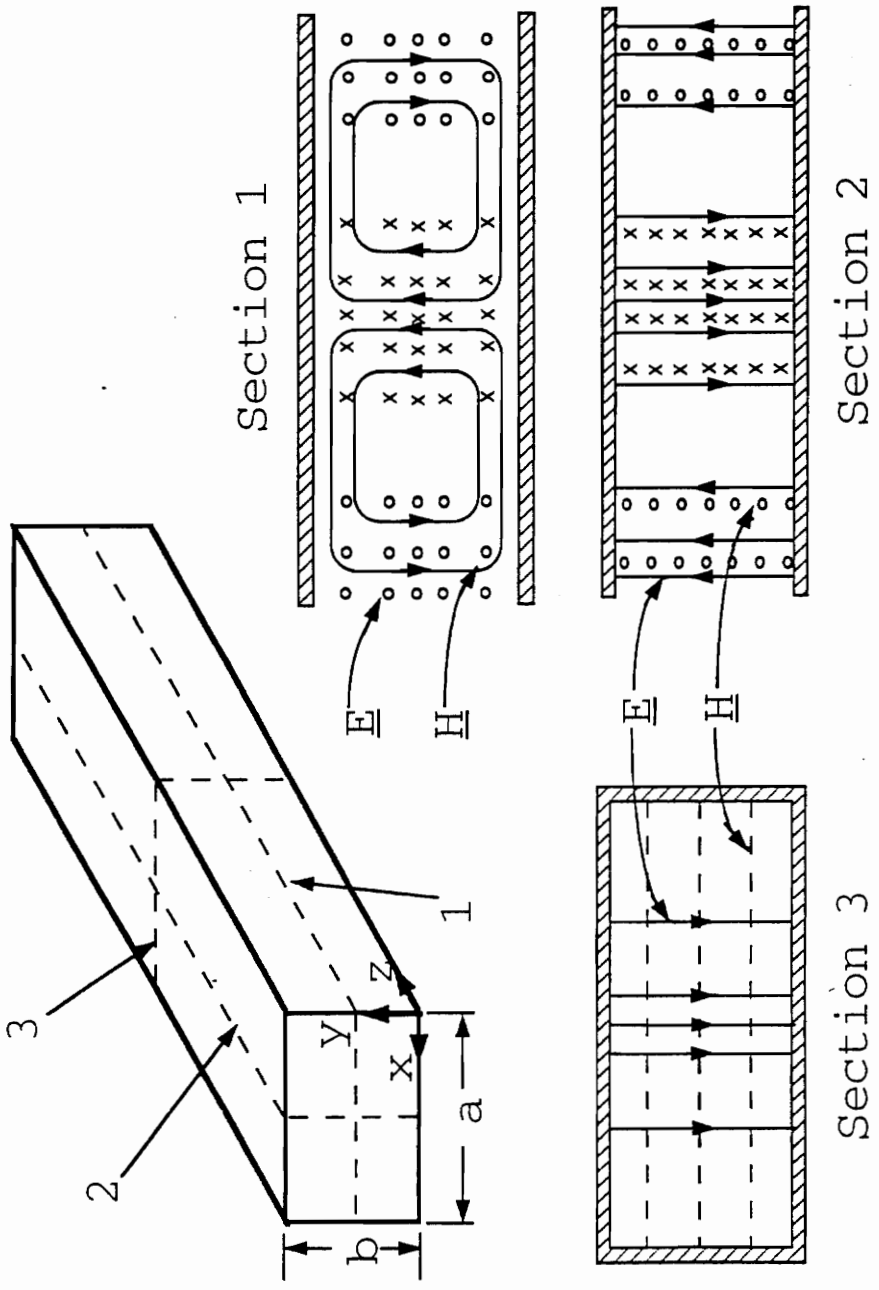


Figure 3.1.1.1: Rectangular waveguide geometry and the TE<sub>10</sub> electromagnetic field distribution.

Substitution of Equation (3.1.4) into Equations (3.1.1a) through (3.1.1d) yields

$$E_x = \frac{j\omega\mu n\pi}{k_c^2 b} A_{mn} \cos \frac{m\pi x}{a} \cos \frac{n\pi y}{b} e^{-j\beta z} \quad (3.1.5a)$$

$$E_y = -\frac{j\omega\mu m\pi}{k_c^2 a} A_{mn} \sin \frac{m\pi x}{a} \cos \frac{n\pi y}{b} e^{-j\beta z} \quad (3.1.5b)$$

$$H_x = \frac{j\beta m\pi}{k_c^2 a} A_{mn} \sin \frac{m\pi x}{a} \cos \frac{n\pi y}{b} e^{-j\beta z} \quad (3.1.5c)$$

$$H_y = \frac{j\beta n\pi}{k_c^2 b} A_{mn} \cos \frac{m\pi x}{a} \sin \frac{n\pi y}{b} e^{-j\beta z} \quad (3.1.5d)$$

where  $\beta$  = the propagation phase constant

$$= \sqrt{k^2 - \left(\frac{m\pi}{a}\right)^2 - \left(\frac{n\pi}{b}\right)^2} \quad (3.1.6)$$

Note that a comparison of Equations (3.1.2a) and (3.1.6) identifies  $k_c$  as

$$k_c = \sqrt{\left(\frac{m\pi}{a}\right)^2 + \left(\frac{n\pi}{b}\right)^2} \quad (3.1.7)$$

This result for  $k_c$  arises from satisfying the electric field boundary conditions in the solution of Equation (3.1.3). The cutoff frequency  $f_{c_{mn}}$ , corresponding to the condition of  $k = k_c$ , i.e., when  $\beta = 0$  in Equation (3.1.2a), can be found by solving Equations (3.1.2b) and (3.1.7) for  $\omega_c (=2\pi f_c)$ :

$$f_{c_{mn}} = \frac{k_c}{2\pi\sqrt{\mu\epsilon}} = \frac{1}{2\pi\sqrt{\mu\epsilon}} \sqrt{\left(\frac{m\pi}{a}\right)^2 + \left(\frac{n\pi}{b}\right)^2} \quad (3.1.8)$$

The wave impedance in a  $TE_{mn}$  mode can be defined as the ratio of electric to magnetic fields using Equations (3.1.5a), (3.1.5d) and (3.1.2b)

$$Z_{TE} = \frac{E_x}{H_y} = \frac{k\eta}{\beta} = \frac{\omega\mu}{\beta} \quad (3.1.9)$$

where  $\eta = \sqrt{\frac{\mu}{\epsilon}}$  is the intrinsic impedance of the material filling the waveguide. Equation (3.1.6) implies that the cutoff wavenumber  $k_c$  effectively shifts the phase planes (represented by  $\beta$ ) inside the waveguide relative to the planes of the same wave in free space. This phase shift leads to a wavelength inside the waveguide that is longer than that of a free-space wavelength, at the same frequency. Since the wavelength is defined as the distance between two equal phase planes, the following relations hold:

$$\lambda_g = \frac{2\pi}{\beta} > \lambda = \frac{2\pi}{k} \quad (3.1.10)$$

where  $\lambda_g =$  guide wavelength  
 $\lambda =$  free-space wavelength

### 3.1.2 The TE<sub>10</sub> Mode

The dominant mode in a waveguide has the lowest cutoff frequency and can exist as the sole mode over a certain frequency range. In rectangular waveguides the TE<sub>10</sub> mode, corresponding to  $m = 1$  and  $n = 0$ , is the dominant mode. The field quantities in Equations (3.1.4) and (3.1.5a) through (3.1.5d) can be reduced, for the TE<sub>10</sub> mode, to

$$H_z = A_{10} \cos \frac{\pi x}{a} e^{-j\beta z} \quad (3.1.11a)$$

$$E_y = -\frac{j\omega\mu a}{\pi} A_{10} \sin \frac{\pi x}{a} e^{-j\beta z} \quad (3.1.11b)$$

$$H_x = \frac{j\beta a}{\pi} A_{10} \sin \frac{\pi x}{a} e^{-j\beta z} \quad (3.1.11c)$$

$$E_x = E_z = H_y = 0 \quad (3.1.11d)$$

where  $A_{10} =$  amplitude constant specific to the TE<sub>10</sub> mode  
 $= \sqrt{\frac{2}{ab}}$

The EM field distributions for the TE<sub>10</sub> mode are shown in Figure 3.1.1. Note that the electric field has only a single y-direction component; this fact is advantageous and is utilized in permittivity measurement techniques. The cutoff frequency for the TE<sub>10</sub> mode can be determined from Equation (3.1.8) as

$$f_{c_{10}} = \frac{1}{2a\sqrt{\mu\epsilon}} \quad (3.1.12)$$

Likewise,  $k_c$  and  $\beta$  are also mode specific; for the TE<sub>10</sub> mode

$$k_c = \frac{\pi}{a} \quad (3.1.13)$$

$$\begin{aligned} \beta &= \sqrt{k^2 - \left(\frac{\pi}{a}\right)^2} \\ &= \sqrt{\omega^2\mu\epsilon - \left(\frac{\pi}{a}\right)^2} \\ &= \sqrt{\epsilon\left(\frac{\omega}{c}\right)^2 - \left(\frac{\pi}{a}\right)^2} \end{aligned} \quad (3.1.14)$$

where, in the definition of  $\beta$ ,  $k$  has been substituted using Equation (3.1.2b). In the final expression  $c$  is the speed of light; this is a substitution of the phase velocity, Equation (A.11), with a general relative permittivity  $\epsilon$  and an assumed non-ferromagnetic permeability of  $\mu = 1$ .

## 3.2 Cavity Perturbation

The cavity perturbation technique was chosen to measure the microwave frequency permittivity of the glass fiber and polycarbonate component materials. This technique is well suited to accommodate materials in the form of strands. Bundles of material strands can easily be inserted into the cavity through holes in the waveguide walls without disassembly of any components; this measurement configuration is detailed in Section (3.2.4) of this chapter and in Sections (4.2.4) and (4.2.5). This technique is based upon the assumption that low-loss dielectric materials, introduced into an empty resonant cavity, will change the conditions within the cavity only slightly. These small changes in cavity resonant conditions can be measured, and with the knowledge of material geometry, the permittivity can be computed. The following development is similar to that of Altschuler; this is an excellent source for more detailed information on this technique [39].

### 3.2.1 The Empty Lossless Cavity Condition

Assume a cavity with arbitrary shape and perfect (or very good) conductors for wall surfaces, containing lossless (or very low-loss) materials. Maxwell's equations under these conditions can be written in phasor form similar to Equations (A.5a) and (A.5b):

$$\vec{\nabla} \times \vec{E} = -j\omega\mu\vec{H} \quad (3.2.1a)$$

$$\vec{\nabla} \times \vec{H} = j\omega\varepsilon\vec{E} \quad (3.2.1b)$$

with  $\varepsilon$ ,  $\mu$ , and  $\omega$  real in this case. Taking the scalar products,

$$\begin{aligned} & \vec{H} \cdot (\vec{\nabla} \times \vec{E}) \\ & \vec{E} \cdot (\vec{\nabla} \times \vec{H}) \end{aligned}$$

subtracting, and integrating over the cavity volume ( $V_c$ ), yields

$$\begin{aligned} & \int_{V_c} [\vec{E} \cdot (\vec{\nabla} \times \vec{H}) - \vec{H} \cdot (\vec{\nabla} \times \vec{E})] dV \\ & = \int_{V_c} [\vec{E} \cdot (j\omega\epsilon\vec{E}) - \vec{H} \cdot (-j\omega\mu\vec{H})] dV \quad (3.2.2) \\ & = j\omega \int_{V_c} [\epsilon\vec{E} \cdot \vec{E} - \mu\vec{H} \cdot \vec{H}] dV \end{aligned}$$

where Equations (3.2.1a) and (3.2.1b) have been substituted.

Using the vector identity

$$\vec{B} \cdot (\vec{\nabla} \times \vec{A}) - \vec{A} \cdot (\vec{\nabla} \times \vec{B}) = \vec{\nabla} \cdot (\vec{A} \times \vec{B})$$

the left-hand integrand of Equation (3.2.2) becomes  $\vec{\nabla} \cdot (\vec{H} \times \vec{E})$ . Substituting this identity and using Gauss's theorem, Equation (3.2.2) becomes

$$\begin{aligned} & \int_{V_c} \vec{\nabla} \cdot (\vec{H} \times \vec{E}) dV \\ & = \int_{S_c} (\vec{H} \times \vec{E}) \cdot \vec{n} dS \quad (3.2.3) \\ & = j\omega \int_{V_c} [\epsilon\vec{E} \cdot \vec{E} + \mu\vec{H} \cdot \vec{H}] dV \end{aligned}$$

where  $S_c$  denotes the surface area of the cavity walls and  $\vec{n}$  is the unit vector normal to the surface.

Since it has been assumed that the walls are perfect conductors where the tangential electric fields vanish, it follows that

$$\vec{E} = E \vec{n}$$

is the only electric field component on the surface  $S_C$  and thus the quantity

$$\vec{H} \times \vec{E} = \vec{H} \times \vec{n} E$$

cannot have a component normal to  $S_C$ , leading to

$$(\vec{H} \times \vec{E}) \cdot \vec{n} = 0$$

Since the left-hand integrands of Equation (3.2.3) are zero, the result of Equation (3.2.3) is

$$\int_{V_C} \epsilon \vec{E} \cdot \vec{E} \, dV = - \int_{V_C} \mu \vec{H} \cdot \vec{H} \, dV \quad (3.2.4)$$

If the standing waves in the cavity are considered with  $\vec{E}$  being real, then  $\vec{H}$  from Equation (3.2.1) is imaginary, and

$$\vec{E} \cdot \vec{E} = |E|^2, \quad \vec{H} \cdot \vec{H} = -|H|^2$$

Note the sign change in the magnetic field scalar product due to the sign in Equation (3.2.1). Equation (3.2.4) can now be written

$$\int_{V_C} \epsilon |E|^2 \, dV = \int_{V_C} \mu |H|^2 \, dV \quad (3.2.5)$$

Recalling Equations (A.28a) and (A.28b), it is clear that the integral terms of Equation (3.2.5) represent the average energy stored in the electric and magnetic fields within a material of permittivity  $\epsilon$  and permeability  $\mu$ . This result implies that, for a lossless closed cavity with perfectly conducting walls, the time-averaged electric and magnetic field energies are equal.

### 3.2.2 Cavity Perturbation

The results of Equation (3.2.5) hold approximately for

conditions close to those previously assumed, i.e., walls with very high conductivity and a low-loss material medium occupying the cavity volume. Cavity perturbation is based on this approximation

It is to be assumed that the only difference between two cavities containing two different dielectric materials is due to differences in permittivity and permeability. Equation (3.2.1) can be written

$$(\vec{\nabla} \times \vec{E}_i) = -j\omega_i \mu_i \vec{H}_i \quad \left. \vphantom{(\vec{\nabla} \times \vec{E}_i)} \right\} i = 1, 2 \quad (3.2.6a)$$

$$(\vec{\nabla} \times \vec{H}_i) = j\omega_i \epsilon_i \vec{E}_i \quad (3.2.6b)$$

where 1 and 2 correspond to the empty and material loaded cavities, respectively. The frequencies  $\omega_i$  are now taken to be complex; all losses, including material and external coupling, are accounted for in this way. Using steps similar to those taken in deriving Equations (3.2.2) through (3.2.4), the result is

$$\begin{aligned} & \omega_1 \int_{V_c} [\epsilon_1 \vec{E}_1 \cdot \vec{E}_2 - \mu_1 \vec{H}_1 \cdot \vec{H}_2] dV \\ & = \omega_2 \int_{V_c} [\epsilon_2 \vec{E}_1 \cdot \vec{E}_2 - \mu_2 \vec{H}_1 \cdot \vec{H}_2] dV \end{aligned} \quad (3.2.7)$$

Now subtracting both sides of Equation(3.2.7) from the quantity

$$\omega_2 \int_{V_c} [\epsilon_1 \vec{E}_1 \cdot \vec{E}_2 - \mu_1 \vec{H}_1 \cdot \vec{H}_2] dV$$

and rearranging gives

$$\frac{\omega_2 - \omega_1}{\omega_2} = \frac{\int_{V_c} [(\mu_2 - \mu_1) \vec{H}_1 \cdot \vec{H}_2 - (\epsilon_2 - \epsilon_1) \vec{E}_1 \cdot \vec{E}_2] dV}{\int_{V_c} [\epsilon_1 \vec{E}_1 \cdot \vec{E}_2 - \mu_1 \vec{H}_1 \cdot \vec{H}_2] dV} \quad (3.2.8)$$

For condition 1 corresponding to a cavity filled only with air ( $\epsilon_1 = \epsilon_0$ ,  $\mu_1 = \mu_0$ ) and cavity condition 2 corresponding to a cavity containing homogeneous materials ( $\epsilon_2$  and  $\mu_2$  are constant at a fixed temperature), Equation(3.2.8) becomes

$$\frac{\omega_2 - \omega_1}{\omega_2} = \frac{(\mu_2 - \mu_0) \int_{V_\epsilon} \vec{H}_1 \cdot \vec{H}_2 dV - (\epsilon_2 - \epsilon_0) \int_{V_\epsilon} \vec{E}_1 \cdot \vec{E}_2 dV}{2\epsilon_0 \int_{V_c} |\vec{E}_1|^2 dV} \quad (3.2.9)$$

where  $V_\epsilon$  is the volume of the sample and is considered to be very small relative to the volume of the cavity ( $V_\epsilon \ll V_c$ ). The integrals in the numerator of Equation (3.2.9) are taken only over  $V_s$  because outside of the sample  $\epsilon_1 = \epsilon_2 = \epsilon_0$  and  $\mu_1 = \mu_2 = \mu_0$ , thus  $\epsilon_1 - \epsilon_2 = 0$  and  $\mu_1 - \mu_2 = 0$ . In the denominator integrals, the fields inside and outside of the specimen have been assumed to differ very little, thus  $\vec{E}_2 = \vec{E}_1$  and  $\vec{H}_2 = \vec{H}_1$ . The vector products become  $|\vec{E}_1|^2$  and  $-|\vec{H}_1|^2$ , the integrals of which can be interchanged by recalling Equation(3.2.5).

If the material in cavity condition 2 is assumed to be non-ferromagnetic, then  $\mu_1 = \mu_2$  and the first term of Equation (3.2.9) vanishes. The resulting equation is

$$\frac{\omega_2 - \omega_1}{\omega_2} = \frac{-\frac{(\epsilon_{r2} - 1)}{2} \int_{V_\epsilon} \vec{E}_1 \cdot \vec{E}_2 dV}{\int_{V_c} |\vec{E}_1|^2 dV} \quad (3.2.10)$$

where  $\epsilon_{r2}$  is the relative complex permittivity.

### 3.2.3 Resonant Frequency and Q Factor Relationships

The fields under consideration can be assumed to vary with time  $t$  as the function  $e^{j\omega t}$  where the angular frequency  $\omega$  can be complex for a dissipative system, i.e.,

$$\omega = \omega' + j \omega'' \quad (3.2.11)$$

The real part,  $\omega'$ , can be written as

$$\omega' = 2 \pi f \quad (3.2.12)$$

where  $f$  is frequency.

Energy is proportional to field quantities squared, so the corresponding time-domain temporal dependence will be  $e^{j2\omega t}$ . Energy dissipation is a decreasing function associated with the imaginary component of the frequency and includes the form  $e^{-2\omega'' t}$  [40]. The energy dissipated over a short time  $\Delta\tau$ , assuming unit energy at time  $t = 0$ , is  $(1 - e^{-2\omega'' \Delta\tau})$ . Expanding the exponential term in a Taylor series:

$$e^{-2\omega'' \Delta\tau} = 1 - 2\omega'' \Delta\tau + 2 \omega''^2 \Delta\tau^2 + \dots$$

and neglecting the terms of order  $\Delta\tau^2$  and greater, the resulting approximation is

$$e^{-2\omega'' \Delta\tau} \cong 1 - 2\omega'' \Delta\tau$$

This approximation leads to an energy dissipation per unit energy, over the short time interval  $\Delta\tau$ , of

$$1 - (1 - 2\omega'' \Delta\tau) = 2\omega'' \Delta\tau \quad (3.2.13)$$

and a corresponding power dissipation per unit energy of  $2\omega''$ . If  $U_T$  is defined as the total average energy of the system, then the average dissipation of power is  $2\omega'' U_T$ .

The definition of the quality factor  $Q$  is

$$\begin{aligned} Q_L &= \frac{\omega' (\text{Stored Energy in a Cavity})}{(\text{Average Power Loss})} \\ &= \frac{\omega' U_T}{2\omega'' U_T} = \frac{\omega'}{2\omega''} \end{aligned} \quad (3.2.14)$$

This particular  $Q$  factor ( $Q_L$ ) accounts for all dissipative effects in the system.

The complex frequency and Q factors can now be related to the permittivity and field quantities in Equation (3.2.10). Upon substitution of complex frequencies, the left-hand term of Equation (3.2.10) becomes

$$\frac{\omega_2 - \omega_1}{\omega_2} = \frac{(\omega'_2 - \omega'_1) + j(\omega''_2 - \omega''_1)}{\omega'_2 \left( 1 + j \frac{\omega''_2}{\omega'_2} \right)} \quad (3.2.15)$$

If the cavity is now taken to be resonant in both conditions 1 and 2, designated by resonant frequencies  $f_{r1}$  and  $f_{r2}$ , Equation (3.2.15) becomes

$$\frac{\omega_2 - \omega_1}{\omega_2} = \left( 1 + j \frac{\omega''_{r2}}{\omega'_{r2}} \right)^{-1} \left( \frac{f_{r2} - f_{r1}}{f_{r2}} + j \left( \frac{\omega''_{r2}}{\omega'_{r2}} - \frac{\omega''_{r1}}{\omega'_{r2}} \right) \right) \quad (3.2.16)$$

Assuming a small frequency shift due to material perturbation (i.e.,  $\omega'_1 \cong \omega'_2$ ) and employing the Q factor definition of Equation (3.2.14), Equation (3.2.16) becomes

$$\frac{\omega_2 - \omega_1}{\omega_2} = \left( 1 + j \frac{1}{2Q_{L2}} \right)^{-1} \left( \frac{f_{r2} - f_{r1}}{f_{r2}} + j \left( \frac{1}{2Q_{L2}} - \frac{1}{2Q_{L1}} \right) \right) \quad (3.2.17)$$

If a low-loss material ( $\omega_2'' \ll \omega_2'$ ) is inserted into the resonant cavity (thereby maintaining a large Q), then  $(2Q_{L2})^{-1} \ll 1$ , so Equation (3.2.17) can be written

$$\frac{\omega_2 - \omega_1}{\omega_2} = \frac{f_{r2} - f_{r1}}{f_{r2}} + \frac{j}{2} \left( \frac{1}{Q_{L2}} - \frac{1}{Q_{L1}} \right) \quad (3.2.18)$$

Combining Equations (3.2.18) and (3.2.10) yields

$$\frac{-\frac{(\epsilon_{r2} - 1)}{2} \int_{V_\epsilon} \vec{E}_1 \cdot \vec{E}_2 dV}{\int_{V_c} |\vec{E}_1|^2 dV} = \frac{f_{r2} - f_{r1}}{f_{r2}} + \frac{j}{2} \left( \frac{1}{Q_{L2}} - \frac{1}{Q_{L1}} \right) \quad (3.2.19)$$

### 3.2.4 Material Geometry and Field Relationships

In order to solve Equation (3.2.19) for the material's relative permittivity  $\epsilon_{r2}$  (to be known as the complex permittivity  $\epsilon^*$  hereafter), the relationship between the electric field vectors  $\vec{E}_2$  and  $\vec{E}_1$  must be determined. Several sample geometries lend themselves to internal ( $\vec{E}_2$ ) field approximations for specific unperturbed ( $\vec{E}_1$ ) field conditions [39]. The most commonly used sample geometry is that of a small rod inserted completely through holes in the broad walls of a rectangular waveguide cavity resonating in a  $TE_{10n}$  mode, as in Figure 3.2.1. In this configuration, all points on the sample surface are tangent to the unperturbed electric field lines. Since the tangential electric field components must be continuous across the boundary of a dielectric, the approximation

$$\vec{E}_2 \cong \vec{E}_1 \quad (3.2.20)$$

holds, given that the sample is very small relative to the resonant wavelength. Note that, while a rod geometry has been mentioned here, a bundle of material strands or a sample with flat surfaces may be used as long as the sample cross-section is small.

In a cavity of length  $3d$  in the  $z$  direction, where  $d$  is the length of a single period of the mode structure in the  $TE_{103}$  mode, the only electric field component in the assumed  $TE_{10n}$  mode is

$$E_y = E_0 \sin \frac{\pi x}{a} \sin \frac{n\pi z}{3d} \quad (3.2.21)$$

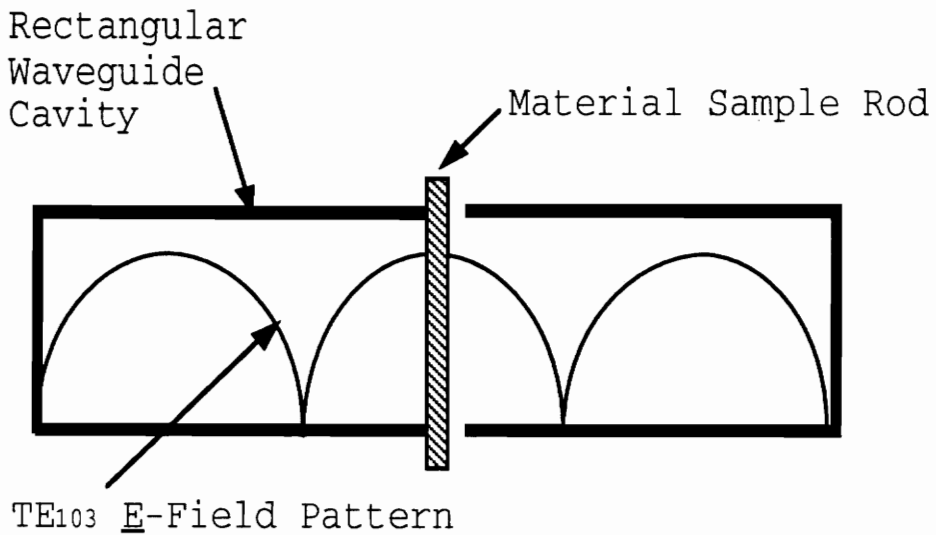
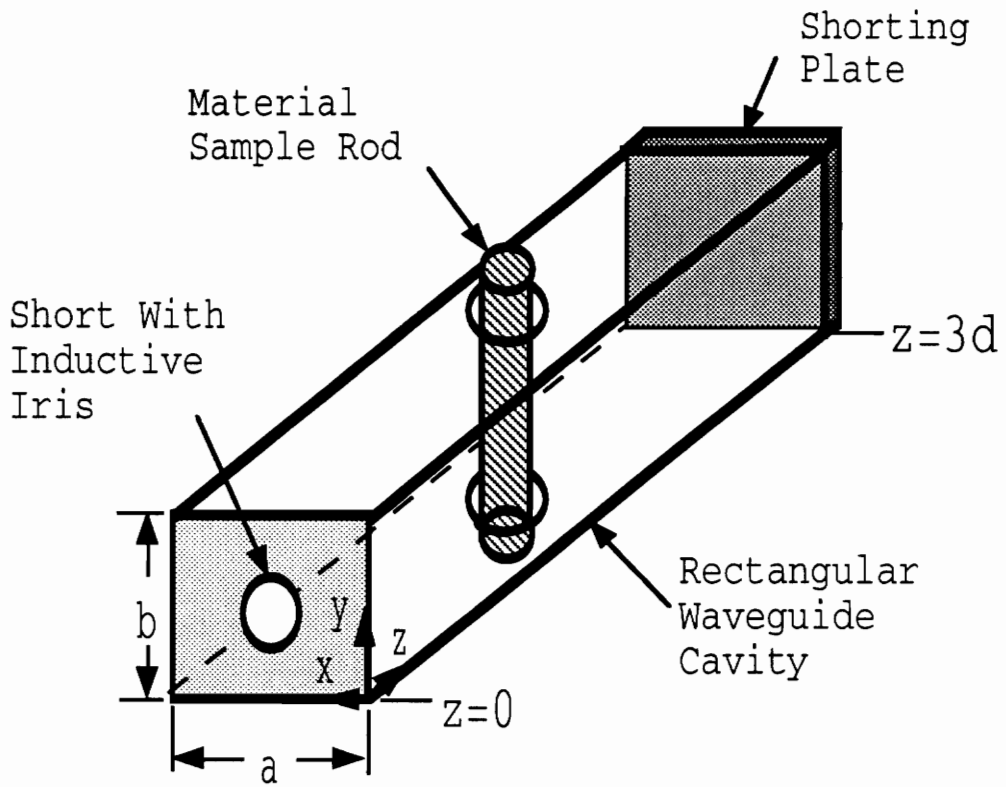


Figure 3.2.1: Schematic of the cavity perturbation measurement configuration for a rectangular cavity resonating in the  $TE_{103}$  mode.

Using the approximation of Equation (3.2.20) for this geometry, and the electric field component  $E_y$  of Equation (3.2.21), the integrals in Equation (3.2.19) can be solved. The denominator integral, taken over the entire cavity volume, becomes

$$\begin{aligned}
 & \int_{V_c} |E_y|^2 dV \\
 &= E_0^2 \int_0^a \sin^2 \frac{\pi x}{a} dx \int_0^{3d} \sin^2 \frac{n\pi z}{3d} dz \int_0^b dy \quad (3.2.22) \\
 &= E_0^2 \frac{a}{2} \frac{3d}{2} b = E_0^2 \frac{V_c}{4}
 \end{aligned}$$

Since the integral in the numerator of Equation (3.2.19) is taken only over the very small dimensions of the material sample, the electric field component  $E_y$  can be assumed to be constant, i.e., it does not vary spatially. This assumption results in the approximation

$$\int_{V_\epsilon} |E_y|^2 dV \cong E_0^2 V_\epsilon \quad (3.2.23)$$

Substituting the results of Equations (3.2.22) and (3.2.23) into Equation (3.2.19), and solving for the complex material permittivity  $\epsilon^*$  gives

$$\epsilon^* = \frac{V_c}{V_\epsilon} \left[ \frac{f_{r1} - f_{r2}}{2 f_{r1}} - \frac{j}{4} \left( \frac{1}{Q_{L2}} - \frac{1}{Q_{L1}} \right) \right] + 1 \quad (3.2.24)$$

The complex material permittivity in Equation (3.2.24) can be separated into its real and imaginary components to give the dielectric constant  $\epsilon'$  and loss factor  $\epsilon''$

$$\epsilon' = \frac{V_c}{2 V_\epsilon} \frac{(f_{r1} - f_{r2})}{f_{r1}} + 1 \quad (3.2.25a)$$

$$\epsilon'' = \frac{V_c}{4 V_\epsilon} \left( \frac{1}{Q_{L2}} - \frac{1}{Q_{L1}} \right) \quad (3.2.25b)$$

Note that Equations (3.2.25a) and (3.2.25b) reflect the physics of material perturbation; the dielectric constant  $\epsilon'$  is a function of the real frequency shift related to energy storage, while the dielectric loss factor  $\epsilon''$  depends on Q factors that represent power dissipation mechanisms. Once the cavity and sample dimensions are known, Equations (3.2.25a) and (3.2.25b) require measurement of only the unperturbed (empty) and perturbed (sample loaded) resonant frequencies and Q factors to compute the complex permittivity of the material. These equations, while very simple in form, provide very accurate permittivities for low-loss materials assuming that the Q and resonant frequency  $f_r$  data are accurate.

### 3.3 Reflection Cavity Formulation

As with the development of the cavity perturbation equations, the reflection cavity formulation will start from basic definitions. The very name of the measurement technique provides some insight: a specimen is to be placed against the shorted end of a waveguide cavity, the frequency swept until resonance occurs, and the  $Q$  and resonant frequency,  $f_r$ , are to be measured. A comparison of the  $Q$  and  $f_r$  for an empty and material loaded cavity lead to a computation of the complex permittivity  $\epsilon^*$ .

#### 3.3.1 Q Factor Relations

Recall the definition of a quality factor  $Q$  from Equation (3.2.14)

$$Q = \omega_r \frac{(\text{Stored Energy})}{(\text{Average Power Loss})} \quad (3.3.1)$$

where  $\omega_r$  is the circular frequency at resonance. Now define  $U_T$  to be the total energy stored in the electric and magnetic fields. In Section (3.2.5), the stored electric and magnetic field energies were shown to be equal at resonance. Likewise, recall the integral forms of energies  $U_E$  and  $U_H$  given in Equations (A.28a) and (A.28b). These energies can be written

$$U_E = \frac{\epsilon_0}{2} \int_{V_c} \epsilon' |E|^2 dV \quad (3.3.2a)$$

$$U_H = \frac{\mu_0}{2} \int_{V_c} \mu' |H|^2 dV \quad (3.3.2b)$$

where  $V_c$  is the cavity volume. Note that  $\epsilon'$  and  $\mu'$  are, in general, real and are tensor quantities that can be anisotropic.

Power losses in the resonant system are mainly attributable to 1) energy dissipation in the imperfectly conducting cavity walls and any lossy dielectric occupying the

cavity, and 2) losses to the external electrical circuit. [39] These power losses, when expressed as Q factors as in Equation (3.3.1), are related by

$$\frac{1}{Q_L} = \frac{1}{Q_U} + \frac{1}{Q_E} \quad (3.3.3)$$

where  $Q_L$  represents the total power loss in the system  
 $Q_U$  represents power loss in the resonant cavity  
and  $Q_E$  represents power loss to the external circuit.

Wall conductivity power losses ( $P_w$ ) are given by [39]

$$P_w = \frac{1}{2} \int_{S_c} R_s |J_{surf}|^2 dS \quad (3.3.4)$$

where  $S_c$  = total surface area of the cavity walls  
 $R_s$  = surface resistivity per unit area  
 $J_{surf}$  = maximum instantaneous surface current density.

The surface resistivity for smooth walls has the form [33]

$$R_s = \sqrt{\frac{\pi f \mu_m}{\sigma_m}} \quad (3.3.5)$$

where  $f$  = frequency  
 $\mu_m$  = magnetic permeability of the walls  
(assumed to be  $\mu_0$  for non-ferromagnetic waveguides)  
 $\sigma_m$  = metal conductivity.

The boundary conditions on Maxwell's equations at the surface of a perfect conductor state that [33]

$$\vec{J}_{surf} = \vec{n} \times \vec{H} \quad (3.3.6)$$

where  $\vec{n}$  is the unit vector normal to the cavity wall surface and  $\vec{H}$  is the magnetic field component at the surface. Equation (3.3.4) can be rewritten using Equation (3.3.6) as

$$P_W = \frac{1}{2} \int_{S_c} R_s |H_T|^2 dS \quad (3.3.7)$$

where  $H_T$  is the tangential magnetic field component.

Power dissipation  $P_\epsilon$  in a dielectric material within the cavity is given by

$$P_\epsilon = \frac{1}{2} \int_{V_\epsilon} \sigma_\epsilon |E|^2 dV \quad (3.3.8)$$

where  $\sigma_\epsilon$  is the conductivity tensor of the dielectric material and  $V_\epsilon$  is the volume of the dielectric. As described in Section (A.2) materials with low electrical conductivity are more properly described in terms of dielectric loss. Such insulators have conductivities described by

$$\sigma_\epsilon = \omega \epsilon_0 \epsilon' \tan \delta = \omega \epsilon_0 \epsilon'' \quad (3.3.9)$$

where  $\tan \delta$  is the dielectric loss tangent. In these terms, Equation (3.3.8) becomes

$$P_\epsilon = \frac{\omega \epsilon_0}{2} \int_{V_\epsilon} \epsilon'' |E|^2 dV \quad (3.3.10)$$

Note that, in general,  $\epsilon''$  is a tensor quantity that can be anisotropic.

The quality factor of the "unloaded" cavity  $Q_U$ , i.e., the cavity without the "load" of the external circuit, can be written following Equation (3.3.1)

$$Q_U = \frac{\omega_r U_T}{P_W + P_\epsilon} \quad (3.3.11)$$

It should be emphasized that Equation (3.3.11) applies only at resonance. An empty cavity experiences losses due only to wall conductivity, thus  $P_\epsilon = 0$  and  $\epsilon' = 1$ . At resonance the total energy ( $U_T$ ) can be expressed as the electric field energy ( $U_E$ ) alone, since the electric and magnetic energies

are equal and in time quadrature. For the empty cavity Equation (3.3.2a) reduces to

$$U_T = \frac{\epsilon_0}{2} \int_{V_c} |E|^2 dV \quad (3.3.12)$$

The empty cavity quality ( $Q_{U0}$ ) can now be written

$$Q_{U0} = \frac{\omega_{r0} \epsilon_0 \int_{V_c} |E|^2 dV}{\int_{S_c} R_s |H_T|^2 dS} \quad (3.3.13)$$

A cavity containing a dielectric material will experience power dissipation described by Equations (3.3.7) and (3.3.10), with stored energy given by

$$U_T = \frac{\epsilon_0}{2} \left( \int_{V_\epsilon} \epsilon' |E|^2 dV + \int_{V_c - V_\epsilon} |E|^2 dV \right) \quad (3.3.14)$$

and a quality ( $Q_{U1}$ ) of

$$Q_{U1} = \frac{\omega_{r1} \epsilon_0 \left( \int_{V_\epsilon} \epsilon' |E|^2 dV + \int_{V_c - V_\epsilon} |E|^2 dV \right)}{\int_{S_c} R_s |H_T|^2 dS + \omega_{r1} \epsilon_0 \int_{V_\epsilon} \epsilon'' |E|^2 dV} \quad (3.3.15)$$

### 3.3.2 The TE<sub>103</sub> Cavity

The previously derived quality factors apply to a cavity of arbitrary geometry having conductive walls, containing a dielectric material of unspecified shape, and resonating in an arbitrary mode. Upon specifying the cavity geometry and resonant mode, the field quantities necessary for evaluation of Equations (3.3.13) and (3.3.15) can be determined.

The cavity geometry chosen in this work is a rectangular waveguide shorted on one end by a metal plate, and coupled to

an external waveguide circuit through a circular inductive iris, as shown in Figure 3.3.1. The length of the cavity is  $3d$ , where  $d$  is a guide half-wavelength ( $\lambda_g/2$ ) of the empty cavity at resonance. Standard broad (x-direction) and narrow (y-direction) dimensions are designated  $a$  and  $b$ , respectively. The  $z$ -direction is the direction of propagation. Perfect shorts are assumed at  $z = 0$  (the iris) and at  $z = 3d$  (shorting plate). A dielectric sample of thickness  $l_\epsilon$  is placed into the waveguide with one face in complete contact with the shorting plate. The distance from the iris to the nearest face of the sample is designated  $z = l_0$ , leading to the simple relationship at the plane of the short

$$z = 3d = l_0 + l_\epsilon$$

Recalling waveguide theory from Section (3.1), the  $TE_{10}$  mode is the dominant mode of propagation in a rectangular waveguide with  $a > b$ . This implies that, over a certain frequency band, only the  $TE_{10}$  mode will exist; therefore this is the mode assumed to exist in the resonant cavity. With the condition of a three period standing wave at resonance ( $l = 3d$ ), the resonant mode becomes the  $TE_{103}$  mode. Field relationships for the  $TE_{10n}$  modes are, using transmission line formalism of voltage ( $V$ ) and current ( $I$ ) [39,41],

$$\begin{aligned} E_y &= E_0 \sin \frac{\pi x}{a} \sin \frac{\pi z}{3d} \\ &= -\sqrt{\frac{2}{ab}} V(z) \frac{\pi x}{a} \end{aligned} \quad (3.3.16a)$$

$$H_x = \sqrt{\frac{2}{ab}} I(z) \sin \frac{\pi x}{a} \quad (3.3.16b)$$

$$H_z = -\frac{j\lambda}{\eta a \sqrt{2ab}} V(z) \cos \frac{\pi x}{a} \quad (3.3.16c)$$

where

$I(z)$  = effective current as a function of  $z$

$V(z)$  = effective voltage as a function of  $z$

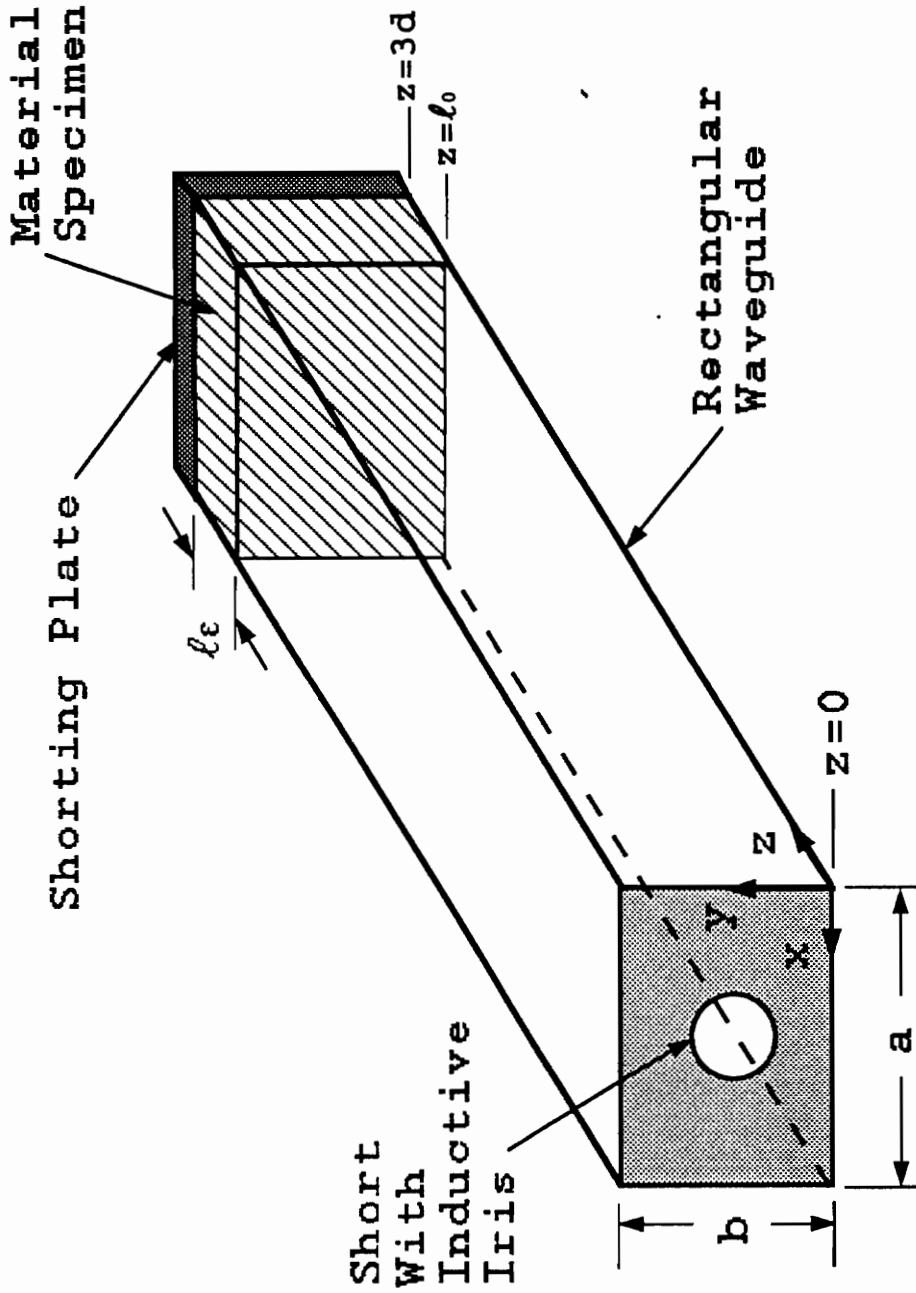


Figure 3.3.1: Schematic of the reflection cavity measurement configuration.

Note that the intrinsic impedance  $\eta$  and unbounded wavelength  $\lambda$  are functions of  $z$  in that they depend upon the medium of propagation; thus they change at the air-sample interface located at  $z = \ell_0$ .

Equations (3.3.16a) through (3.3.16c) describe all of the TE<sub>103</sub> field components in terms of two unknowns,  $V(z)$  and  $I(z)$ . If impedances relating voltage and current can be determined for all regions of the cavity, the number of unknowns will reduce to one. This single unknown can be carried through the integrals of Equations (3.3.13) and (3.3.15) and will cancel in the division. The task is to define  $V(z)$  and  $I(z)$  in terms of a consistent unknown and impedances.

An expansion of the forward propagating voltage and current waves yields

$$\begin{aligned} V(z) &= V(z_0) e^{-\gamma(z-z_0)} \\ &= V(z_0) \cos \gamma(z - z_0) \\ &\quad -j Z_0 I(z_0) \sin \gamma(z - z_0) \end{aligned} \tag{3.3.17a}$$

$$\begin{aligned} I(z) &= I(z_0) e^{-\gamma z} \\ &= I(z_0) \cos \gamma(z - z_0) \\ &\quad -j \frac{V(z_0)}{Z_0} \sin \gamma(z - z_0) \end{aligned} \tag{3.3.17b}$$

where

$Z_0$  = the characteristic impedance of the medium

$z_0$  = a reference point along the cavity axis

### 3.3.3 The Empty Cavity Condition

Consider the empty cavity in the TE<sub>103</sub> resonant mode as the first application of Equations (3.3.17a) and (3.3.17b). There is a short at  $z = 0$  (the iris), such that  $V(0) = 0$  and

$I(0)$  is a function of the input power only. Setting  $z_0 = 0$  in Equations (3.3.17a) and (3.3.17b) at resonance leads to

$$V(z) = -j Z_{r0} I(0) \sin(\beta_{r0} z) \quad (3.3.18a)$$

$$I(z) = I(0) \cos(\beta_{r0} z) \quad (3.3.18b)$$

where  $Z_{r0}$  = characteristic impedance of air at resonance

$$= \frac{\omega_{r0} \mu_0}{\beta_{r0}}$$

$\beta_{r0}$  = propagation phase constant of air at resonance

$$= \frac{2\pi}{\lambda_{gr0}}$$

and  $\lambda_{gr0}$  = guide wavelength in air at resonance

$$= 2d$$

Note that in lossless air,  $\gamma$  is replaced by  $\beta_{r0}$  in Equations (3.3.17a) and (3.3.17b).

### 3.3.4 The Material Loaded Cavity Condition

A simple network transmission line model can be employed in the analysis of the sample loaded cavity. This network model, shown in Figure 3.3.2, consists of an empty cavity of length  $\ell_0$  characterized by  $Z_{r1}$  and  $\beta_{r1}$ . The sample occupies the cavity from  $z = \ell_0$  to  $z = 3d$ , with the properties  $Z_{\epsilon r1}$  and  $\beta_{\epsilon r1}$ . Note that these conditions hold for the cavity in resonance, denoted by the subscript  $r$ .

The voltage and current Equations (3.3.17a) and (3.3.17b) over the empty cavity section, with  $V(0) = 0$ , are

$$V(z) = -j Z_{r1} I(0) \sin(\beta_{r1} z) \quad (3.3.19a)$$

$$I(z) = I(0) \cos(\beta_{r1} z) \quad (3.3.19b)$$

where  $0 < z < \ell_0$ .

Likewise, at the air/sample interface ( $z = \ell_0$ )

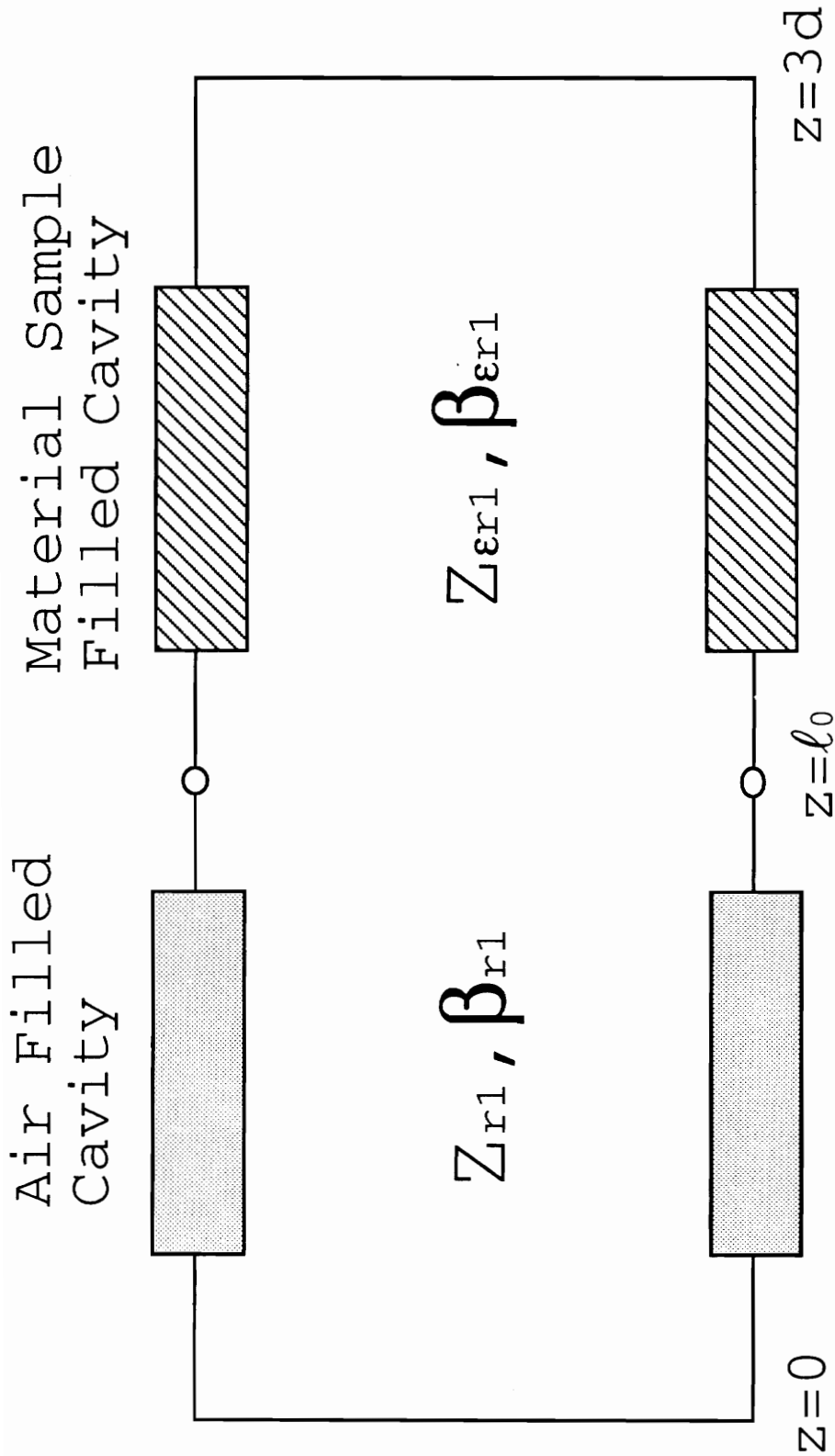


Figure 3.3.2: Network model of the material loaded reflection cavity.

$$V(\ell_0) = -j Z_{r1} I(0) \sin(\beta_{r1} \ell_0) \quad (3.3.20a)$$

$$I(\ell_0) = I(0) \cos(\beta_{r1} \ell_0) \quad (3.3.20b)$$

The sample filled cavity section is treated as a new region by shifting the z-axis reference point from  $z = 0$  to  $z = \ell_0$ . Thus,  $z_0 = \ell_0$  in Equations (3.3.17a) and (3.3.17b), resulting in

$$\begin{aligned} V(z) &= V(\ell_0) \cos \beta_{er1}(z - \ell_0) \\ &\quad -j Z_{er1} I(\ell_0) \sin \beta_{er1}(z - \ell_0) \end{aligned} \quad (3.3.21a)$$

$$\begin{aligned} I(z) &= I(\ell_0) \cos \beta_{er1}(z - \ell_0) \\ &\quad -j \frac{1}{Z_{er1}} V(\ell_0) \sin \beta_{er1}(z - \ell_0) \end{aligned} \quad (3.3.21b)$$

### 3.3.5 Integration of Field Quantities

The voltage and current equations (3.3.18a), (3.3.18b), and (3.3.19) through (3.3.21) describe the entire cavity in terms of known quantities ( $Z_{r0}, \beta_{r0}, Z_{r1}, \beta_{r1}$ ), terms containing only the unknowns that are the desired components dependent upon permittivity ( $Z_{er1}, \beta_{er1}$ ), and the constant  $I(0)$ . Once the equations for  $V(z)$  and  $I(z)$  are substituted back into the field equations (3.3.16a) through (3.3.16c), which contain no further unknowns, the integrals in the Q-factor relationships of Equations (3.3.13) and (3.3.15) can be solved.

Several elementary, but useful, integral solutions are presented here as templates to facilitate the solution of the EM field integrals:

$$\int_0^a \sin^2 \frac{\pi x}{a} dx = \int_0^a \cos^2 \frac{\pi x}{a} dx = \frac{a}{2}$$

$$\begin{aligned} \int_0^{3d} \cos^2 \beta_{r0} z dz &= \int_0^{3d} \sin^2 \beta_{r0} z dz = \int_0^{3d} \sin^2 \frac{\pi z}{d} \\ &= \frac{3d}{2} = \frac{3\lambda_{gr0}}{4} \end{aligned}$$

There are several integrals that occur repeatedly, so they are defined as constants  $S_i$ :

$$S_1 = \int_0^{\ell_0} \sin^2 \beta_{r1} z \, dz = \frac{\ell_0}{2} - \frac{\sin 2\beta_{r1}\ell_0}{4\beta_{r1}}$$

$$S_2 = \int_0^{\ell_0} \cos^2 \beta_{r1} z \, dz = \frac{\ell_0}{2} + \frac{\sin 2\beta_{r1}\ell_0}{4\beta_{r1}}$$

$$S_3 = \int_{\ell_0}^{3d} \sin^2 \beta_{er1} (z - \ell_0) \, dz = \frac{\ell_\epsilon}{2} - \frac{\sin 2\beta_{er1}\ell_\epsilon}{4\beta_{er1}}$$

$$S_4 = \int_{\ell_0}^{3d} \cos^2 \beta_{er1} (z - \ell_0) \, dz = \frac{\ell_\epsilon}{2} + \frac{\sin 2\beta_{er1}\ell_\epsilon}{4\beta_{er1}}$$

$$S_5 = \int_{\ell_0}^{3d} \sin \beta_{er1} (z - \ell_0) \cos \beta_{er1} (z - \ell_0) \, dz = \frac{\sin^2 \beta_{er1}\ell_\epsilon}{2\beta_{er1}}$$

It is useful to define commonly occurring integrals of voltage and current. Note that each result has a common factor of  $I^2(0)$ ; since the solution to the integral is  $(I^2(0) \times S_i)$ ,  $S_i$  represents only the multiplier for  $I^2(0)$ .

For the case of an empty cavity, using Equations (3.3.18a) and (3.3.18b), the resulting integrals are

$$\int_0^{3d} V^2(z) \, dz = -I^2(0) z_{r0}^2 \frac{3d}{2}$$

$$\therefore S_6 = -z_{r0}^2 \frac{3d}{2}$$

$$\int_0^{3d} I^2(z) \, dz = I^2(0) \frac{3d}{2}$$

$$\therefore S_7 = \frac{3d}{2}$$

Integrating quantities in Equations (3.3.19a) and (3.3.19b), and (3.3.21a) and (3.3.21b) for the sample loaded cavity leads to

$$\int_0^{\ell_0} V^2(z) dz = -I^2(0) Z_{r1}^2 \int_0^{\ell_0} \sin^2 \beta_{r1} z dz = -I^2(0) Z_{r1}^2 S_1$$

$$\therefore S_8 = -Z_{r1}^2 S_1$$

$$\int_0^{\ell_0} I^2(z) dz = I^2(0) \int_0^{\ell_0} \cos^2 \beta_{r1} z dz = I^2(0) S_2$$

$$\therefore S_9 = S_2$$

$$\int_{\ell_0}^{3d} V^2(z) dz = -I^2(0) \begin{pmatrix} S_4 Z_{r1}^2 \sin^2 \beta_{r1} \ell_0 \\ + S_3 Z_{er1}^2 \cos^2 \beta_{r1} \ell_0 \\ + S_5 Z_{r1} Z_{er1} \sin 2\beta_{r1} \ell_0 \end{pmatrix}$$

$$\therefore S_{10} = - \begin{pmatrix} S_4 Z_{r1}^2 \sin^2 \beta_{r1} \ell_0 \\ + S_3 Z_{er1}^2 \cos^2 \beta_{r1} \ell_0 \\ + S_5 Z_{r1} Z_{er1} \sin 2\beta_{r1} \ell_0 \end{pmatrix}$$

$$\int_{\ell_0}^{3d} I^2(z) dz = I^2(0) \begin{pmatrix} S_4 \cos^2 \beta_{r1} \ell_0 \\ + S_3 \left[ \frac{Z_{r1}}{Z_{er1}} \right]^2 \sin^2 \beta_{r1} \ell_0 \\ + S_5 \left[ \frac{Z_{r1}}{Z_{er1}} \right] \sin 2\beta_{r1} \ell_0 \end{pmatrix}$$

$$\therefore S_{11} = \begin{pmatrix} S_4 \cos^2 \beta_{r1} \ell_0 \\ + S_3 \left[ \frac{Z_{r1}}{Z_{er1}} \right]^2 \sin^2 \beta_{r1} \ell_0 \\ + S_5 \left[ \frac{Z_{r1}}{Z_{er1}} \right] \sin 2\beta_{r1} \ell_0 \end{pmatrix}$$

The voltage and current integrals can now be used to solve the integrals involving  $\vec{E}$  and  $\vec{H}$  field components. For an empty cavity, the integral in the numerator of Equation (3.3.13) is

$$\int_0^a \int_0^b \int_0^{3d} E_y^2 dz dy dx = I^2(0) S_6$$

$$\therefore S_{12} = S_6$$

The surface integral of the tangential  $\vec{H}$  fields in Equation (3.3.13) involve six integrals (one for each wall) for each field component. By symmetry, only three integrals need be evaluated [39]:

$$\begin{aligned} \text{at } x = 0, H_x = 0 \text{ and } |H_T|^2 &= |H_z|^2 \\ \text{at } z = 0, H_z = 0 \text{ and } |H_T|^2 &= |H_x|^2 \\ \text{at } y = 0, H_T &= x_0 H_x + y_0 H_y \\ \text{such that } |H_T|^2 &= |H_x|^2 + |H_y|^2 \end{aligned}$$

These integrals are written as follows:

$$\begin{aligned} \int_{S_c} |H_T|^2 ds = \\ \{1\} \int_0^a \int_0^b H_x^2 dy dx \Big|_{z=0,3d} + \{2\} \int_0^b \int_0^{3d} H_z^2 dz dy \Big|_{x=0,a} \\ + \{3\} 2 \int_0^a \int_0^{3d} H_x^2 dz dx \Big|_{y=0} + \{4\} 2 \int_0^a \int_0^{3d} H_z^2 dz dx \Big|_{y=0} \end{aligned}$$

Note that integrals {3} and {4} are doubled, since no  $y$  dependent function exists to make an integral at  $y = 0$  different from one at  $y = b$ .

Evaluating each of these integrals results in

$$\begin{aligned} \{1\} [z = 0, 3d] &= I^2(0) \\ \{2\} [x = 0, a] &= -\frac{\lambda^2}{2\eta^2 a^3} I^2(0) S_6 \end{aligned}$$

$$\{3\} [y = 0] = \frac{2}{b} I^2(0) S_7$$

$$\{4\} [y = 0] = -\frac{\lambda^2}{2\eta^2 a^2 b} I^2(0) S_6$$

Summing the results of integrals {1} through {4}, where {1} and {2} are added twice to account for the two z and x boundary conditions, respectively, and factoring  $I^2(0)$ , leads to

$$S_{13} = \left[ 2 + \frac{2}{b} S_7 - \frac{\lambda^2}{\eta^2 a^2} \left( \frac{1}{2b} + \frac{1}{a} \right) S_6 \right]$$

The integrals of the  $\vec{E}$  field in Equation (3.3.15) over the dielectric sample filled cavity and over the remaining empty cavity are

$$\int_0^a \int_0^b \int_0^{\ell_0} E_y^2 dz dy dx = I^2(0) S_8$$

$$\therefore S_{14} = S_8$$

$$\int_0^a \int_0^b \int_0^{\ell_0} E_y^2 dz dy dx = I^2(0) S_{10}$$

$$\therefore S_{15} = S_{10}$$

The surface integral of  $\vec{H}$  in Equation (3.3.15) is separated into two regions: the walls in contact with the dielectric sample ( $S_E$ ) and the walls contacting only air in the empty part of the cavity ( $S_I$ ). For the empty cavity, the integrals are

$$\begin{aligned} & \{1\} \int_{S_I} H_x^2 dy dx \Big|_{z=0} + \{2\} \int_{S_I} H_x^2 dy dx \Big|_{z=\ell_0} \\ & + \{3\} 2 \int_{S_I} H_x^2 dx dz \Big|_{y=0} + \{4\} 2 \int_{S_I} H_z^2 dz dx \Big|_{y=0} \\ & + \{6\} \int_{S_I} H_z^2 dz dy \Big|_{x=0} + \{6\} \int_{S_I} H_z^2 dz dy \Big|_{x=a} \end{aligned}$$

Likewise, for the sample filled cavity, the result is

$$\begin{aligned}
 & \{7\} \int_{S_\epsilon} H_x^2 dy dx \Big|_{z=\ell_0} + \{8\} \int_{S_\epsilon} H_x^2 dy dx \Big|_{z=3d} \\
 & + \{9\} 2 \int_{S_\epsilon} H_x^2 dx dz \Big|_{y=0} + \{10\} 2 \int_{S_\epsilon} H_z^2 dz dx \Big|_{y=0} \\
 & + \{11\} \int_{S_\epsilon} H_z^2 dz dy \Big|_{x=0} + \{12\} \int_{S_\epsilon} H_z^2 dz dy \Big|_{x=a}
 \end{aligned}$$

The solutions to these integrals are

$$\begin{aligned}
 \{1\} &= I^2(0) \\
 \{2\} &= I^2(0) \cos^2(\beta_{r1}\ell_0) \\
 \{3\} &= I^2(0) \frac{2}{b} S_9 \\
 \{4\} &= I^2(0) \frac{-\lambda_{r1}^2}{2\eta_0^2 a^2 b} S_8 \\
 \{5\} &= I^2(0) \frac{-\lambda_{r1}^2}{2\eta_0 a^3} S_8 \\
 \{6\} &= I^2(0) \frac{-\lambda_{r1}^2}{2\eta_0 a} S_8 \\
 \{7\} &= I^2(0) \cos^2(\beta_{r1}\ell_0) \\
 \{8\} &= I^2(0) \left[ \begin{array}{c} \cos(\beta_{r1}\ell_0) \cos(\beta_{\epsilon r1}\ell_\epsilon) \\ -\frac{Z_{r1}}{Z_{\epsilon r1}} \sin(\beta_{r1}\ell_0) \sin(\beta_{\epsilon r1}\ell_\epsilon) \end{array} \right]^2 \\
 \{9\} &= I^2(0) \frac{2}{b} S_{11} \\
 \{10\} &= I^2(0) \frac{-\lambda_{\epsilon r1}^2}{2\eta_\epsilon^2 a^2 b} S_{10}
 \end{aligned}$$

$$\{11\} = I^2(0) \frac{-\lambda_{\epsilon r 1}^2}{2\eta_{\epsilon}^2 a^3} S_{10}$$

$$\{12\} = I^2(0) \frac{-\lambda_{\epsilon r 1}^2}{2\eta_{\epsilon}^2 a^3} S_{10}$$

Summing {1} through {12} and factoring  $I^2(0)$  leads to:

$$S_{16} = \left[ \begin{aligned} &1 + 2 \cos^2(\beta_{r1}\ell_0) + \frac{2}{b} (S_9 + S_{11}) \\ &+ \left[ \cos(\beta_{r1}\ell_0) \cos(\beta_{\epsilon r 1}\ell_{\epsilon}) - \frac{Z_{r1}}{Z_{\epsilon r 1}} \sin(\beta_{r1}\ell_0) \sin(\beta_{\epsilon r 1}\ell_{\epsilon}) \right]^2 \\ &- \frac{\lambda_{r1}^2}{2\eta_0^2 a^2} \left[ \frac{1}{b} + \frac{2}{a} \right] S_8 - \frac{\lambda_{\epsilon r 1}^2}{2\eta_{\epsilon}^2 a^2} \left[ \frac{1}{b} + \frac{2}{a} \right] S_{10} \end{aligned} \right]^2$$

### 3.3.6 Solution for Permittivity Components

The quality factor equations can now be simplified using  $S_{12}$ ,  $S_{13}$  and Equation (3.3.5). Equation (3.3.13) becomes

$$Q_{u0} = \frac{\omega_{r0} \epsilon_0 S_{12}}{S_{13} \sqrt{\frac{f_{r0} \pi \mu_m}{\sigma_m}}} \quad (3.3.22)$$

Equation (3.3.15) reduces to

$$Q_{u1} = \frac{\omega_{r1} \epsilon_0 (\epsilon' S_{15} + S_{14})}{S_{16} \sqrt{\frac{f_{r1} \pi \mu_m}{\sigma_m}} + \omega_{r1} \epsilon_0 \epsilon'' S_{15}} \quad (3.3.23)$$

Note that if the tensor quantities  $\epsilon'$  and  $\epsilon''$  in Equation (3.3.15) are considered to be oriented in principal directions (i.e., only diagonal permittivity components exist), then only a single permittivity component multiplies the  $TE_{10}$  mode's lone electric field component  $E_y$  described in Equation (3.3.16a). This fact allows the permittivity components to be

factored out of the integration of the electric field in Equations (3.3.2a) and (3.3.10); these permittivity components appear as constant multipliers of the same integral,  $S_{15}$ , in the numerator and denominator Equation (3.3.23). If the sample is not oriented in a principal direction then the permittivity components in Equation (3.3.23) represent non-principal values that have undergone a tensor rotation. This orientation dependence is described further in Section (2.3.2) and is a point of study in this work.

Recall that the solutions of the integrals in the Q equations leads to a factor of  $I^2(0)$  that cancels in division, leaving the known  $S_i$  terms. In order to eliminate the unknown  $\sqrt{\sigma_m}$ , Equation (3.3.22) can be rearranged as

$$\sqrt{\sigma_m} = \frac{\sqrt{f_{r0} \pi \mu_m} Q_{u0} S_{13}}{\omega_{r0} \epsilon_0 S_{12}} \quad (3.3.24)$$

When this result is substituted into Equation (3.3.23),  $\epsilon''$  can be isolated as:

$$\epsilon'' = \frac{1}{S_{15}} \left[ \frac{S_{14} + \epsilon' S_{15}}{Q_{u1}} - \frac{S_{16} S_{12}}{S_{13} Q_{u0}} \sqrt{\frac{f_{r0}}{f_{r1}}} \right] \quad (3.3.25)$$

Note that Equation (3.3.25) contains only  $S_i$  terms, measurable  $f_r$  and Q quantities, and  $\epsilon'$ . Since  $\epsilon'$  appears explicitly in Equation (3.3.25) and is implicitly embedded in some  $S_i$  terms (in  $\eta_\epsilon$  and  $\beta_{\epsilon r1}$ ), a solution for  $\epsilon'$  must precede the solution of Equation (3.3.25) for  $\epsilon''$ .

The solution method for  $\epsilon'$  is based upon the continuity of the input impedance at the dielectric sample/empty cavity interface. Figure 3.3.3 is a diagram of a cavity of length  $3d$  loaded with a sample of thickness  $l_\epsilon$  flush against a terminal short. The material/air interface at  $z = l_0$  is characterized by single value of impedance. However, it can be recalled from Equation (A.50) that the input impedance ( $Z_{in}$ ) of a

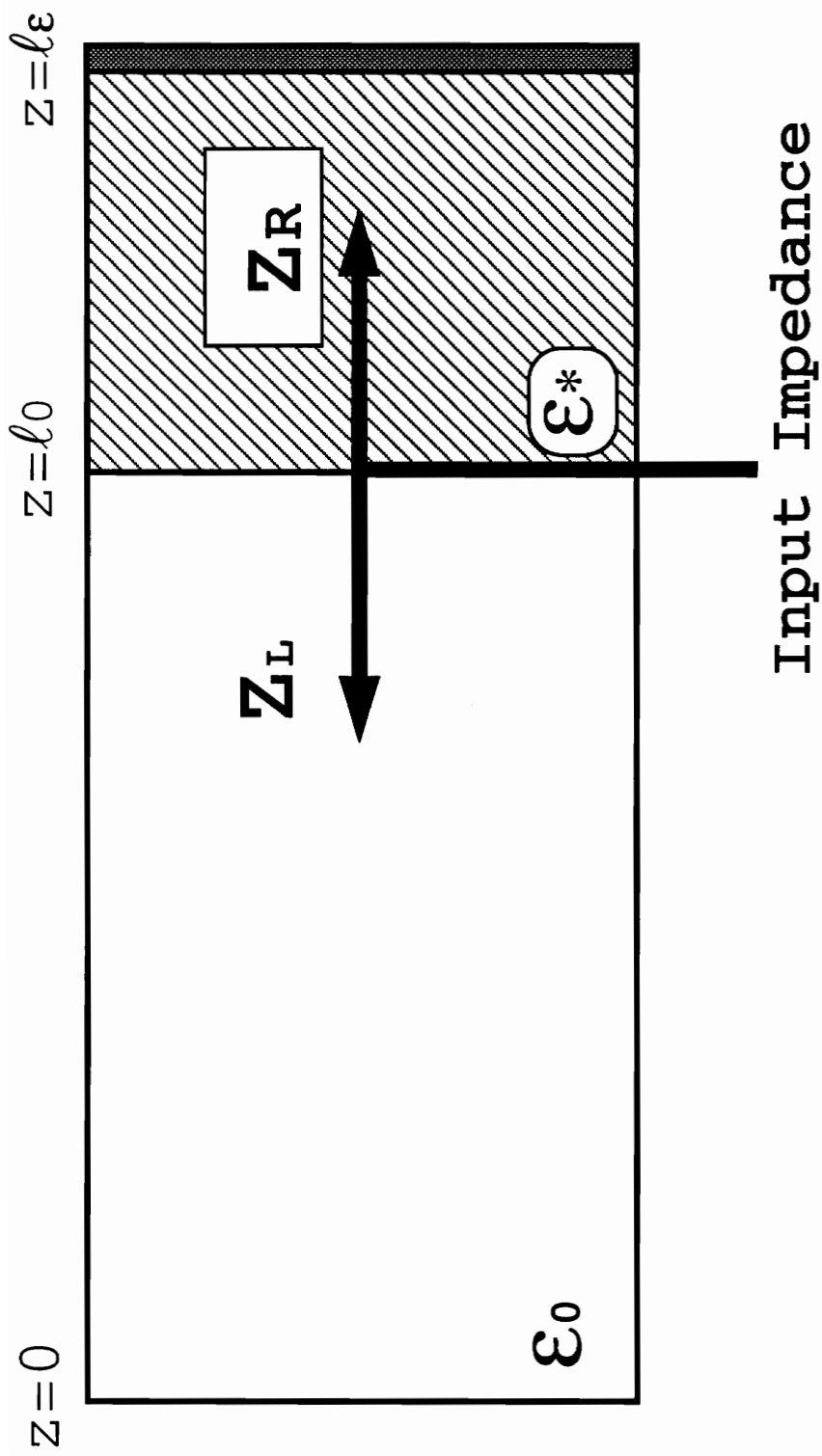


Figure 3.3.3: Impedance matching at the material interface in the reflection cavity.

section of a transmission line, determined by hypothetically "looking down" the line in some direction, is a function of the characteristic impedance ( $Z_0$ ), the load impedance ( $Z_L$ ), the phase constant ( $\beta$ ), and the line length ( $\ell$ ). Both the iris and the short are considered to be perfect shorting conductors, so  $Z_L = 0$  in Equation (A.50). Thus, the input impedance looking left from  $z = \ell_0$  toward the iris is

$$Z_{Lf} = jZ_{r1} \tan(\beta_{r1}\ell_0)$$

while the input impedance looking right from  $z = \ell_0$  through the sample toward the shorting plate is

$$Z_R = -jZ_{\epsilon r1} \tan(\beta_{\epsilon r1}\ell_\epsilon)$$

Note the sign change in  $Z_R$  due to the change in direction along the waveguide axis through which the input impedance is being viewed.

Equating these input impedances results in

$$\begin{aligned} Z_{Lf} &= Z_R \\ -\tan(\beta_{r1}\ell_0) &= \frac{Z_{\epsilon r1}}{Z_{r1}} \tan(\beta_{\epsilon r1}\ell_\epsilon) \end{aligned} \quad (3.3.26)$$

Recall from Equation (3.1.9), for TE waveguide modes, that the characteristic impedance is

$$Z_0 = \frac{\omega\mu}{\beta} \quad (3.1.9)$$

Substituting this definition for characteristic impedance into the ratio of impedances in Equation (3.3.26) leads to

$$\frac{Z_{\epsilon r1}}{Z_{r1}} = \left( \frac{\omega_{r1}\mu_0}{\beta_{\epsilon r1}} \right) \left( \frac{\beta_{r1}}{\omega_{r1}\mu_0} \right) = \frac{\beta_{r1}}{\beta_{\epsilon r1}} \quad (3.3.27)$$

Using the result of (3.3.27) into (3.3.26) and dividing both sides by  $\ell_\epsilon$  results in

$$-\frac{\tan(\beta_{r1}\ell_0)}{(\beta_{r1}\ell_\epsilon)} = \frac{\tan(\beta_{\epsilon r1}\ell_0)}{(\beta_{\epsilon r1}\ell_\epsilon)} = \hat{k} \quad (3.3.28)$$

The first term in Equation (3.3.28) contains only known and measurable quantities. Recall the definition of  $\beta_{r1}$  from Equation (3.1.14)

$$\beta_{r1} = \sqrt{\epsilon' \left(\frac{\omega_{r1}}{c}\right)^2 - \left(\frac{\pi}{a}\right)^2} = \sqrt{\left(\frac{\omega_{r1}}{c}\right)^2 - \left(\frac{\pi}{a}\right)^2} \quad (3.3.29)$$

where the relative permittivity  $\epsilon' = 1$  in the empty portion of the cavity. Furthermore  $\ell_0$  can be determined very accurately by measuring the resonant frequency of the empty cavity. Remember that

$$\ell_0 = 3d - \ell_\epsilon$$

and

$$d = \lambda_g/2$$

therefore,

$$\ell_0 = 3\lambda_g/2 - \ell_\epsilon$$

Recall from (3.1.10) the definition of  $\lambda_g$  is

$$\lambda_g = \frac{2\pi}{\beta} \quad (3.1.10)$$

It is clear then that by combining Equations (3.3.29), (3.1.10), and (3.1.15) in an empty cavity condition, the empty portion of the specimen loaded cavity is

$$\ell_0 = \frac{3\pi}{\sqrt{\left(\frac{\omega_{r0}}{c}\right)^2 - \left(\frac{\pi}{a}\right)^2}} - \ell_\epsilon \quad (3.3.30)$$

Thus, only the specimen thickness  $\ell_\epsilon$  must be measured accurately by mechanical means; the measured resonant frequency  $\omega_{r0}$  value will then provide a means for determining  $\ell_0$ .

Since the first term in Equation (3.3.28) can be determined from resonant frequency measurements,  $\hat{k}$  becomes a known quantity leading to a transcendental equation of the form

$$\hat{k} = \frac{\tan(\beta_{\epsilon r1} \ell_{\epsilon})}{(\beta_{\epsilon r1} \ell_{\epsilon})} = \frac{\tan \hat{x}}{\hat{x}} \quad (3.3.31)$$

This equation can be solved numerically for the first positive root  $\hat{x}_0$  ; this first root corresponds to the TE<sub>10</sub> mode, while higher-order modes theoretically correspond to larger positive roots. This root ( $\hat{x}_0 = \beta_{\epsilon r1} \ell_{\epsilon}$ ) can be substituted into Equation (3.1.15)

$$\beta_{\epsilon r1} = \sqrt{\epsilon' \left( \frac{\omega_{r1}}{c} \right)^2 - \left( \frac{\pi}{a} \right)^2} \quad (3.1.15)$$

that has been solved for  $\epsilon'$ :

$$\epsilon' = \left( \frac{c}{\omega_{r1}} \right)^2 \left[ \left( \frac{\hat{x}_0}{\ell_{\epsilon}} \right)^2 + \left( \frac{\pi}{a} \right)^2 \right] \quad (3.3.32)$$

With the knowledge of  $\epsilon'$ , the loss factor  $\epsilon''$  in Equation (3.3.25) can be determined.

### 3.4 Q and Resonant Frequency Measurement

A resonant cavity can be modeled by the simple lumped-component circuit shown in Figure 3.4.1 [33]. This model holds for a single resonance mode, therefore a narrow frequency range near the resonant frequency is assumed. The input impedance ( $Z_{in}$ ) as "seen" through the coupling mechanism, a circular iris in this case, can be separated into the external circuit coupling impedance

$$Z_e = R_e + j X_e$$

and the cavity parallel LRC circuit. The coupling resistance  $R_e$  is assumed to be negligible [42]. The input impedance of the parallel circuit can be written:

$$\begin{aligned} Z_{in}'' &= \frac{1}{Y_{in}''} = \frac{1}{\left[ \frac{1}{R} + \frac{1}{j\omega L} + j\omega C \right]} \\ &= \frac{1}{\left[ \frac{1}{R} + j\left( \omega C - \frac{1}{\omega L} \right) \right]} \\ &= \frac{R}{\left[ 1 + j\left( \omega CR - \frac{R}{\omega L} \right) \right]} \end{aligned} \tag{3.4.1}$$

where

$R$  = real resistance of the cavity,

$C$  = capacitance of the cavity,

$L$  = inductance of the cavity,

$\omega$  = circular frequency ,

$j = \sqrt{-1}$

$Y''_{in}$  = input admittance

Multiplying parts of Equation (3.4.1) by an identity of  $(\omega/\omega_0)$ , where  $\omega_0$  is the resonant frequency, yields

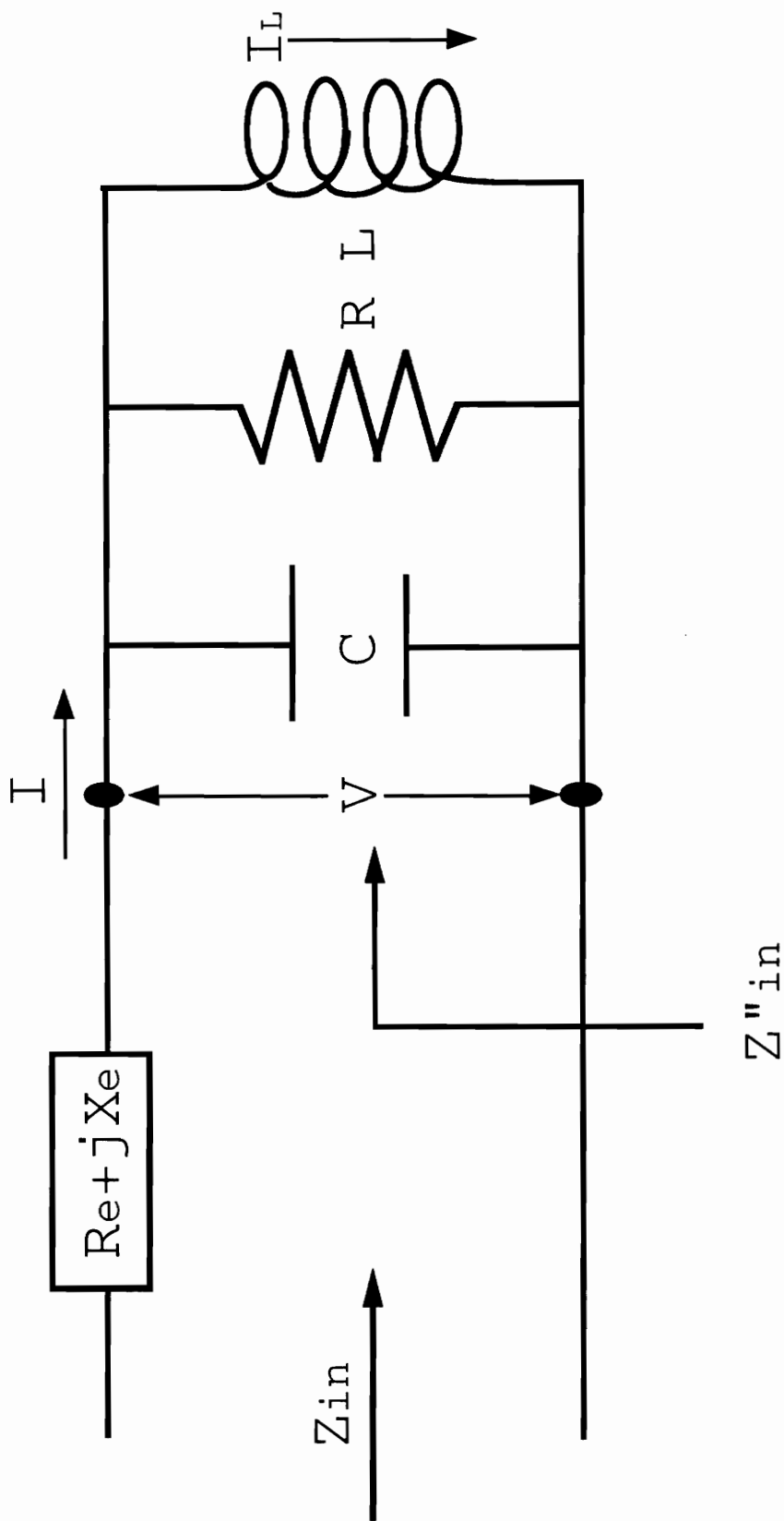


Figure 3.4.1: Lumped-component circuit model for an inductively coupled resonant cavity [33].

$$Z_{in}^* = \frac{R}{1 + j \left[ \frac{\omega}{\omega_0} (\omega_0 CR) - \frac{\omega_0}{\omega} \left( \frac{R}{\omega_0 L} \right) \right]} \quad (3.4.2)$$

Now consider the power input into the cavity ( $P_{in}$ )

$$P_{in} = \frac{1}{2} |I|^2 Z_{in} = \frac{1}{2} |V|^2 \frac{1}{Z_{in}^*}$$

Using  $Z_{in}$  in Equation (3.4.1),

$$P_{in} = \frac{1}{2} |V|^2 \left[ \frac{1}{R} + j \left( \omega C - \frac{1}{\omega L} \right) \right] \quad (3.4.3)$$

The dissipated power ( $P_{loss}$ ), or the real component of the complex power, is written

$$P_{loss} = \frac{1}{2} \frac{|V|^2}{R} \quad (3.4.4)$$

where  $V$  = the voltage across the LRC circuit

$I$  = the total current flowing into the LRC circuit

The average energy capacitively stored in the electric field is

$$U_E = \frac{1}{4} V V^* C = \frac{1}{4} |V|^2 C \quad (3.4.5)$$

and the average magnetic energy stored inductively is

$$U_H = \frac{1}{4} I_L I_L^* L = \frac{1}{4} L \left| \frac{V}{\omega L} \right|^2 = \frac{1}{4} \frac{1}{\omega^2 L} |V|^2 \quad (3.4.6)$$

where  $I_L$  is the complex current flowing through the inductor  $L$  in the model of Figure 3.4.1. Note that the voltage magnitude  $|V|$  in Equations (3.4.4) through (3.4.6) are root mean square (RMS) voltages which are  $(1/\sqrt{2})V_{max}$ , hence the extra factor of 1/2 in Equations (3.4.5) and (3.4.6).

Recall from Equation (3.2.5) that, at resonance,  $U_E = U_H$ . Using this fact and the definition of the "unloaded" or

cavity-only  $Q$  (not including external coupling effects), the result is

$$\begin{aligned}
 Q &= \omega \left( \frac{\text{Average Energy Stored}}{\text{Power Loss}} \right) \\
 &= \omega \frac{U_E + U_H}{P_{\text{loss}}} \\
 &= \frac{2\omega U_H}{P_{\text{loss}}}
 \end{aligned} \tag{3.4.7}$$

Now using the definitions of Equations (3.4.4) and (3.4.6), one obtains

$$Q = \frac{2\omega_0 |V|^2}{4\omega_0^2 L} = \frac{R}{\omega_0 L} \tag{3.4.8}$$

Equating Equations (3.4.5) and (3.4.6) at resonance:

$$\frac{1}{4} |V|^2 C = \frac{1}{4} |V|^2 \frac{1}{\omega_0^2 L} \rightarrow L = \frac{1}{\omega_0^2 C} \tag{3.4.9}$$

Combining Equations (3.4.8) and (3.4.9), the result is

$$Q = \frac{R}{\omega_0 \left( \frac{1}{\omega_0^2 C} \right)} = RC\omega_0 = \frac{R}{\omega_0 L} \tag{3.4.10}$$

These definitions of  $Q$  can be used in Equation (3.4.2), yielding

$$Z_{\text{in}}'' = \frac{R}{1 + jQ \left( \frac{\omega}{\omega_0} - \frac{\omega_0}{\omega} \right)} \tag{3.4.11}$$

The complete input impedance  $Z_{\text{in}}$ , accounting for the impedances of external coupling, the cavity, and any material it contains, is therefore

$$Z_{in} = jX_e + \frac{R}{1 + jQ\left(\frac{\omega}{\omega_0} - \frac{\omega_0}{\omega}\right)} \quad (3.4.12)$$

If the input impedance of Equation(3.4.12) is plotted in the complex plane using frequency as a parameter, a circle is obtained as shown in Figure 3.4.2. Note that at resonance a real component exists corresponding to the physical energy dissipation mechanisms within the cavity. The imaginary reactance component  $X_e$  shifts the circle upward from the real axis. Note in Figure 3.4.2 that the circle does not close symmetrically, rather the plot is a loop with tails at frequencies relatively distant from the resonant frequency. This effect, which has a marked effect upon the determination of  $Q$  from the data, is attributable to  $X_e$  being a linear function of frequency instead of a constant. Hence, the point along the imaginary axis is not strictly  $X_e$ , but is only its constant component  $X_{ec}$  [42].

The input impedance in Equation (3.4.12) is computed from reflection coefficient ( $\Gamma$  discussed in Section (A.4)) data obtained using the network analyzer. Reflection coefficient data obtained when the frequency is swept near resonance results in a loop in the complex  $\Gamma$  plane. The points of this loop can be interpolated and, using a procedure detailed in [42], the information in the  $\Gamma$ -plane can be mapped into the  $Z$ -plane. Note that the external circuit coupling effects are imbedded in the actual  $\Gamma$  measurements and are accounted for in the mapping step. The  $Q$  and  $\omega_0$  of the cavity can subsequently be determined.

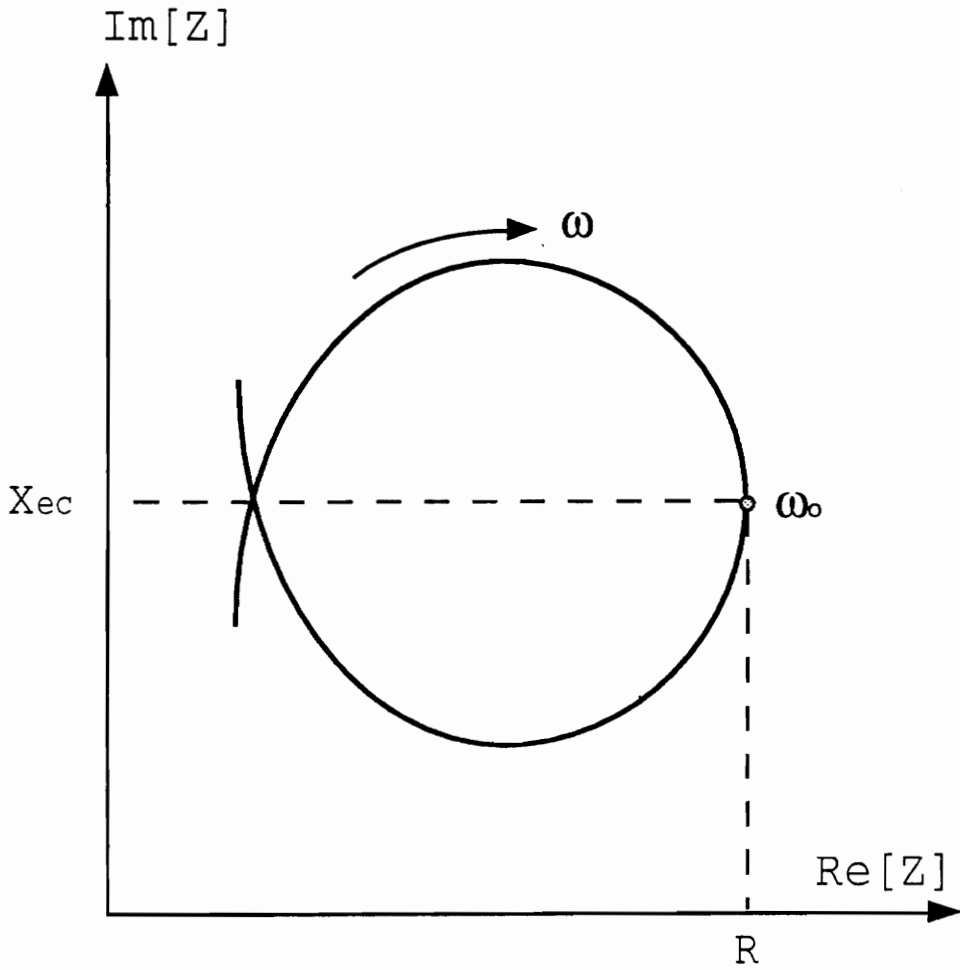


Figure 3.4.2: Input impedance plotted in the complex plane using frequency as a parameter [42].

## 4 EXPERIMENTAL

### 4.1 Equipment

The experimental system used in this study can be subdivided into four categories: 1) the Hewlett-Packard network analyzer system, 2) waveguide cavities and coaxial transmission lines, 3) heat sources and control devices used in elevated temperature measurements, and 4) waveguide calibration standards.

#### 4.1.1 Network Analyzer System

Hewlett-Packard's Model 8510B network analyzer is a microwave receiver that can process signals from a device to determine the phase and amplitude of the waves over a selected frequency band [33,43,44]. As illustrated in Figure 4.1.1, two connection ports on the HP 8515A S-Parameter test unit allow for sampling of incident, reflected, and transmitted signals, often referred to as the S-parameters, related to some device-under-test (DUT). Inside the network analyzer, microwave frequency signals are detected and converted to digital information. An internal computer processes this digital information, computes the phase and amplitude of the S-parameters, and calculates useful quantities including standing-wave ratios (see Section (A.5)) and complex impedances (see Section (3.4)) as a function of frequency.

The computer can also perform error-correction which can mathematically account for slight discontinuities, reflections, losses, and imperfections in the transmission lines leading to the DUT. Error-correction is accomplished by measuring known calibration standards, comparing the signal data to theoretical values in an error model, and mathematically accounting for system imperfections in

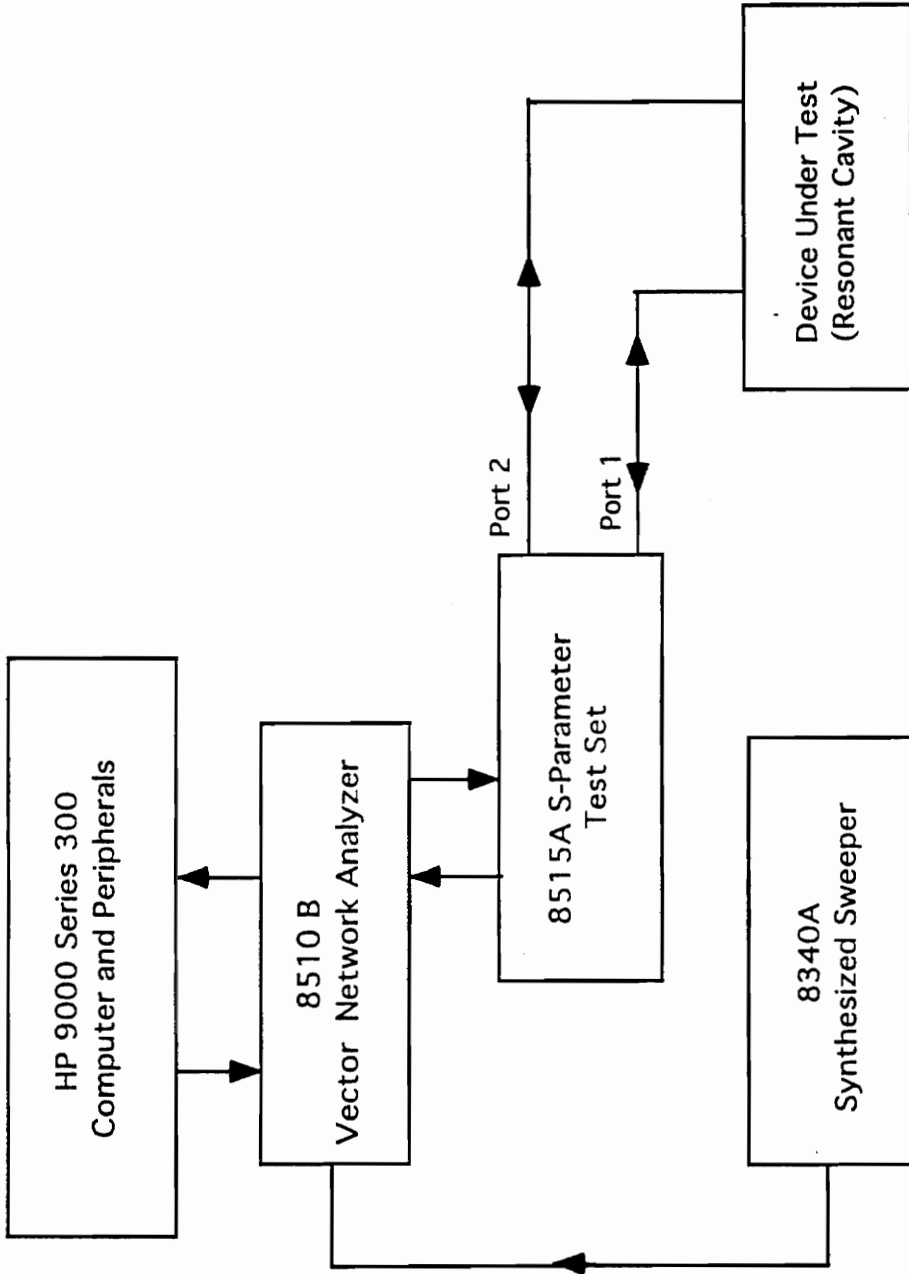


Figure 4.1.1: Schematic of the Hewlett-Packard 8510B network analyzer and 8515A 2-port S-parameter test set system configuration.

subsequent computations. Thus, the calibration procedure is a necessary first step in operating the HP 8510B. There are many calibration procedures; the TRL method used in this study will be outlined in Section (4.2.1).

The 8510B network analyzer can operate in the frequency band from 45 MHz to 26.5 GHz. Thus, the HP 8515A S-parameter test set, which operates in this frequency range, provides the two ports for connecting the network analyzer to the DUT. The source of the high frequency signals in this system is the 8340A synthesized sweeper which has a frequency band of 10 MHz to 26.5 GHz.

The 8510B can be operated from its front panel function buttons and menus; a dial-selector and numerical keypad are also available for input. An HP 9000, series 300 computer is capable of controlling the 8510B and can access the many quantities computed by the network analyzer for analysis in user written programs; such a program was used to determine  $Q$  and  $f_r$  quantities as detailed in Section (3.4).

#### 4.1.2 Coaxial Waveguides and Cavities

Coaxial waveguides serve as the connections from the network analyzer ports to the DUT (a single port cavity in this study). The use of a special, highly flexible coaxial line with APC-7 connectors manufactured by Gore (Model SN S24183) facilitated easy attachment to the cavities in several test configurations. The APC-7 designation stands for "Amphenol Precision Connector," after its original designer, with a 7 mm outer conductor diameter, useful to about 18 GHz. This connector is among the most precise commercial standards in current use [33].

Permittivity measurements were conducted at two frequencies, 2.45 GHz and 9.4 GHz, requiring cavities of different waveguide dimensions. The WR-430 (2.45 GHz) waveguide components that comprised the resonant cavity were

a straight 20.32 cm (8 in.) section and a coax-to-waveguide transition Model APC7-101M section, both manufactured by Struthers Electronic Corporation. The WR-90 (9.4 GHz) waveguide components used to construct the cavity were a straight 6.6 cm (2.6 in.) made in-house at Oak Ridge National Laboratory and a coax-to-waveguide transition Model X209D2 produced by Maury Microwave Corporation. A complete listing of the cavity components are presented in Table 4.1.1. The custom shorting plates were cut from 0.635 cm (0.25 in.) aluminum plate, the inner surface was polished, and the attachment bolt holes were countersunk so the tightened bolt heads would be slightly recessed. This recess was necessary for the short to lie flat on a heating plate in elevated temperature reflection cavity measurements as detailed in Section (4.2.6).

Table 4.1.1  
Cavity Components

Component	Waveguide Designation (Frequency)	
	WR-430 (2.45 GHz)	WR-90 (9.4 GHz)
Straight Section	8" Struthers Electronic Corp.	Custom (ORNL)
Coax-to Waveguide Transition	Struthers Model APC7-101M	Maury Microwave Model X209D2
Iris	1.02" Dia. 0.0056" Thick	0.267" Dia. 0.0056" Thick
Shorting Plate	Custom 1/4" Thick Polished Aluminum	Custom 1/4" Thick Polished Aluminum

#### 4.1.3 Heat Sources

Differences in the configurations of the cavity

perturbation and reflection cavity measurement techniques required different heating schemes in each. As described in Section (4.2.4), hot N<sub>2</sub> gas was used in the cavity perturbation technique. The N<sub>2</sub> gas passed through coils of metal tubing immersed in the sand of a Techne Model SBL-1 fluidized bath heating system, as is illustrated in Figure 4.2.1a. The reflection cavity technique described in Section (4.2.6) used a Corning PC-351 heating plate to heat the composite specimens inside the cavity. This heating plate's power was controlled through a temperature feedback system using an Omega Model 400KC controller fitted with a Type K thermocouple. This heating schematic is shown in Figure 4.2.1b.

#### 4.1.4 Calibration Standards

The 2-port TRL method of calibration used in this study requires only two standards: a short length of waveguide, or line, of known impedance and length, and a highly reflective shorting plate. The initials TRL stand for "Thru-Reflect-Line" which are the three basic steps of the calibration procedure. The "Thru" step requires that the calibration planes of port 1 and port 2 be directly connected, thus no standard is necessary. A polished shorting plate acts as the "Reflect" standard. The shorts used in this study were the custom shorts described in Section (4.1.2). The "Line" standards used in the WR-430 system were a Struthers 6" Model P/N112497 straight section while a Maury microwave Model X103A5 5" standard was used in the WR-90 system. The TRL calibration procedure is outlined in Section (4.2.2).

## 4.2 Procedures

### 4.2.1 TRL Calibration Background

The 2-port TRL, or "Thru-Reflect-Line", technique is a simple yet robust calibration that makes use of transmission

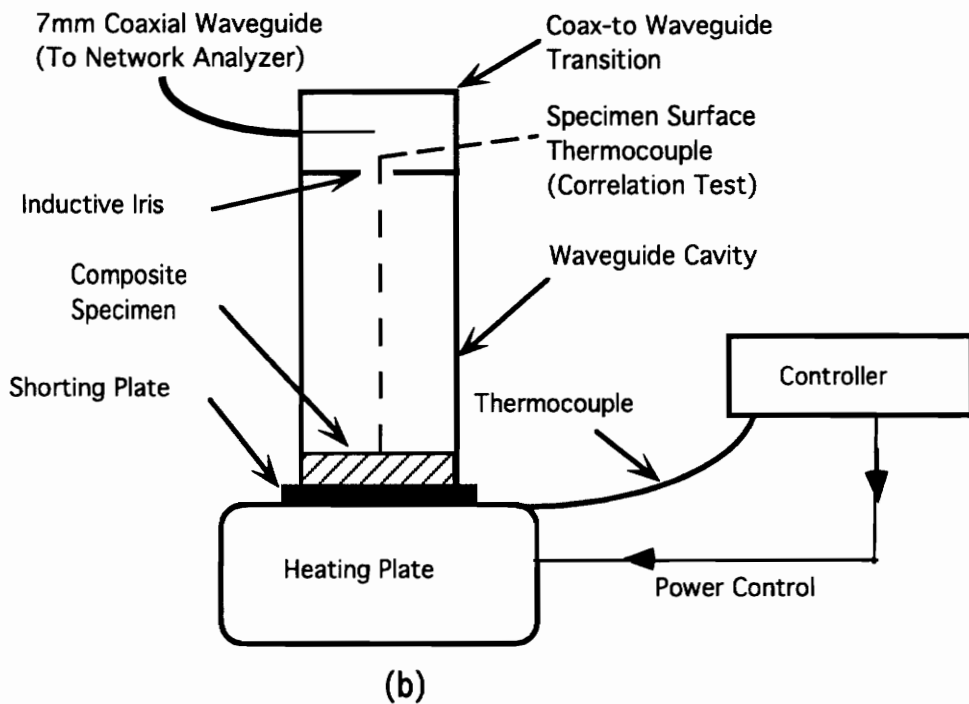
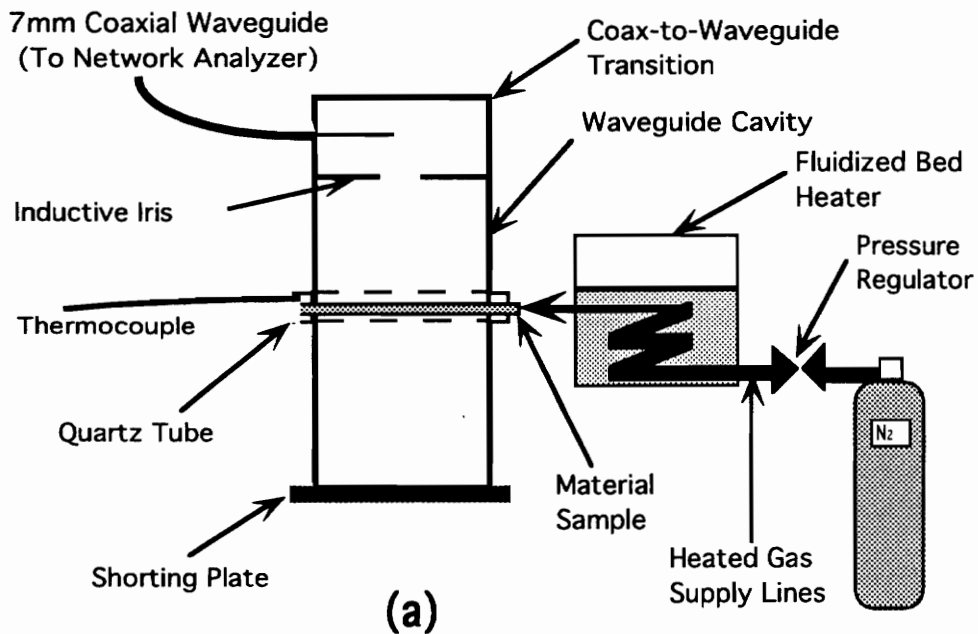


Figure 4.2.1: Apparatus configurations for elevated temperature measurements: (a) hot  $N_2$  gas flow in the cavity perturbation experiment, (b) heating plate and controller in the reflection cavity experiment.

lines instead of special impedance standards [44]. An 8-term error model, described in [44], is built into the HP 8510B network analyzer's computer as an on-line calibration option. Thus, only a section of waveguide of known length and impedance, and a polished short, are needed to perform the calibration.

Several variations on the TRL method are available, as listed in [44]. The zero-length "Thru" option was chosen for simplicity, since no additional waveguide would be necessary. Prior to performing a calibration, the parameters describing the standards to be used must be defined, by the user, in the 8510B's memory. These specified parameters include "Line" length and impedance, the short offset (0 for a flat short), the useful frequency band of the waveguide, and the standard class assignments that are accessed by the TRL program. The procedure for defining standards is somewhat complex and is beyond the scope of this description; detailed information and instructions can be found in [43,44].

#### 4.2.2 TRL Calibration Procedure

A typical TRL calibration procedure would be conducted as follows (note that words in **BOLD** indicate actual labels appearing on the HP8510B buttons and menus):

i) Connect the 7 mm coaxial lines to ports 1 and 2 of the network analyzer and attach coax-to-waveguide transitions to each coax line. The flanged ends of the coax-to-waveguide transitions are the calibration planes.

ii) Press the **PRESET** button on the HP8510B to clear the network analyzer of its current settings and establish a known state. Enter the desired measurement parameters including frequency band, number of data collection points within that band, and data averaging and smoothing functions.

iii) Press the **CAL** button to start the calibration process. Press **TRL 2-PORT** to enter the built-in TRL

calibration model submenu. The titles **THRU**, **S11REFLECT**, **S22REFLECT**, **ISOLATION**, and **LINE** will appear on the submenu. These calibration steps may be performed in any convenient order. Note that **LOWBAND REFLECTION** is used for coaxial system calibrations and therefore will not be used here.

iv) The Thru calibration will be performed first. Connect the coax-to-waveguide transition flanges, clamp them together, and press the **THRU** button. Swept frequency signals from both ports will pass through the system, be detected and digitized by the network analyzer, and stored in the computer's memory. When the frequency band is swept and the measurements are complete, the label **THRU** will be underlined.

v) Disconnect the mated flanges and attach the flat short to the port 1 waveguide flange. Press **S11REFLECT** and allow the frequency sweep to finish. **S11REFLECT** should now be underlined.

vi) Disconnect the short from the port 1 waveguide flange and attach it to the port 2 flange. Press **S22REFLECT** and allow the frequency sweep to finish. **S22REFLECT** should now be underlined.

vii) Disconnect the short from the port 2 waveguide flange and attach the straight waveguide section between the flanges. Press **LINE** and allow the frequency sweep to finish. **LINE** should now be underlined.

viii) The last standard is the **ISOLATION** option. This parameter is used to quantify the systematic cross-talk inside the network analyzer; this is usually very small relative to the power levels used in typical measurements and can be neglected. Press **ISOLATION**, **OMIT ISOLATION**, and **ISOLATION DONE**.

ix) Press **SAVE TRL CAL** and select a **CAL SET** memory location. Error-correction is now in effect over the preset frequency range.

x) Clear the **CAL SET** memory location that numerically immediately follows the set used to store the TRL calibration in step (ix). The program that will be used to measure the  $Q$  and resonant frequency  $f_r$  data uses this memory location; the program will freeze if this memory location is occupied.

#### 4.2.3 Materials and Sample Preparation

The material used in this study was a polycarbonate/unidirectional, continuous fiberglass composite made from a prepregged tape supplied by ICI-Fiberite Corporation. This tape was produced using Makrolon HMS-3118 amorphous thermoplastic polycarbonate resin from Mobay Corporation and Owens Corning S-2 glass fibers. Several 15.24 cm x 15.24 cm (6 in. x 6 in.) plates were fabricated by stacking plies of tape in a mold and consolidating in a heated platen press at a maximum pressure of 1.034 MPa (150 psi) and a maximum temperature of 210°C. All the plies were stacked with fibers aligned in the same direction. A portion of the plates was cut into rectangular specimens with various fiber orientations. Each specimen was precisely machined to the internal dimensions of the rectangular waveguide in which it would be measured. The remainder of the plates was repressed to remove more resin, thereby increasing  $v_f$ . This process was repeated to produce specimens with a range of fiber volume fractions.

Samples of pure S-glass and polycarbonate were prepared for use in the determination of component permittivity. Owens Corning S-2 glass fiber strands were accurately cut to a uniform length, vacuum dried, and weighed. Polycarbonate strands were capillary extruded from Makrolon HMS-3118 bulk material pellets, using a 0.5 mm (0.0204 in.) circular die. The polycarbonate strands were inspected visually to reject any void containing strands from the test specimen lot.

These strands were subsequently vacuum dried, cut to a uniform length, bundled into a volume suitable for measurement, and weighed.

#### 4.2.3 1 Orientation

All tests were conducted with the waveguide propagating the dominant  $TE_{10}$  mode. It can be seen in Figure 3.1.2 that the  $\vec{E}$ -field in this mode has a component only in the direction parallel to the narrow dimension of the cross-plane, which is normal to the axis of the waveguide. Recalling the permittivity mixture theory in Section (2.2.1), composite specimens having fibers aligned with the narrow dimension, and therefore with the  $\vec{E}$ -field, are considered to be in "parallel" geometrically and electrically. Specimens with fibers aligned with the wide dimension are geometrically "perpendicular" or electrically in "series". These orientations are shown schematically in Figure 2.3.1. A range of specimens with orientations  $\theta$  between  $0^\circ$  and  $90^\circ$  was prepared by cutting and machining specimens from the unidirectional panels by rotating the panel at different angles during the cut.

#### 4.2.3.2 Fiber Volume Fraction

Resin burnoff was employed to determine the fiber volume fraction  $v_f$  of each composite specimen plate. Several sample pieces of each plate were placed in dry crucibles, weighed, and heated to  $950^\circ\text{C}$ . The polycarbonate resin burned away at this high temperature leaving only the glass fibers. The crucibles were reweighed and reheated until their weight became constant. The mass fraction of the fiberglass  $m_f$  was determined from the ratio of the final to initial sample weights. The fiber volume fraction  $v_f$  was computed using tabulated densities of polycarbonate  $\rho_{pc}$  and fiberglass  $\rho_f$  as

$$V_f = \frac{\frac{\rho_f m_f}{\rho_{PC}}}{(1 - m_f) + \frac{\rho_f m_f}{\rho_{PC}}} \quad (4.2.1)$$

#### 4.2.4 Cavity Perturbation Technique

The cavity perturbation technique described in Section (3.2) was especially well suited to the measurement of the component S-glass and polycarbonate materials. Specimens of the component materials fit the following criteria for measurement by cavity perturbation:

- 1) low-loss and non-ferromagnetic
- 2) small volumes relative to the cavity volume
- 3) homogeneous and electrically isotropic

Since the component material specimens had the form of strands, they were easily inserted and removed from the cavity through the holes in the broad walls, as illustrated in Figure 3.2.1. The formulae from which  $\epsilon'$  and  $\epsilon''$  are computed, Equations (3.2.25a) and (3.2.25b) respectively, require sample volume as the only material geometry related input parameter. If the material strands are assumed to be uniform along their length, then a volume per unit length ( $V/l_s$ ) quantity can be determined using

$$\frac{V}{l_s} = \frac{m}{l_s} \frac{1}{\rho} \quad (4.2.2)$$

where  $m/l_s$  = mass per unit length of strand  
 $\rho$  = material density

Strands of material were simply cut to a known length and weighed to determine  $m/l_s$ . The densities of the component materials were taken from supplier technical data sheets and the literature [45,46]. The length of the sample strands actually placed inside the rectangular cavity is the narrow dimension  $b$  (see Section (3.3.1)), of the waveguide.

Multiplication of Equation (4.2.1) by  $b$  yields the sample volume  $V_g$  used in Equations (3.2.25a) and (3.2.25b).

Component permittivities were measured at two frequencies, 2.45 GHz and 9.4 GHz, using  $TE_{103}$  rectangular waveguide cavities (see Section (3.2.4)). The designation, dimensions, frequency range, and cutoff frequency of the waveguide used in these cavities are listed in Table 4.2.1 [47].

Table 4.2.1  
Rectangular Waveguide Data

EIA Designation	$TE_{10}$ Mode Frequency Band [GHz]	Cutoff Frequency [GHz]	Physical Dimensions [cm (in.)]			
			Interior		Exterior	
			Width	Height	Width	Height
WR-430	1.72-2.61	1.373	10.922 (4.300)	5.461 (2.150)	11.328 (4.460)	5.867 (2.310)
WR-90	8.20-12.50	6.562	2.286 (0.900)	1.016 (0.400)	2.540 (1.000)	1.270 (0.500)

Permittivities of the component materials were measured as a function of temperature at both frequencies. Hot  $N_2$  gas was flowed through a quartz tube that has been inserted through the sample holes in the waveguide cavity as illustrated in Figure 4.2.1a. A thermocouple was positioned in the outlet end of the quartz tube just outside the waveguide wall; the thermocouple could not protrude into the cavity because its conductive wires would greatly disturb the standing field patterns. The  $N_2$  gas flowed from a pressurized cylinder, through the coils of a fluidized bed heater, then through the quartz tube. The temperature of the gas monitored at the outlet wall of the waveguide was assumed

to be that of the materials being measured. Measurements of  $Q$  factors and resonant frequencies were taken over a temperature range for both the unloaded (empty) and sample loaded conditions (see Section (3.2.3)). It has been assumed that, at the same measured temperature, the unloaded and sample loaded  $Q$  and  $f_r$  data differ only due to the perturbation effects of the sample material; the effects of cavity thermal expansion and quartz tube heating were assumed to be identical in both conditions and therefore cancel in subsequent permittivity computation.

Following preliminary tests, it was determined that the use of a quartz tube extending completely through the cavity was acceptable in the WR-430 cavity, but was unacceptable in the WR-90 cavity. Room temperature measurements of an empty cavity and a teflon sample were made with and without the quartz tube at both frequencies. The data from these tests were used to compute the teflon's permittivity. In the WR-430 case (2.45 GHz), the difference in computed material permittivity between the two conditions (tube present and absent) was very slight; the effect of the tube canceled. This was not the case in the WR-90 (9.4 GHz) test, where the permittivity was found to be significantly higher in both the real and imaginary parts where the quartz tube was present. This implies that the quartz tube may have significantly altered the field patterns in the cavity of smaller volume, leading to a non-linear condition in which tube contributions would not cancel in the process of permittivity computation. Therefore, in subsequent measurements, the  $N_2$  gas was flowed into a section of quartz tube that did not enter the cavity, but acted as a supply hose attachment and material sample holder only. An identical section of quartz tube was placed at the outlet but did not enter the cavity; this section supported the material sample and the thermocouple.

#### 4.2.5 Cavity Perturbation Procedure

The procedure used for measuring the permittivity of the component materials is as follows:

i) Calibrate the network analyzer Port 1 to the plane of the iris using the TRL calibration method (see Section (4.2.2)). This provides a reference of amplitude and phase for the transmission line up to the iris plane, excluding the iris. Save the calibration set in the network analyzer's memory and clear the next calibration set memory space for input from the measurement program.

ii) Place the iris sheet on the calibrated waveguide flange and attach the cavity to the waveguide with bolts, making sure the flanges are exactly aligned. Place the cavity such that the axis of the sample insertion holes is horizontal, i.e., with the waveguide resting upon its length, the narrow dimension vertical.

iii) Run the program "Cavtpert" to collect  $Q$  and  $f_r$  data from the empty cavity condition. The quartz sample tube must be in place for experiments using hot gas flow.

iv) If only a room temperature test is conducted, proceed to step (vii).

v) If elevated temperature measurements are desired, attach the heated  $N_2$  gas line to the inlet of the quartz tube and insert the thermocouple into the outlet end of the tube very near the outer surface of the waveguide wall. Open the valve on the  $N_2$  cylinder regulator to allow a slight gas flow. Monitor the thermocouple signal on the digital thermometer display and adjust the gas flow to obtain the desired temperature. Allow the cavity to come to thermal equilibrium; this will be evident when the changes in  $Q$  and  $f_r$  are small between data measurement intervals. The steady state  $Q$  and  $f_r$  values are to be used in permittivity calculation.

vi) Slightly increase the  $N_2$  flow rate to incrementally raise the temperature. Repeat this incremental  $N_2$  flow rate increase throughout the desired range of temperatures, each time recording the steady state  $Q$  and  $f_r$  values.

vii) Insert the sample material strands. If elevated temperature measurements are desired, make sure that the thermocouple is making good contact with the sample. Allow the entire system to cool to room temperature before reheating.

viii) Repeat steps (iii), (v), and (vi) with the sample strands in place.

ix) Enter the  $Q$  and  $f_r$  data, along with the sample volume, into the program "Perturb" (listed in Appendix B). This program, written in the *Mathematica* language, is based on the derivations in Section (3.2) and will compute the sample's complex permittivity.

The entire series of elevated temperature measurements, both empty and sample loaded, should be conducted under the same calibration conditions to ensure accuracy and repeatability. It should be noted that any disconnection of the transmission lines from the calibration plane back to the network analyzer port invalidates the current calibration; recalibration would be necessary before continuing with measurements.

#### 4.2.6 Reflection Cavity Technique

The permittivity of the rectangular composite specimens was measured using the reflection cavity technique, which was formulated in Section (3.3). The cavity perturbation technique previously described was not suitable for measuring samples with a plate geometry, since observation of orientation effects and assurance of uniform heating would be difficult. A schematic of the reflection cavity

configuration is presented in Figure 3.3.1. Composite permittivities were measured at frequencies of 2.45 GHz (LS-band) and 9.4 GHz (X-band). Dimensions and empty resonant frequencies of these cavities are given in Table (4.2.1).

The formulae from which  $\epsilon'$  and  $\epsilon''$  are computed, Equations (3.3 32) and (3.3 25) respectively, require the composite specimen thickness  $l_{\epsilon}$  as the only material geometry related input parameter. The specimens fit precisely within the waveguide, therefore their planar dimensions were equal to the waveguide inner wall dimensions. Specimen thicknesses  $l_{\epsilon}$  were measured using dial calipers.

Elevated temperature measurements were conducted by placing the reflection cavity in a vertical orientation resting on a flat plate heater as shown in Figure 4.2.1b. It was assumed that the specimens in contact with the shorting plate were uniformly heated. Since the metallic thermocouples could not extend into the cavity during measurements, a thermocouple was placed in the recess of a bolt hole on the external face of the waveguide shorting plate. This external thermocouple monitored temperatures throughout the measurements. A preliminary experiment was conducted where the iris wall of the waveguide cavity was removed, a composite specimen was inserted into its position flat on the shorting plate, and thermocouples monitored the specimen and external measurement point temperatures, as illustrated in Figure 4.2.1b. The specimen monitoring thermocouple was taped to the specimen's surface, and the open end of the cavity was covered to prevent convective air currents from cooling the specimen. The external thermocouple was connected to a feed back controller unit that controlled power flow to the heating plate. Temperature data was collected from both the specimen and external thermocouples over a range of controller temperature settings. These data were plotted to form a correlation

curve, shown in Figure 4.2.2., relating the externally measured temperature to the actual specimen temperature at each controller setting; this curve would serve as a conversion rule for external to specimen temperature during experimental data analysis. Note that there is a small difference (about 1°C) in temperature at low temperatures, increasing to a maximum difference of about 3°C above 130°C.

#### 4.2.7 Experimental Procedure

The procedure used for measuring the permittivity of composite specimens is as follows:

i) Calibrate the network analyzer Port 1 to the plane of the iris using the TRL calibration method (see Section (4.2.2)). This provides a reference of amplitude and phase for the transmission line up to the iris plane, excluding the iris. Save the calibration set in the network analyzer's memory and clear the next calibration set memory space for input from the measurement program.

ii) Place the iris sheet on the calibrated waveguide flange and attach the cavity to the waveguide with bolts, making sure the flanges are exactly aligned. Make sure that the cavity is empty and that the shorting plate is tightly bolted in place with uniform tightening of each bolt to avoid warping. Place the cavity such that the z-axis (the long axis) is vertical, resting on the shorting plate's external face. If elevated temperature measurements are desired, rest the cavity on the heating plate and place the controller thermocouple into the same bolt recess used in the preliminary correlation experiment. Plug the heating plate into the controller supply socket and turn the temperature setting to "high"; this will supply constant heating upon the

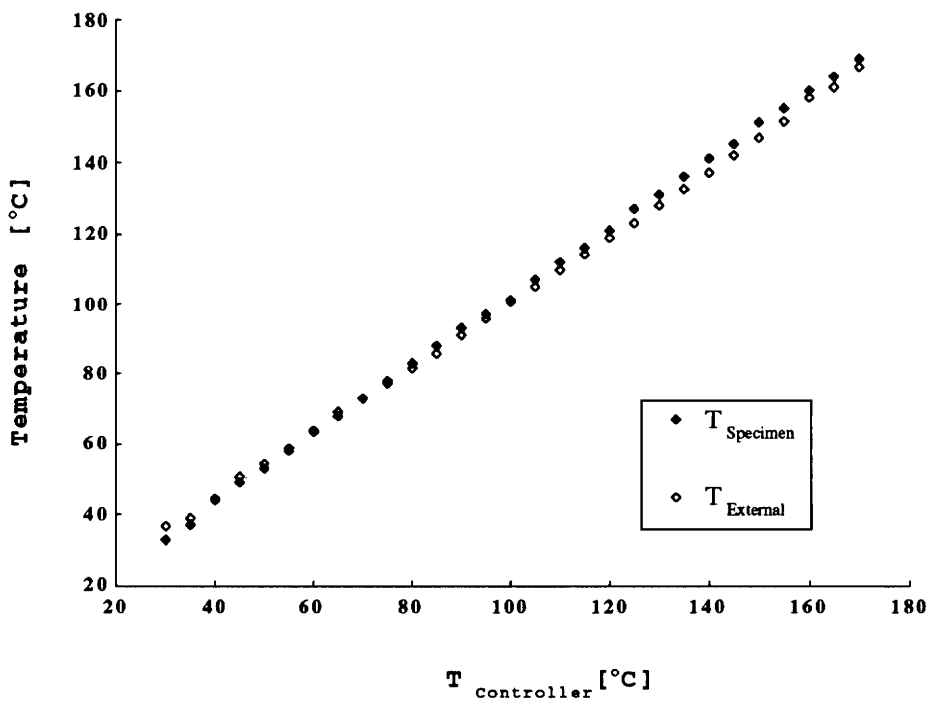


Figure 4.2.2: Temperature correlation curve relating the specimen's surface temperature to the externally measured temperature.

controller's demand, overriding any of the heating plate's control mechanisms.

iii) Run the program "cavtpert" to collect  $Q$  and  $f_r$  data for the empty cavity condition.

iv) If only a room temperature test is conducted, proceed to step (vii).

v) If elevated temperature measurements are desired, increase the controller's set temperature by the desired increment. Most heating experiments conducted in this study used a  $5^\circ$  C increment. Allow the cavity to come to thermal equilibrium and measure the steady state  $Q$  and  $f_r$  values, noting the observed temperature on the resulting computer printout.

vi) Again incrementally increase the controller's set temperature, allow the system to equilibrate, measure  $Q$  and  $f_r$ , and note the observed temperature. Repeat this step throughout the desired temperature range.

vii) Remove the shorting plate, carefully insert the composite specimen into the waveguide, and replace the shorting plate, taking care to tighten the bolts securely and uniformly. If elevated temperature measurements are underway, place the cavity back on the heating plate and replace the control thermocouple. Allow the entire system to cool to room temperature before reheating.

viii) Repeat step (iii) for the material loaded condition. If elevated temperature measurements are desired, repeat steps (v) and (vi) with the composite specimens in place.

ix) Enter the  $Q$  and  $f_r$  data, along with the specimen's thickness, into the program "Reflect" (listed in Appendix B). This program, written in the *Mathematica* language, is based on the derivations in Section (3.3) and will compute the composite specimen's complex permittivity.

## 5 RESULTS

Polycarbonate and S-2 glass permittivities were measured as a function of temperature as described in Section (4.2.5). These component permittivities were substituted into rule-of-mixtures models given by Equations (2.2.7) and (2.2.9) to predict the permittivity of a composite of these materials as a function of fiber volume fraction  $v_f$  at a fixed temperature and as a function of temperature at a fixed  $v_f$ . The permittivity of composite specimens of varied  $v_f$  were measured as a function of temperature as described in Section (4.2.7). This composite permittivity data was compared to the predictions of the mixture models. Composite permittivity as a function of fiber orientation was also measured and was compared to the tensor rotation model of Section (2.3.2).

### 5.1 Component Permittivity Computation

Recall from Section (4.2.4) that the component samples were heated by flowing hot  $N_2$  gas over them and that the temperature was controlled by manually adjusting the gas flow rate. This system, while effective, was difficult to adjust in exact temperature increments, especially at higher temperatures. The average deviation from the desired temperature setpoint, in both the empty and sample loaded tests, was approximately  $0.7^\circ C$ , but maximum deviations from  $2$  to  $3^\circ C$  occurred. For this reason the  $Q$  and  $f_r$  data were not obtained at uniform  $5^\circ C$  increments and were therefore fit with polynomials over the measurement temperature range as shown in Figure 5.1.1 for the 9.4 GHz component material measurements. The  $Q$  factors for the empty cavity and the glass fiber loaded cavity decreased slightly at a nearly constant rate as the temperature increased, while the

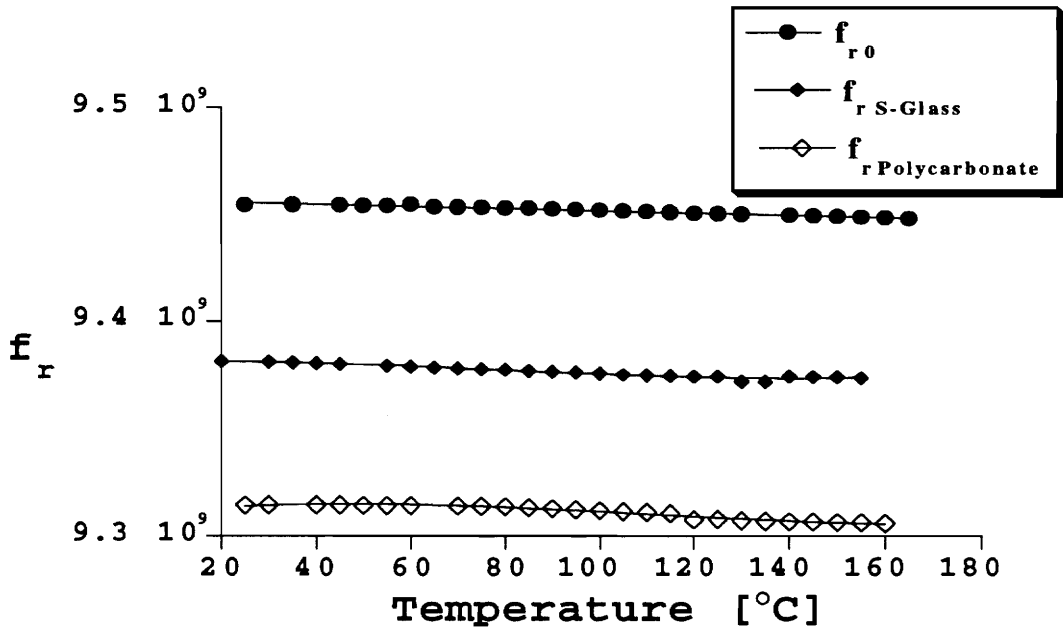
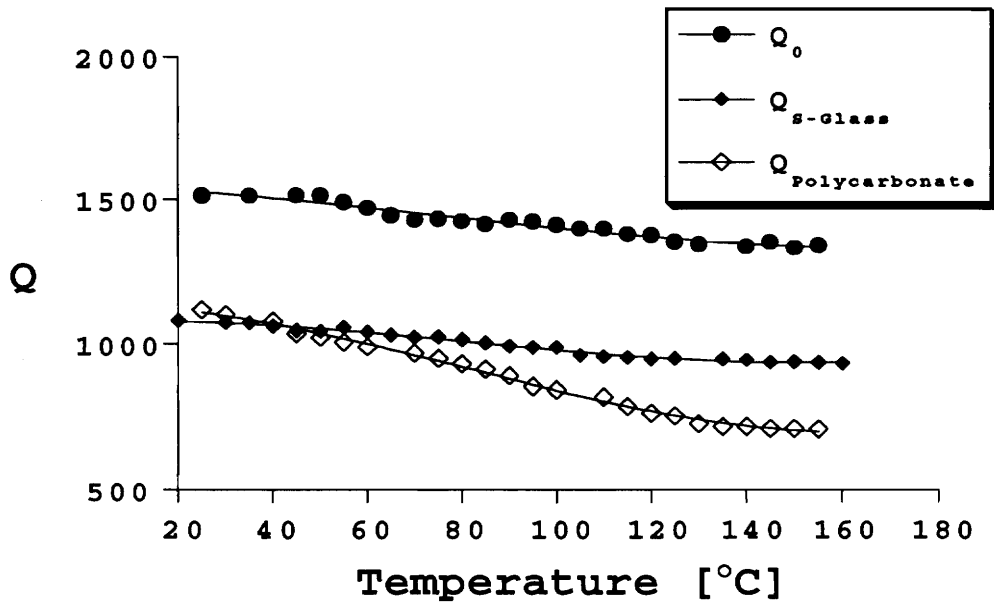


Figure 5.1.1 : 9.4 GHz component material  $Q$  and  $f_r$  data polynomial fit curves.

polycarbonate Q factors decreased at a greater rate for temperatures above 100°C. These data trends were consistent with the slight increases in lossiness of the metal cavity walls and glass fibers with temperature and the strong increase in lossiness of polycarbonate near its glass transition temperature. Resonant frequency  $f_r$  data decreased slightly, in a nearly linear fashion, with temperature for all three cavity conditions; this behavior indicated a minor increase in real permittivity  $\epsilon'$  of the materials with temperature. Each data set was fit with a polynomial that resulted in a least squares correlation coefficient  $R$  of no less than 0.98. These polynomials, presented in Table 5.1.1, were subsequently entered into a modified version of the *Mathematica* analysis program "Perturb" listed in Appendix B. They provided correlation between Q and  $f_r$  for each material at all temperatures in the measured range.

Table 5.1.1  
Component Material Q and  $f_r$  Data Polynomial Fits

Cavity Condition	Q Factor	$f_r$ (Hz)
Empty	$1532.6 + 0.37874 T - 0.032970 T^2 + 0.00018673 T^3$	$9.4577 \times 10^9 - 53277 T$
S-2 Glass	$1126.0 - 1.76130 T + 0.0031447 T^2$	$9.3805 \times 10^9 + 60968 T - 1994.2 T^2 + 8.4199 T^3$
Polycarbonate	$1136.4 - 0.066208 T - 0.049063 T^2 + 0.00020187 T^3$	$9.3095 \times 10^9 + 229370 T - 3059.2 T^2 + 9.1437 T^3$

## 5.2 Results at 9.4 GHz

Permittivities of component materials measured at 9.4 GHz as a function of temperature are shown in Figure 5.2.1. The real part of the permittivity  $\epsilon'$  of both materials changed slightly with temperature from 25°C to 170°C; the S-2

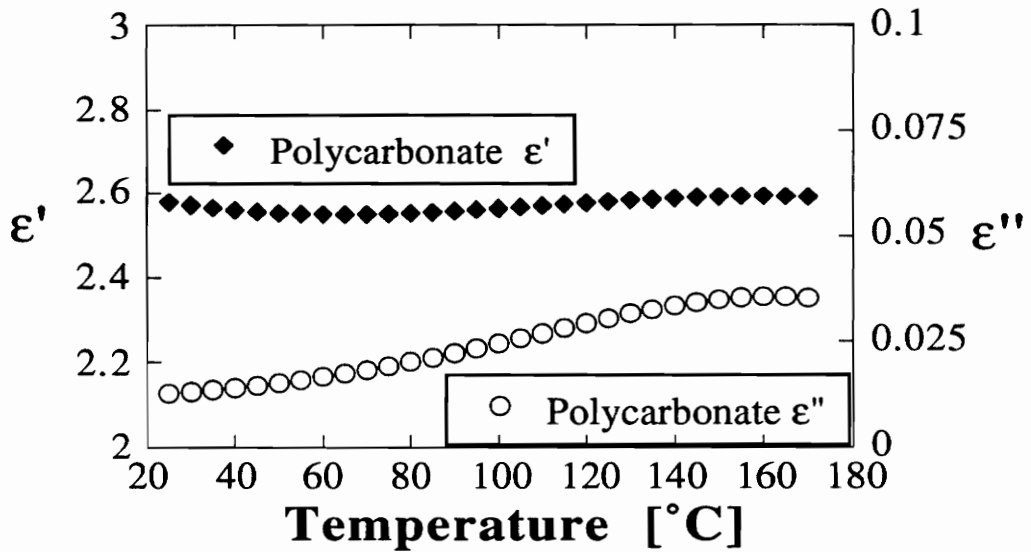
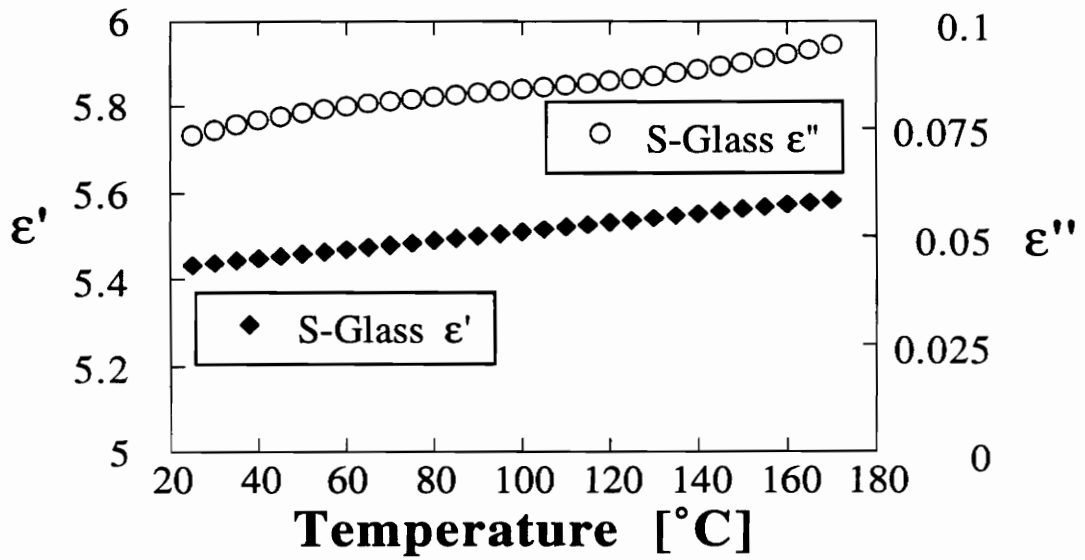
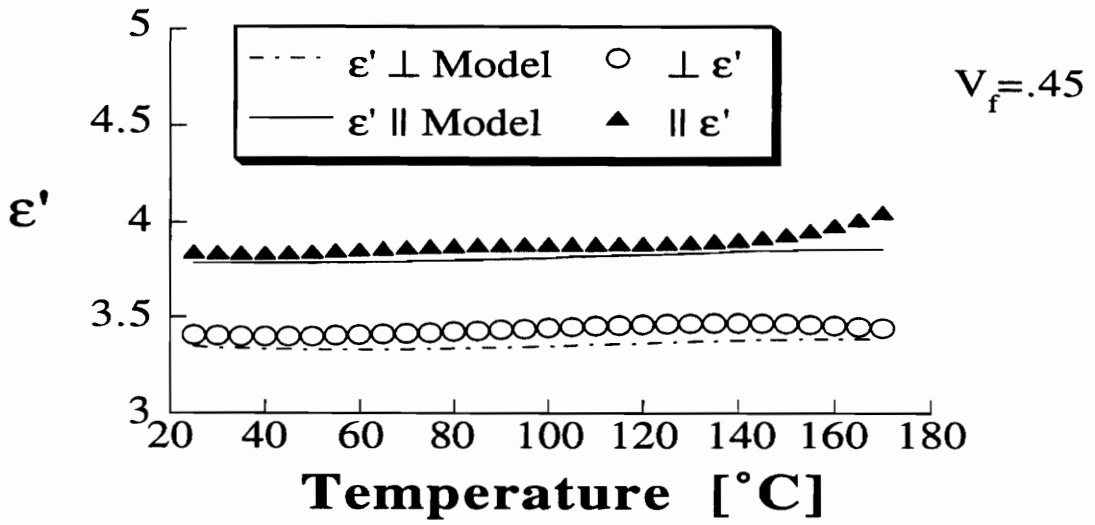


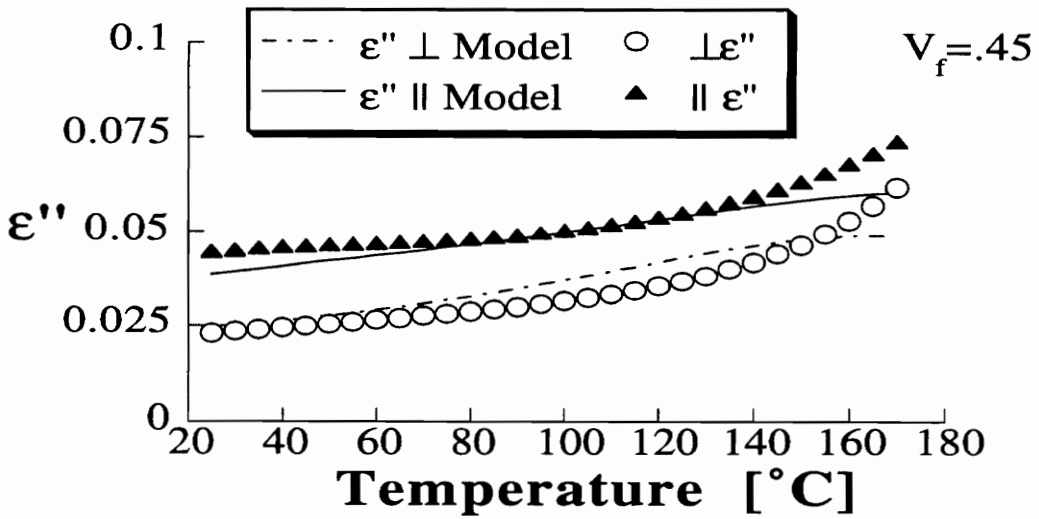
Figure 5.2.1: Component material permittivity measured at 9.4 GHz as a function of temperature.

glass  $\epsilon'$  increased 2.77% and the polycarbonate  $\epsilon'$  increased only 0.46% over this temperature range. The imaginary part of the permittivity  $\epsilon''$  increased significantly for both materials over the same temperature range. The S-2 glass  $\epsilon''$  increased steadily for an overall increase of 28.8% while the polycarbonate  $\epsilon''$  exhibited a relaxation peak starting at roughly 120°C, reaching a maximum in the region of  $T_g$  ( $\approx 150^\circ\text{C}$ ), for a total increase in  $\epsilon''$  of 177%. These results clearly indicate the dielectric relaxation phenomenon occurring in the polycarbonate near its  $T_g$  attributed to the loosening of entanglements and weakening of intermolecular binding forces. These temperatures are too low for the glass fibers to encounter a strong transition region, hence only the moderate increase in  $\epsilon''$ .

The component material permittivities as a function of temperature were substituted into the mixture models given by Equations (2.2.7) and (2.2.9) at a fixed  $v_f = 0.45$  to yield the continuous curves of Figure 5.2.2. The dielectric constants at 9.4 GHz for oriented composite samples show good agreement with the models (Figure 5.2.2a). The loss factors of the composites (Figure 5.2.2b) also agree with the model, although the models do not adequately predict the increased  $\epsilon''$  of the composites near the  $T_g$  of the polycarbonate at 150°C. While it is possible that some unknown physical mechanism caused the composites to deviate from the simple behavior assumed in the rule-of-mixtures models at high temperatures, it is believed that increased measurement error associated with the reflection cavity technique at elevated temperatures contributed to the disagreement in Figure 5.2.2b. A significant source of error might be attributable to the formation of gaps between the composite specimen and the waveguide walls due to the different thermal expansion characteristics of the two materials. This gap can change



a



b

Figure 5.2.2: Model and composite permittivity at 9.4 GHz as a function of temperature.

the field structure assumed in the reflection cavity formulation and can lead to error [39].

Room temperature (23°C) component permittivities were used in Equations (2.2.7) and (2.2.9) to compute the mixture model as a function of fiber volume fraction as shown in Figure 5.2.3. Oriented composite  $\epsilon'$  and  $\epsilon''$  values at 9.4 GHz show very good agreement with the models. With the accurate prediction of  $\epsilon^*(v_f)$ , a simple two-dimensional tensor rotation equation (Section 2.3.2) was used with  $\epsilon^*_{||}$  and  $\epsilon^*_{\perp}$  values considered to be composite permittivities in principal directions parallel and perpendicular to the electric field, respectively. Substitution of composite permittivities at  $v_f = 0.45$  and  $T = 23^\circ\text{C}$  into Equation (2.3.8) yielded the plots in Figure 5.2.4. The measured composite  $\epsilon'(\theta)$  measured values show excellent agreement, while composite  $\epsilon''(\theta)$  data generally follow the model's trend.

### 5.3 Results at 2.45 GHz

A parallel study at 2.45 GHz followed the same computational procedure as that at 9.4 GHz. Component permittivities as a function of temperature are shown in Figure 5.3.1. As in the 9.4 GHz results, dielectric constants  $\epsilon'$  increased slightly, while loss factors  $\epsilon''$  displayed large relative increases with temperature. A comparison of permittivities (Figures 5.2.1 and 5.3.1) shows a slight increase in  $\epsilon'$  magnitude for S-2 glass and little change in polycarbonate  $\epsilon'$  from 2.45 GHz to 9.4 GHz. Much more significant decreases in  $\epsilon''$  magnitudes are evident from 2.45 GHz to 9.4 GHz. This indicates stronger dielectric loss mechanisms at the lower frequency in both the glass and the polycarbonate.

The agreement of elevated temperature composite permittivities at 2.45 GHz with model predictions, shown in Figure 5.3.2, is clearly not as good as results at 9.4 GHz.

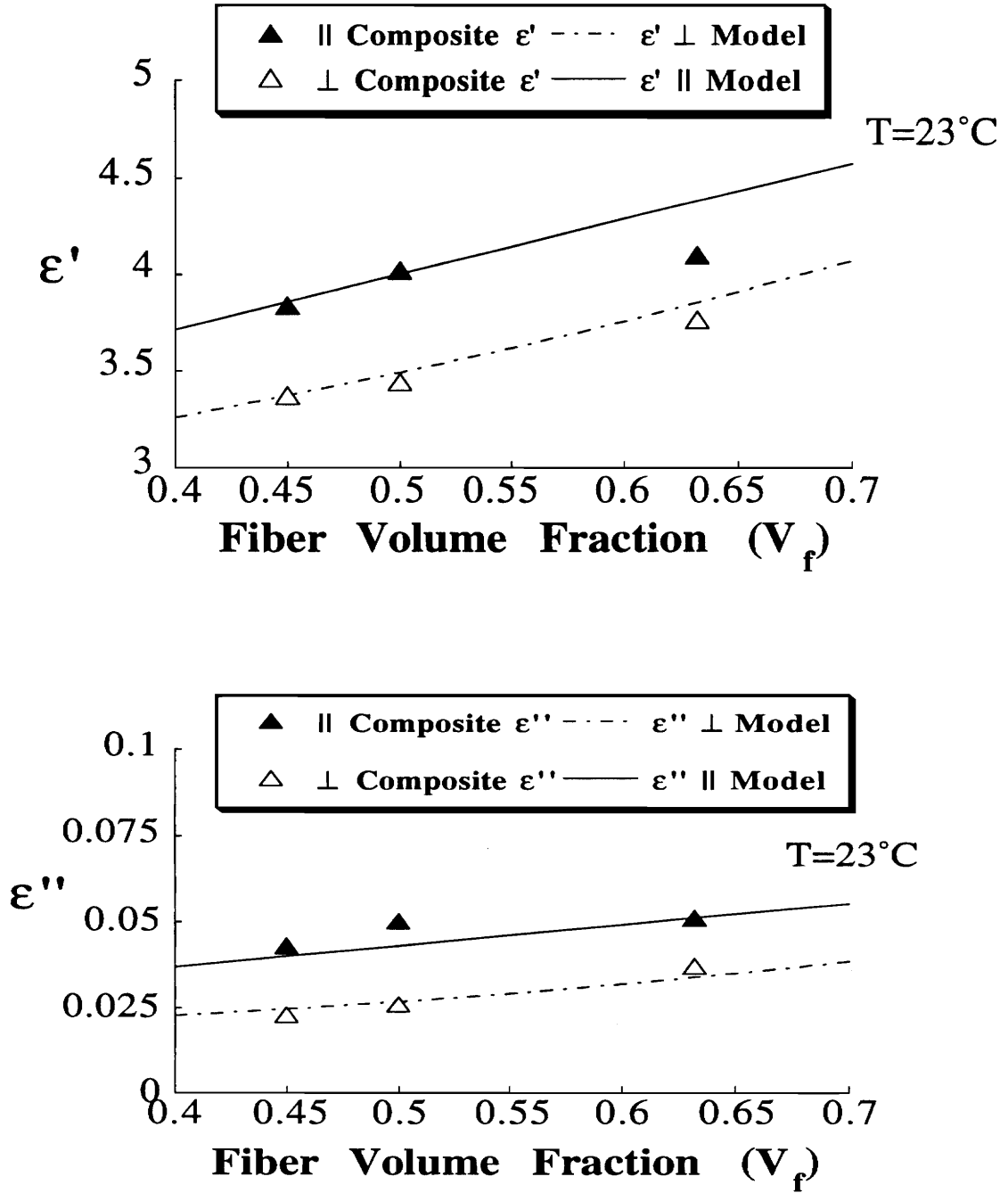


Figure 5.2.3: Model and composite permittivity at 9.4 GHz as a function of fiber volume fraction.

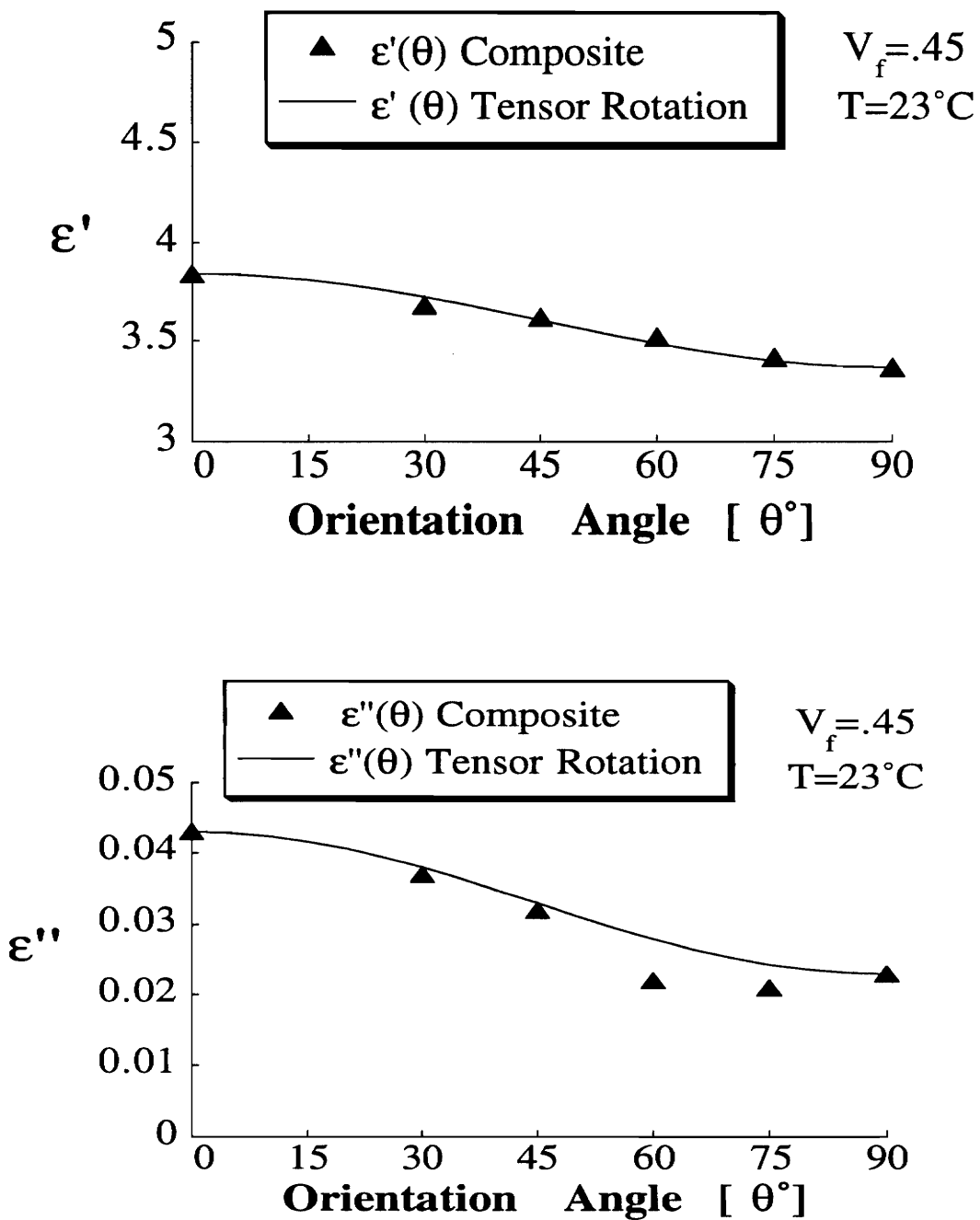


Figure 5.2.4: Model and composite permittivity at 9.4 GHz as a function of fiber orientation.

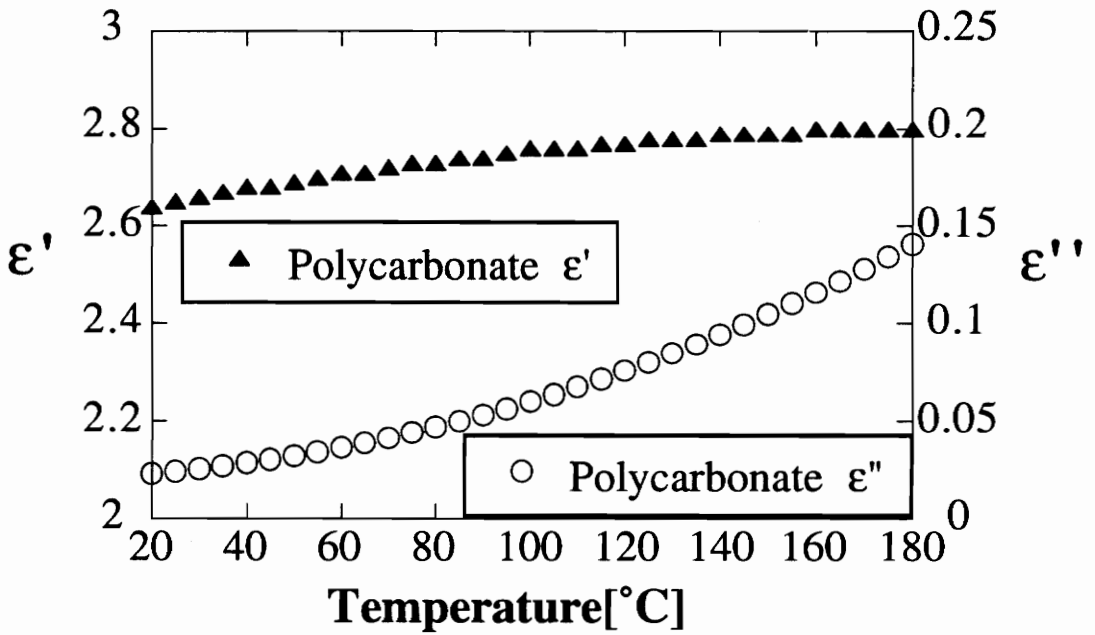
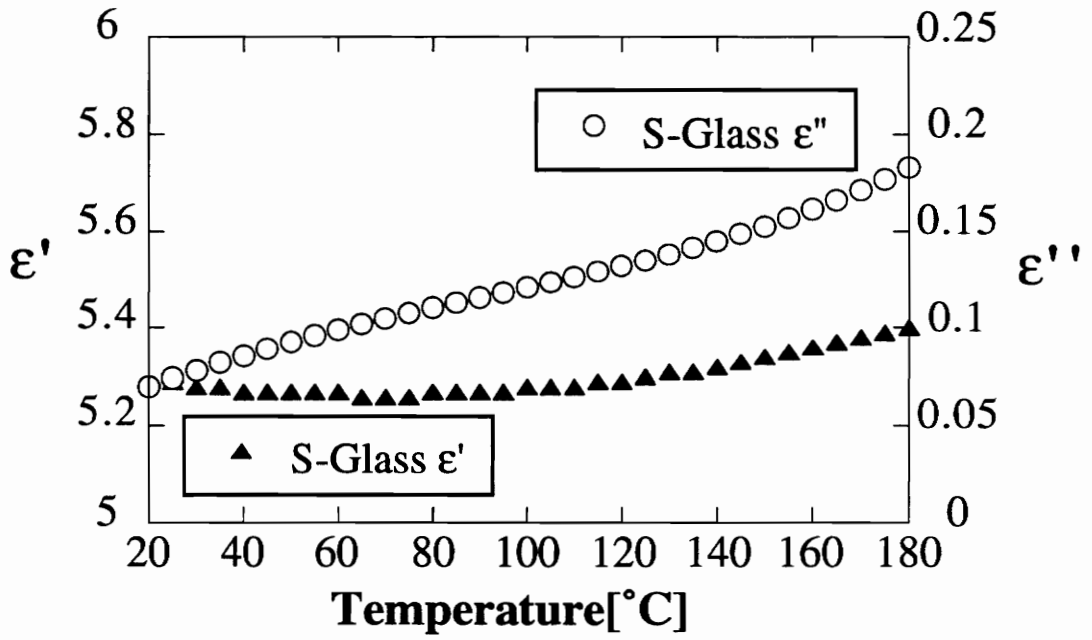


Figure 5.3.1: Component material permittivity at 2.45 GHz as a function of temperature.

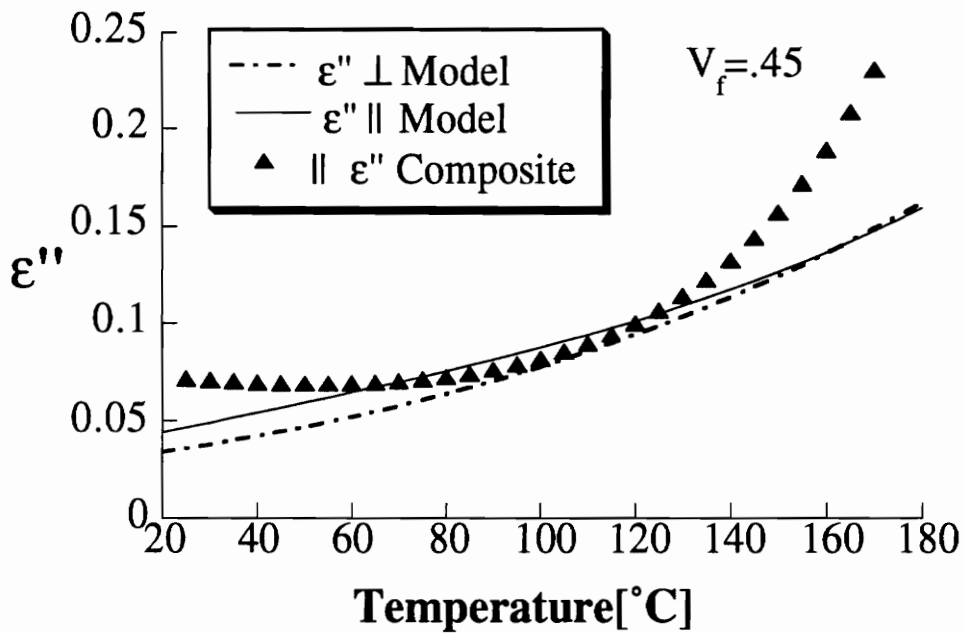
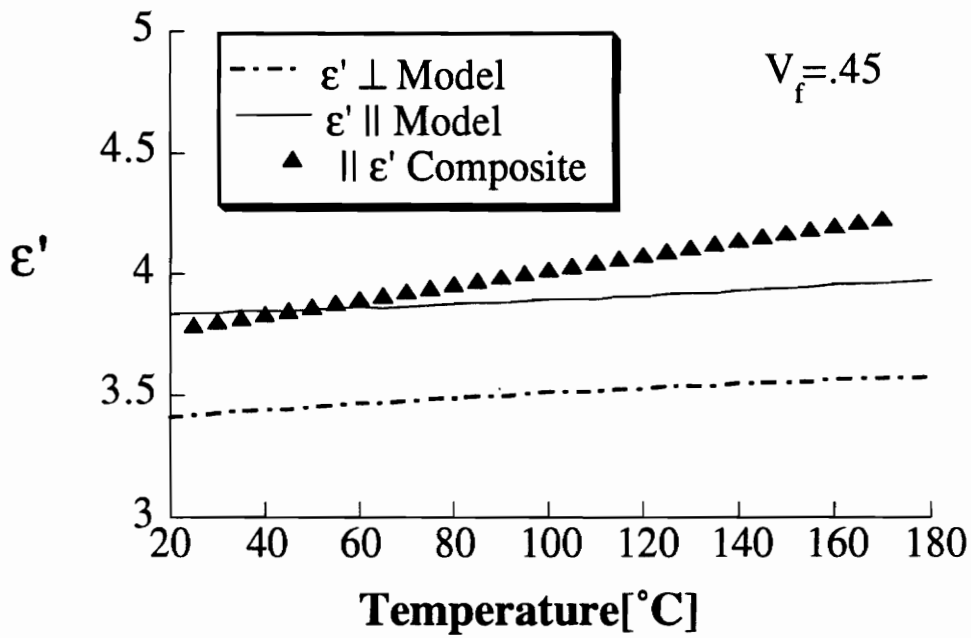


Figure 5.3.2: Model and composite permittivity at 2.45 GHz as a function of temperature.

No results for  $\epsilon^*$  of a composite with perpendicular orientation could be reported with confidence. A comparison of Figures 5.2.3 and 5.3.3 shows a decrease in agreement of the composite  $\epsilon^*(v_f)$  data with the models from 9.4 GHz to 2.45 GHz. While the measurement of the permittivity data points in Figure 5.3.3 was repeatable, it is believed that part of the inaccuracy resulted from using specimens that were thin relative to the measurement wavelength. Specimens with equal fiber volume fraction had the same thickness in both the 2.45 GHz and 9.4 GHz experiments. Since the S-2 glass/polycarbonate prepreg was an experimental system supplied by ICI-Fiberite, only a limited supply was available, and therefore a lack of prepreg stock prevented the fabrication of thicker specimens for the 2.45 GHz study. The composite specimen thickness-to-wavelength ratio was 1:27 at 2.45 GHz, while at 9.4 GHz the ratio was 1:7. The measurement inaccuracy resulting from thin specimens was quantified with measurements at 2.45 GHz made using different thicknesses of teflon ( $\epsilon^* = 2.05 - j 0.0004$ ). Results for a teflon specimen with a thickness-to-wavelength ratio of 1:9, similar to the 9.4 GHz specimens, were  $\epsilon^* = 2.09 - j 0.00021$ , while for a teflon specimen of ratio 1:22, similar to the 2.45 GHz specimens, a permittivity of  $\epsilon^* = 2.38 - j 0.0017$  was obtained. It is clear that for small specimen thickness-to-wavelength ratios the accuracy of the reflection cavity technique declines significantly. In order to attain the thickness-to-wavelength ratio of 1:7 at 2.45 GHz the specimen would need to be approximately 1.5 cm (0.6 in.) thick; a thermoplastic specimen of this thickness would require more prepreg than was available and would be difficult to consolidate with the hot press facilities used in specimen fabrication.

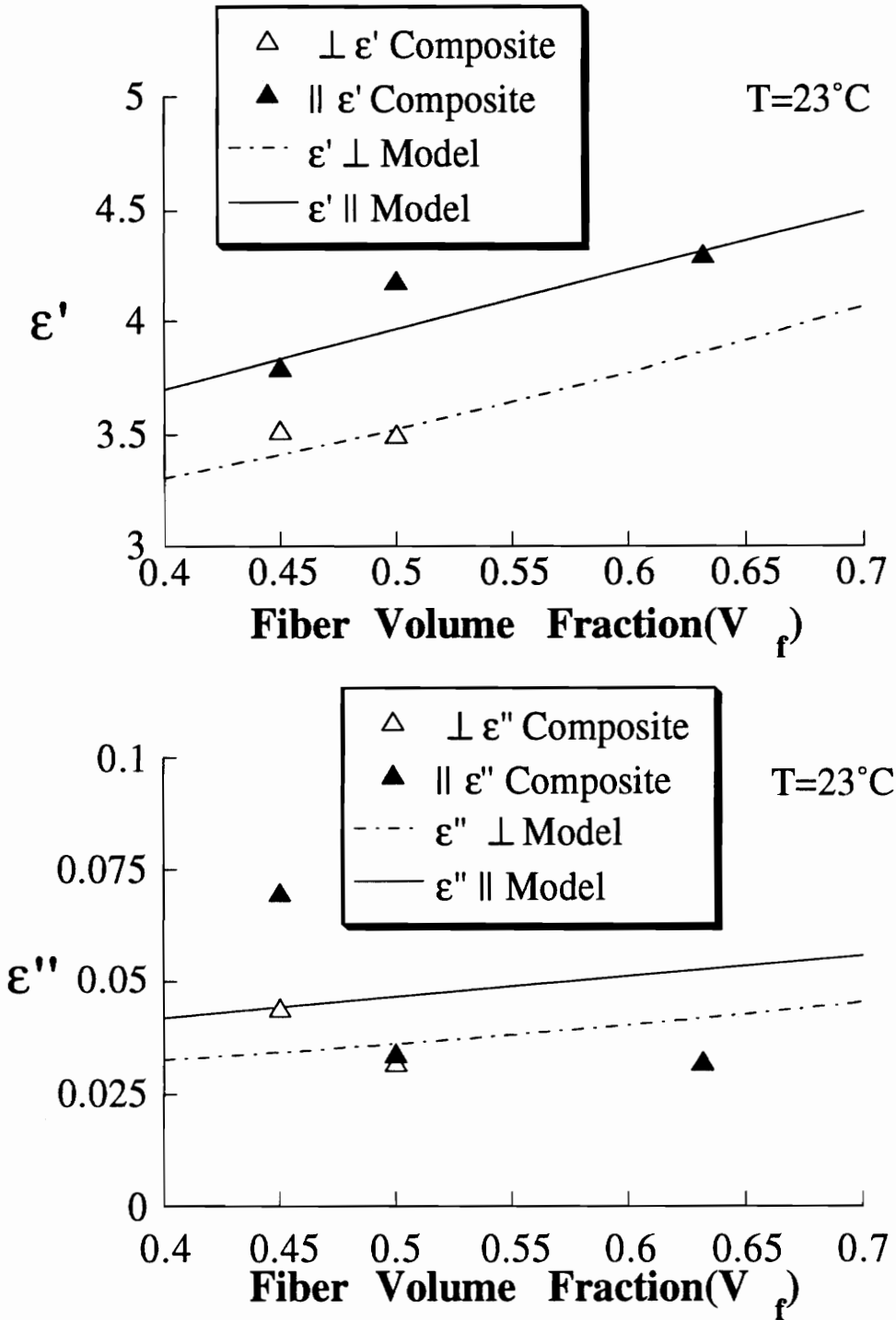


Figure 5.3.3: Model and composite permittivity at 2.45 GHz as a function of fiber volume fraction.

## 5.4 Experimental Uncertainty

The accuracy of the permittivity data was estimated by comparing permittivity measurements of teflon, which is a very low-loss polymer, to values reported in the literature. Teflon is a dielectric commonly used in the manufacture of microwave components and therefore it has been well characterized. MacDonald et. al. reported ranges of permittivity values of  $\epsilon' = 2.01-2.05$  and  $\epsilon'' = 0.0004-0.0006$  for teflon at 10 GHz [5], while Stonier reported  $\epsilon^* = 2.1-j 0.0008$  [3] at 10 GHz and Metaxas and Meredith reported  $\epsilon^* = 2.1-j 0.0003$  [13] at 3 GHz. Note that the cited real parts of the permittivity  $\epsilon'$  vary by a maximum of ~4% while the cited imaginary parts  $\epsilon''$  vary by a maximum of ~150%! It is clear that, for such a low-loss material, only the real part of the permittivity  $\epsilon'$  can be quantitatively compared to reported data; imaginary permittivity  $\epsilon''$  measurements can only be compared on an "order-of-magnitude" basis. Experimental uncertainty for both the reflection cavity and the cavity perturbation techniques at 9.4 GHz will be discussed, while only the cavity perturbation technique uncertainty at 2.45 GHz is presented here; the error in the 2.45 GHz reflection cavity technique is discussed in Section (5.3).

In all experiments to determine uncertainty a teflon sample was measured five times, each time it was removed and replaced before the next measurement. This gave an indication of systematic error, including sample placement. All tests were conducted at room temperature. The reported teflon permittivity of  $\epsilon' = 2.05$  was taken as the standard value [5]. At 2.45 GHz, the cavity perturbation measurements resulted in an average  $\epsilon' = 1.97$  with a standard deviation of 0.007 and a standard error of 0.003 which is 0.16% of the mean. The error in this measurement relative to the standard is -3.9%. The 9.4 GHz cavity perturbation measurements gave an average  $\epsilon' = 2.02$  with a standard deviation of 0.023, a

standard error of 0.010 which is 0.50% of the mean, and an overall relative error of -1.3%. The 9.4 GHz reflection cavity measurements resulted in an average  $\epsilon' = 2.09$  with a standard deviation of 0.024, a standard error of 0.011 which is 0.51% of the mean, and an overall relative error of +2.0%. Systematic errors of  $\pm 5\%$  have been reported in waveguide measurement techniques [5,12], thus the errors determined for the measurement systems in this study seem reasonable.

It is difficult to quantify the accuracy of microwave frequency imaginary permittivity data relative to low-loss standards since few reliable standards exist. Teflon is the notable exception. Most  $\epsilon''$  data reported for polymers and ceramics do not give the exact grade of material. Precise chemical content and material morphology, especially crystallinity, are critical in determining a standard for comparison. Therefore, an "order-of-magnitude" comparison with teflon is an alternative. The previously referenced range of teflon  $\epsilon''$  values was  $3-8 \times 10^{-4}$ . Teflon measurements using the 2.45 GHz cavity perturbation method gave an average  $\epsilon'' = 8.1 \times 10^{-4}$  with a standard deviation of  $2.2 \times 10^{-4}$ , a standard error of  $1.3 \times 10^{-4}$  which is 16% of the mean. The 9.4 GHz cavity perturbation resulted in an average  $\epsilon'' = 2.4 \times 10^{-4}$  with a standard deviation of  $7.4 \times 10^{-5}$ , a standard error of  $3.3 \times 10^{-5}$  which is 13.8% of the mean. The 9.4 GHz reflection cavity method gave an average  $\epsilon'' = 2.1 \times 10^{-4}$  with a standard deviation of  $2.1 \times 10^{-4}$ , a standard error of  $9.4 \times 10^{-5}$  which is 44% of the mean. Since the component and composite materials measured in this study have  $\epsilon''$  values approximately 2 orders of magnitude higher than that of teflon, the sensitivity and accuracy demonstrated in the measurement of the teflon leads to the conclusion that the reported  $\epsilon''$  values are reasonably accurate.

The network analyzer/cavity system, independent of the material measurements, proved to be very accurate. When an

empty, calibrated cavity was repeatedly measured, i.e., the permittivity of air ( $\epsilon^*=1-j0$ ) was determined,  $\epsilon'$  and  $\epsilon''$  fluctuated from the exact permittivity on the order of  $10^{-5}$  and  $10^{-6}$ , respectively. It is therefore believed that systematic error was slight and that the primary sources of uncertainty were attributable to improper orientation and/or fit of samples, errors in measuring sample dimensions, uncertainty in temperature measurement, and uncertainty arising from the assumptions made in the cavity perturbation and reflection cavity analyses for determining  $\epsilon^*$ .

## 6 CONCLUSIONS

### 6.1 Conclusions

The microwave frequency complex permittivity of unidirectional-fiber reinforced thermoplastic composites has been measured and modeled. A cavity perturbation technique was used to measure the component material permittivity as a function of temperature. Composites of these components were fabricated and a reflection cavity technique was used to measure the composite permittivities as a function of temperature, fiber volume fraction, and fiber orientation relative to a unidirectional electric field. Rule-of-mixtures and tensor rotation models, using permittivity data from the component material experiments, were used to predict the composite permittivities; the model predictions and experimental data were compared. As a result of this work the following conclusions have been drawn:

1) Based upon comparisons within the S-2 glass/polycarbonate material system, it appears that the simple "rule-of-mixtures" models can be used to predict the permittivities of unidirectional-fiber reinforced thermoplastic composite materials as a function of fiber volume fraction ( $v_f$ ) and orientation ( $\theta$ ) relative to the electric field based upon known component permittivities. Given the component material permittivity characterized with temperature ( $\epsilon^*(T)$ ), these models can predict elevated temperature composite permittivities. While some deviation from the simple mixture models occurred at temperatures above the  $T_g$  of the polymer, this deviation may have been to the measurement uncertainty of the experimental apparatus at high temperatures.

2) Appropriate mixture models provide accurate prediction of composite permittivities and eliminate the need for difficult microwave frequency composite permittivity

measurements. Furthermore, the accuracy in predicting lower microwave frequency (hence longer wavelength) composite permittivities is improved since thin composite samples cannot be measured as accurately using the reflection cavity technique as can the component materials using cavity perturbation methods.

3) Mixture models are only as useful as the input component material permittivities are accurate. This fact is especially important in low-loss mixtures where  $\epsilon''$  may be difficult to measure with a high degree of certainty. Though little accurate microwave frequency complex permittivity data for low-loss standard materials is available, teflon is one notable exception. This study employed teflon as the standard material for determining systematic error. Due to the extreme low-loss nature of teflon, however, only an order-of-magnitude error analysis for  $\epsilon''$  was possible; this error analysis seems reasonable since the component materials used in this study were approximately two orders of magnitude larger in  $\epsilon''$ .

4) The success of the rule-of-mixtures models indicates that, for the S-2 glass/polycarbonate material system, composites behave like the assumed simple layered dielectric oriented relative to the electric field. The complex permittivity of a composite with its fibers oriented parallel ( $\epsilon_{||}^*$ ) to the electric field is analogous to parallel oriented two-phase capacitor dielectrics where the capacitances are additive, or in series. The complex permittivity of a composite with its fibers oriented perpendicular ( $\epsilon_{\perp}^*$ ) to the electric field is analogous to a perpendicularly oriented two-phase capacitor dielectric where the capacitances are electrically added in parallel.

Some well known averaged-field effective-mixture models, including the Sillars model and the Bottcher model, agree with the parallel rule-of-mixtures models in the limit of

large aspect ratio unidirectional fibers in a single matrix, but do not agree in the perpendicular orientation case where the rule-of-mixtures model predicts a lower bound. The rule-of-mixtures lower bound was verified by the experimental data. The perpendicular-oriented effective mixture models assume that the fiber is an oriented spheroid of large aspect ratio. The depolarization factor for this spheroid describes the effect of the fiber's geometry on the difference between the externally applied electric fields and the electric field inside the spheroid. This depolarization factor is the only means of designating the orientation of the spheroidal fiber's major axes relative to the electric field. Since the averaged-field effective mixture model does not lead to the same result as the experimentally verified perpendicular rule-of-mixtures model, it is concluded that, due to the limitations of the depolarization factor, the spheroidal fiber assumption fails for the case of perpendicular orientation in a high aspect ratio unidirectional continuous-fiber composite permittivity mixture model.

5) Although several microwave frequency permittivity measurement techniques exist [39], each has specific limitations and variable degrees of accuracy, therefore care must be taken when choosing a technique. The cavity perturbation technique used in this study is very accurate for low-loss dielectrics, the sample volume is the only required material specific input, and the raw data can be analyzed using simple closed-form equations. The restriction of sample geometry to uniform cross-section rods is the main limitation to the cavity perturbation technique.

The reflection cavity technique is well suited to the permittivity measurement of anisotropic materials since only a single electric field component exists in a rectangular cavity resonating in the  $TE_{10}$  mode. Several drawbacks to the reflection cavity technique include: material samples must be

precisely machined to prevent air gaps at the waveguide walls, the shorting plate must be removed to insert samples possibly leading to increased error, only flat plates of material can be used, and the raw data analysis for  $\epsilon^*$  involves the solution of transcendental equations that are very sensitive to variations in input parameters. Another potential problem with the reflection cavity technique arises when samples are used that are small relative to the guide wavelength. Since the electric field vanishes at the conductive surface of the shorting plate, a thin sample would interact little with the fields, resulting in increased error. Theoretically, the closer a sample's thickness to one-quarter of the guide wavelength, the better the results. Microwave frequency permittivity measurements at elevated temperatures are difficult and are inaccurate relative to room temperature measurements; this problem is the subject of ongoing study elsewhere [11,12].

## **6.2 Recommendations for Future Work**

The ultimate utility of a composite permittivity model will require the accurate prediction of permittivity for laminates of different matrix and fiber types, varied ply orientations, and varied fiber volume fractions. These demands lead to the following recommendations for further study:

- 1) An amorphous thermoplastic matrix was used in this study for simplicity. The degree of crystallinity in thermoplastics that crystallize has a significant effect on permittivity since the polymer chains are frozen into more ordered conformations in crystals relative to the amorphous state. Similarly, the permittivity of thermoset polymers change dramatically as they undergo cure. Semicrystalline thermoplastics and thermoset resins will require an additional model describing permittivity as a function of the

degree of crystallinity and degree of cure, respectively, in order to extend the permittivity mixture models to these materials.

2) Aramid and carbon fibers are commonly used in polymer matrix composites. Aramid fibers are relatively low-loss and would likely obey the mixture models of this study. Carbon fibers are very conductive and would probably dominate the permittivity characteristics of the mixture at any useful fiber volume fractions. One interesting avenue of study may involve hybrid combinations of carbon and low-loss fibers used in composites to tailor the electrical properties of the material.

3) The rotated permittivity tensor model is directly applicable to modeling laminates composed of plies in various orientations. Electromagnetic propagation, absorption, and reflection characteristics of each ply can be determined from the permittivity tensor and ply geometry. These electromagnetic parameters can be combined to model the laminate's response to microwave radiation in both processing and radar-avoidance applications. The laminate permittivity model could be verified using techniques similar to the reflection cavity technique employed in this study.

4) Component and composite permittivity measurements could be determined more accurately by more precise control of the specimen dimensions. Solid rods of homogeneous component material with a constant diameter and composite specimens machined to exact waveguide dimensions would reduce error. This precision machining might add expense, however. The problem of elevated temperature permittivity measurement might be solved by using free-space cavity methods such as the Fabry-Perot cavity [5,6]. This method uses parabolic reflectors to set up a resonance condition in free-space, thus the material does not contact the "cavity" surfaces, eliminating the thermal expansion problem. This method is

currently under investigation for use in microwave frequency permittivity measurements.

## REFERENCES

- [1] Mijovic, J., and Wijaya, J., "Review of Cure of Polymers and Composites by Microwave Energy," *Polymer Composites*, 11 (3), 184-191 (1990).
- [2] Drzal, L.T., Hook, K.J., Agrawal R.K., "Enhanced Chemical Bonding at the Fiber-Matrix Interphase in Microwave Processed Composites," in Microwave Processing of Materials II, edited by W.B. Snyder, W.H. Sutton, M.F. Iskander, and D.L. Johnson, Materials Research Society Symposium Proceedings, Vol. 189, 449-454 (1991).
- [3] Stonier, A.R., "Stealth Aircraft & Technology from World War II to the Gulf: Part 1 History and Background," *SAMPE Journal* , 27 (4), 9-17 (1991).
- [4] Stonier, A.R., "Stealth Aircraft & Technology from World War II to the Gulf: Part 2 Applications and Design," *SAMPE Journal* , 27 (5), 9-18 (1991).
- [5] MacDonald, A., Moore, R.L., Neale, D., "Characterization of Electromagnetic Material," Technical Report No. RL-TR-92-59, RADC/EECT, Hanscomb AFB, 1992.
- [6] Moore, R.L., MacDonald, A., Moroz, H.R., "Permittivity of Fiber-Polymer Composites: A Study to Determine the Effects of the Environment," *Microwave Journal* , 34 (2), 67-82 (1991).
- [7] Webman, I., Jortner, J., and Cohen, M.H., "Theory of Optical and Microwave Properties of Microscopically Inhomogeneous Materials," *Physical Review B*, 15 (12), 5712-5723 (1976).

- [8] Lee, W.I. and Springer, G.S., "Interaction of Electromagnetic Radiation with Organic Matrix Composites," *Journal of Composite Materials*, 18, 357-385 (1984).
- [9] Lee, W.I. and Springer, G.S., "Microwave Curing of Composites," *Journal of Composite Materials*, 18, 387-409 (1984).
- [10] Aussudre, S., Priou, A., Jullien, H., Delmotte, M., Thullier, F.M., Boulonnais, D., Sailleau, J., "Use of Electromagnetic Waves in the Fabrication of Composite Materials," *Rech. Aerosp.*, 5, 1-13 (1988).
- [11] Tinga, W.R., "Rapid High Temperature Measurement of Microwave Dielectric Properties," in Microwave Processing of Materials III, edited by W.B. Snyder, W.H. Sutton, M. Iskander, and D.L. Johnson, Material Research Society Proceedings, Vol. 269, (1992).
- [12] Salsman, J.B., "Technique for Measuring the Dielectric Properties of Minerals as a Function of Temperature and Density at Microwave Heating Frequencies," in Microwave Processing of Materials II, edited by W.B. Snyder, W.H. Sutton, M. Iskander, and D.L. Johnson, Material Research Society Proceedings, Vol. 189, (1990).
- [13] Metaxas, A.C., and Meredith, R.J., Industrial Microwave Heating, Peter Peregrinus Ltd., London, (1983).
- [14] Kingery, W.D., Bowen, H.K., and Uhlmann, D.R., Introduction to Ceramics, John Wiley & Sons, New York, 931-945 (1976).

- [15] Chen, M., Electromagnetic Radiation Calorimetry of Thermoplastics, Elastomers, and Composite Systems, Ph.D. Dissertation, VPI & SU, (1989).
- [16] Jabbari, E., Investigation of the Heating and Curing Rate of Polymeric Materials with Thermal Energy, Continuous and Pulsed Microwave Radiation, M.S. Thesis, VPI & SU, (1989).
- [17] Bur, A.J., "Dielectric Properties of Polymers at Microwave Frequencies: A Review," *Polymer*, 26, 963-977 (1985).
- [18] Debye, P., Polar Molecules, Chemical Catalog Co., New York (1929).
- [19] Cole, K.S., and Cole, R.H., *Journal of Chemical Physics*, 9, 341 (1941).
- [20] Havriliak S., and Negami, S., "A Complex Plane Analysis of  $\alpha$ -Dispersions in Some Polymer Systems," *Journal of Polymer Science: Part C*, 14, 99-117 (1966).
- [21] Hayt, W.H. Jr, Engineering Electromagnetics, McGraw-Hill, New York, Fourth ed., (1981).
- [22] Banhegyi, G., "Comparison of Electrical Mixture Rules for Composites," *Colloid and Polymer Science*, 264, 1030-1050 (1986).
- [23] Polder, D., and van Santen, J.H., "The Effective Permeability of Mixtures of Solids," *Physica*, 12, 257-271 (1946).
- [24] Stratton, J.A., Electromagnetic Theory, McGraw-Hill, New York, 206-207 (1941).

- [25] Perrin, J., Despax, B., Kay, E., "Optical Properties and Microstructure of Gold-Fluorocarbon Polymer Composite Film," *Physical Review B*, 32 (2), 719-732 (1985).
- [26] Sillars, R.W., "The Properties of a Dielectric Containing Semi-conducting Particles of Various Shapes," *Journal of the Institute of Electrical Engineers*, 80: 378-394 (1937).
- [27] Hsu W.Y., Gierke, T.D., Molnar, C.J., "Morphological Effects on the Physical Properties of Polymer Composites," *Macromolecules*, 16, 1945-1947 (1983).
- [28] Lal, K., and Parshad, R., "The Permittivity of Heterogeneous Mixtures," *Journal of Physics D*, 6, 1363-1368 (1973).
- [29] Bilboul, R.R., "A Note on the Permittivity of a Double-Layer Ellipsoid," *Journal of Physics D*, 2, 921-923 (1969).
- [30] Tinga, W.R., Voss, W.A.G., and Blossey, D.F., "Generalized Approach to Multiphase Dielectric Mixture Theory," *Journal of Applied Physics*, 44 (9), 3897-3902 (1973).
- [31] Sheng, P., "Pair-cluster Theory for the Dielectric Constant of Composite Media," *Physical Review B*, 22 (12), 6364-6368 (1980).
- [32] van Beek, L.H.K., "Dielectric Behavior of Heterogeneous Systems," in Progress in Dielectrics Vol. 7, edited by J.B. Birks, CRC Press, Cleveland OH, 71-114 (1967).

- [33] Pozar, D.M., Microwave Engineering, Addison-Wesley Publishing, New York, (1990).
- [34] Jones, R.M., Mechanics of Composite Materials, Hemisphere Publishing, New York, 325-326 (1975).
- [35] Von Hippel, A.R., Dielectrics and Waves, John Wiley and Sons, New York, (1954).
- [36] Frosini, V., Butta, E., Calamia, M., *Journal of Applied Polymer Science*, 11, 527-551 (1967).
- [37] Vail, C.R., Electro-Technology Science and Engineering Series, No. 38, 82-98 (1962).
- [38] Satomura, Y., Matsuhara, M., and Kumagai, N., "Analysis of Electromagnetic-Wave Modes in Anisotropic Slab Waveguide," *IEEE Transactions on Microwave Theory and Techniques*, 22 (2), 86-92 (1974).
- [39] Altschuler, H.M., "Dielectric Measurements," in Handbook of Microwave Measurements 3rd ed., edited by M. Sucher and J. Fox, Polytechnic Press, New York, 495-546 (1963).
- [40] Collin, R.E., Foundations for Microwave Engineering, McGraw-Hill, New York, 313-325 (1966).
- [41] Gardiol, F.E., Introduction to Microwaves, Artech House Inc., Dedham MA, Second ed., 43-45 (1981).
- [42] Kajfez, D., and Hwan, E.J., "Q-Factor Measurement with Network Analyzer," *IEEE Transactions on Microwave Theory and Techniques*, 32 (7), 666-670 (1984).

- [43] Hewlett-Packard Product Note 8510-5, "Specifying Calibration Standards for the HP 8510 Network Analyzer," Palo Alto, CA, (1986).
- [44] Hewlett-Packard Product Note 8510-8, "Applying the HP 8510B TRL Calibration for Non-coaxial Measurements," Palo Alto, CA, (1987).
- [45] Chamis, C.C., "Simplified Composite Micromechanics Equations for Hygral Thermal and Mechanical Properties," *38<sup>th</sup> Annual Conference, Reinforced Plastics/ Composites Institute*, The Society of the Plastics Industry, Inc, (1983).
- [46] Mobay Product Information, Makrolon HMS-3118, Plastics and Rubber Division, Mobay Corporation, Pittsburg, PA, (1987).
- [47] Liao, S.Y., Microwave Devices and Circuits, Prentice-Hall, Englewood Cliffs, New Jersey, (1985).
- [48] Balanis, C.A., Advanced Engineering Electromagnetics, John Wiley & Sons, New York, (1989).

## APPENDIX A

### ELECTROMAGNETIC THEORY

An understanding of high frequency dielectric measurement and properties needs to be based upon the fundamentals of electromagnetic (EM) wave propagation. These fundamentals are extended to microwave frequency analytical theory and waveguide networks, which are the basis of dielectric measurement techniques. Thus, an elementary foundation of electromagnetics will be presented, including Maxwell's equations, EM wave propagation, and reflection phenomena. These principles will be used in conjunction with transmission line theory to describe rectangular waveguides and their application to dielectric property measurement.

#### A.1 Maxwell's Equations and EM Wave Propagation

Electromagnetic wave motion in free space can be described by the point form of Maxwell's equations written in terms of the electric ( $\vec{E}$ ) and magnetic ( $\vec{H}$ ) fields as [21]

$$\vec{\nabla} \times \vec{H} = \epsilon_0 \frac{\partial \vec{E}}{\partial t} \quad (\text{A.1a})$$

$$\vec{\nabla} \times \vec{E} = -\mu_0 \frac{\partial \vec{H}}{\partial t} \quad (\text{A.1b})$$

$$\vec{\nabla} \cdot \vec{E} = 0 \quad (\text{A.1c})$$

$$\vec{\nabla} \cdot \vec{H} = 0 \quad (\text{A.1d})$$

where  $\epsilon_0$  = free space permittivity  
 $\mu_0$  = free space permeability

Equation (A.1c) and (A.1d) imply that there is no point source of electric or magnetic flux in free space, i.e. that no electrical point charges (or magnetic monopoles) are present. Equation (A.1a) states that as the electric field changes with time at a point, a magnetic field exists in a

closed circulating loop about the  $\vec{E}$  field lines, as prescribed by the curl. Likewise, as  $\vec{H}$  varies with time, a closed circulating  $\vec{E}$  field loop forms about the  $\vec{H}$  field lines, as prescribed by Equation (A.1b). The coupled nature of these equations leads to propagation: as  $\vec{E}$  changes in time,  $\vec{H}$  correspondingly changes, generating a changing  $\vec{E}$  some distance away from the original point. This progression can be described as a wave phenomenon with a definable velocity.

Assume that the time variation of the EM fields is sinusoidal as (using only the  $E_x$  component for simplicity):

$$E_x = E(x, y, z) \cos(\omega t + \psi) \quad (\text{A.2})$$

where  $E(x, y, z)$  = real valued electric field magnitude  
 $\omega$  = circular frequency  
 $\psi$  = a phase angle

If Euler's identity

$$e^{j\omega t} = \cos \omega t + j \sin \omega t$$

is employed and only the real part of  $E_x$  considered, Equation (A.2) becomes

$$\begin{aligned} E_x &= \text{Re}[E(x, y, z) e^{j(\omega t + \psi)}] \\ &= \text{Re}[E(x, y, z) e^{j\psi} e^{j\omega t}] \end{aligned} \quad (\text{A.3})$$

The phasor form ( $E_{xs}$ ), denoted by the subscript "s", is obtained by suppressing  $e^{j\omega t}$  as

$$E_{xs} = E(x, y, z) e^{j\psi} \quad (\text{A.4})$$

Note that a time derivative of Equation (A.3) results in only an additional factor of  $j\omega$ . Making use of this fact, Equations (A.1 a-d) can be written in a phasor-vector form as

$$\vec{\nabla} \times \vec{H}_s = j\omega\epsilon_0 \vec{E}_s \quad (\text{A.5a})$$

$$\vec{\nabla} \times \vec{E}_s = -j\omega\mu_0 \vec{H}_s \quad (\text{A.5b})$$

$$\vec{\nabla} \cdot \vec{E}_s = 0 \quad (\text{A.5c})$$

$$\vec{\nabla} \cdot \vec{H}_s = 0 \quad (\text{A.5d})$$

Taking the curl of Equation (A.5b) leads to

$$\vec{\nabla} \times \vec{\nabla} \times \vec{E}_s = -j\omega\mu_0 \vec{\nabla} \times \vec{H}_s = \vec{\nabla}(\vec{\nabla} \cdot \vec{E}_s) - \nabla^2 \vec{E}_s$$

where the third term is a standard expansion of the first term. Using Equation (A.5a) this can be written

$$\nabla^2 \vec{E}_s = -\omega^2 \mu_0 \epsilon_0 \vec{E}_s \quad (\text{A.6})$$

since  $\vec{\nabla} \cdot \vec{E}_s = 0$  from Equation (A.5c). Equation (A.6) is the wave, or vector Helmholtz, equation.

Solutions of Equation (A.6) describe the electric field in time and space. In order to simplify further analysis, assume only z-direction spatial variation of the x-direction field component  $E_{xs}$ , which leads to the second order ordinary differential equation

$$\frac{d^2 E_{xs}}{dz^2} = -\omega^2 \mu_0 \epsilon_0 E_{xs} \quad (\text{A.7})$$

Solutions of this equation have the form

$$E_{xs} = A e^{-j\omega\sqrt{\mu_0\epsilon_0} z} \quad (\text{A.8})$$

which, upon introduction of  $e^{j\omega t}$  and extraction of the real component, leads to

$$E_x = E_{x0} \cos\left[\omega\left(t - z\sqrt{\mu_0\epsilon_0}\right)\right] \quad (\text{A.9})$$

where  $E_{x0}$  is the electric field amplitude at  $z = 0$  and  $t = 0$ . Equation (A.9) is a plane wave of constant phase, when

$$\omega\left(t - z\sqrt{\mu_0\epsilon_0}\right) = \text{const.} \quad (\text{A.10})$$

Differentiation reduces Equation (A.10) to

$$\frac{dz}{dt} = \frac{1}{\sqrt{\mu_0\epsilon_0}} = c \quad (\text{A.11})$$

which is the phase velocity of the plane wave;  $c$  is the speed of light. At time  $t = 0$ , the period of the cosine wave along the  $z$  axis is

$$\frac{\omega \lambda}{c} = 2\pi$$

therefore

$$\lambda = c \frac{2\pi}{\omega} = \frac{c}{f} \quad (\text{A.12})$$

which defines the free space wavelength  $\lambda$  and the frequency  $f$ .

A description of magnetic field propagation is now required. Referring back to Maxwell's equations, Equation (A.5b) can be used in conjunction with the  $x$ -direction electric field component of Equation (A.9) which varies spatially only with  $z$ . Taking the curl of  $\vec{E}_s$  under these conditions gives

$$\frac{\partial E_{xs}}{\partial z} = -j \omega \mu_0 H_{ys} \quad (\text{A.13})$$

and substitution of  $E_{xs}$  from Equation (A.8) results in the time domain equation

$$H_y = E_{x0} \sqrt{\frac{\epsilon_0}{\mu_0}} \cos\left[\omega\left(t - \frac{z}{c}\right)\right] \quad (\text{A.14})$$

The ratio of  $E_x$  to  $H_y$  holds some physical significance. The fundamental form of Ohm's Law states that

$$V = I R$$

where      V = voltage  
             I = current  
             R = resistance

Considering  $E_x$  and  $H_y$  as analogs to V and I respectively, the ratio of  $E_x$  to  $H_y$  is therefore an impedance (the complex form of resistance). Dividing Equation (A.9) by Equation (A.14) gives

$$\frac{E_x}{H_y} = \sqrt{\frac{\mu_0}{\epsilon_0}} \equiv \eta_0 \quad (\text{A.15})$$

where  $\eta_0$  is the intrinsic impedance of free space. Furthermore it can be shown, since  $\mu_0$  and  $\epsilon_0$  are known constants, that  $\eta_0 \approx 120 \pi$  Ohms.

Note that  $E_x$  and  $H_y$  are in phase and lie in a plane normal to the z-direction of propagation. Hence this is designated to be a transverse electromagnetic (TEM) wave.

## A.2 Propagation in Dielectrics

In ideal EM wave propagation through free space, all of the energy in the wave is conserved. The same wave, when traveling through any real dielectric material, will undergo energy dissipation and will experience a change in propagation behavior. This is due to the complex permittivity difference between free space (or dry air) and condensed matter.

The complex permittivity is a tensor quantity that relates the current density  $\vec{J}_s$  and the electric field  $\vec{E}_s$  as

$$\vec{\nabla} \times \vec{H}_s = \vec{J}_s = j\omega\epsilon_0 [\epsilon^*] \vec{E}_s \quad (\text{A.16})$$

where  $[\epsilon^*]$  is the permittivity tensor. Note that Equation (A.16) is merely a generalized form of Equation (A.5a) with

the introduction of current density. To illustrate this equation consider a rod of material with an imposed electric field (or voltage) driving a current flow through the cross-section (current density) and generating a closed circular magnetic field about the rod. If the rod has some appreciable electrical conductivity  $\sigma$ , then the resulting conduction current density  $\vec{J}_{sc}$  is

$$\vec{J}_{sc} = \sigma \vec{E}_s \quad (\text{A.17})$$

where an isotropic material conductivity  $\sigma$  has been assumed. A dielectric rod having negligible free charge conductivity would experience a current density due to the frequency dependent displacement of bound charges within the material, hence a displacement current  $\vec{J}_{sd}$  can be defined in a form similar to that of Equation (A.16):

$$\vec{J}_{sd} = j\omega\epsilon_0(\epsilon' - j\epsilon'') \vec{E}_s \quad (\text{A.18})$$

In Equation (A.18) the real part of the permittivity  $\epsilon'$  is the relative dielectric constant that represents the energy storage capacity of the material. The relative dielectric loss factor  $\epsilon''$  is the imaginary part of the permittivity that characterizes the electrical energy conversion to heat. Now assume a rod of arbitrary composition. The total current density  $\vec{J}_{st}$  including both free charge conductivity current  $\vec{J}_{sc}$  and displacement current density  $\vec{J}_{sd}$  can be written

$$\begin{aligned} \vec{J}_{st} &= \vec{J}_{sc} + \vec{J}_{sd} \\ &= j\omega\epsilon_0 \left( \epsilon' - j \left[ \epsilon'' + \frac{\sigma}{\omega\epsilon_0} \right] \right) \vec{E}_s \\ &= j\omega\epsilon_0 (\epsilon' - j\epsilon''_{eff}) \vec{E}_s \\ &= j\omega\epsilon_0 \epsilon^* \vec{E}_s \end{aligned} \quad (\text{A.19})$$

where all loss mechanisms are combined in the effective dielectric loss factor  $\epsilon''_{\text{eff}}$ . This form of the permittivity can be physically measured and is, in general, a function of frequency.

Now that complex permittivity is defined, wave propagation through a general material can be described. A phase constant  $\beta$  and an attenuation constant  $\alpha$  can be defined in an x-component electric field equation similar to Equation (A.9):

$$E_x = E_{x0} e^{-\alpha z} \cos(\omega t - \beta z) \quad (\text{A.20a})$$

or in phasor notation

$$\begin{aligned} E_{xs} &= E_{x0} e^{-\alpha z} e^{-j\beta z} \\ &= E_{x0} e^{-\gamma z} \end{aligned} \quad (\text{A.20b})$$

The propagation constant  $\gamma$  has been introduced to account for both the attenuation due to energy dissipation and the constant phase propagation of energy, in the complex form

$$\gamma = \alpha + j\beta \quad (\text{A.21})$$

Since these constants describe the behavior of the EM wave in space, they can be posed in terms of material properties of the medium. Equation (A.20b) can be substituted into a form of Equation (A.7) that has been generalized to an arbitrary homogeneous medium

$$\begin{aligned} \frac{d^2 E_{xs}}{dz^2} &= -\omega^2 \mu \epsilon^* E_{xs} \\ \gamma^2 E_{x0} e^{-\gamma z} &= -\omega^2 \mu \epsilon^* E_{x0} e^{-\gamma z} \\ \gamma^2 &= -\omega^2 \mu \epsilon^* \end{aligned} \quad (\text{A.22})$$

If the form of the permittivity  $\epsilon^*$  is substituted from Equation (A.19), Equation (A.22) can be solved for  $\gamma$  as

$$\begin{aligned}
\gamma &= j\omega\sqrt{\mu\epsilon_0(\epsilon' - j\epsilon''_{\text{eff}})} \\
&= j\omega\sqrt{\mu\epsilon_0\epsilon' - j\mu\epsilon_0\left(\epsilon''_d + \frac{\sigma}{\omega\epsilon_0}\right)}
\end{aligned}
\tag{A.23}$$

Note that if dielectric loss  $\epsilon''_d$  and conductivity  $\sigma$  are small, then the medium can be considered lossless:  $\alpha = 0$  and  $\beta = \omega\sqrt{\mu\epsilon'}$ . No energy would be dissipated in such a material by a propagating EM wave. Low-loss dielectrics are usually considered to be insulators ( $\sigma \approx 0$ ) with small  $\epsilon''$ . A non-zero  $\epsilon''$  means that energy is still dissipated in the medium as a decaying exponential in space since  $\alpha \neq 0$  in Equation (A.20b); this is an important concept in dielectric heating of thick materials.

The y-component of the magnetic field in the dielectric can be obtained using arguments similar to those in Equations (A.13) and (A.14), but with  $E_{xs}$  from (A.20b) yielding

$$H_{ys} = \frac{E_{x0}}{\eta} e^{-\alpha z} e^{-j\beta z} \tag{A.24}$$

where the general complex intrinsic impedance  $\eta$  is given by

$$\begin{aligned}
\eta &\equiv \frac{E_x}{H_y} = \sqrt{\frac{\mu}{\epsilon^*}} \\
&= \sqrt{\frac{\mu}{(\epsilon' - j\epsilon''_{\text{eff}})}} \\
&= \sqrt{\frac{\mu}{\left(\epsilon' - j\left[\epsilon''_d + \frac{\sigma}{\omega\epsilon'}\right]\right)}}
\end{aligned}
\tag{A.25}$$

In a lossy material, where  $\epsilon''_d$  and  $\sigma$  add a complex component to  $\eta$ , the electric and magnetic fields are no longer in time

phase. Only in a lossless material with  $\epsilon''_d \approx \sigma \approx 0$  are  $\eta$  real and the EM fields in phase.

At this point, a question of engineering concern might be "What quantity provides the criterion for the 'low loss' assumption?" The answer can be found in the ratio of the imaginary to the real part of the total current density in Equation (A.19). This ratio is defined as the loss tangent  $\tan \delta$ :

$$\tan \delta = \frac{\epsilon''_{\text{eff}}}{\epsilon'} = \frac{\epsilon''_d + \frac{\sigma}{\omega \epsilon'}}{\epsilon'} \quad (\text{A.26})$$

The angle  $\delta$ , as illustrated in Figure A.1, is the amount that the conservative current component ( $\omega \epsilon_0 \epsilon' E$ ), due to lossless propagation of  $\vec{E}_s$  through a material of permittivity  $\epsilon'$ , leads the phase of the total current  $\vec{J}_{st}$ . The phase lag of  $\vec{J}_{st}$  is a direct measure of the strength of the energy dissipation mechanisms in the material, due to both conductivity ( $\sigma$ ) and displacement of bound charges ( $\epsilon''_d$ ). Thus,  $\tan \delta$  provides a guide to the engineer in making the "low-loss" assumption: the closer  $\tan \delta$  is to 0, the smaller the loss.

### A.3 Power and Poynting's Theorem

Power flow and dissipation are of central importance to engineering the EM heating of materials and in understanding dielectric measurement techniques. Poynting's theorem, which is essentially a power balance equation, can be derived from Maxwell's equations; this derivation is easily followed in elementary texts [21,33] and is therefore omitted here. An inspection of the final Poynting's theorem equation provides sufficient insight for the derivations that follow.

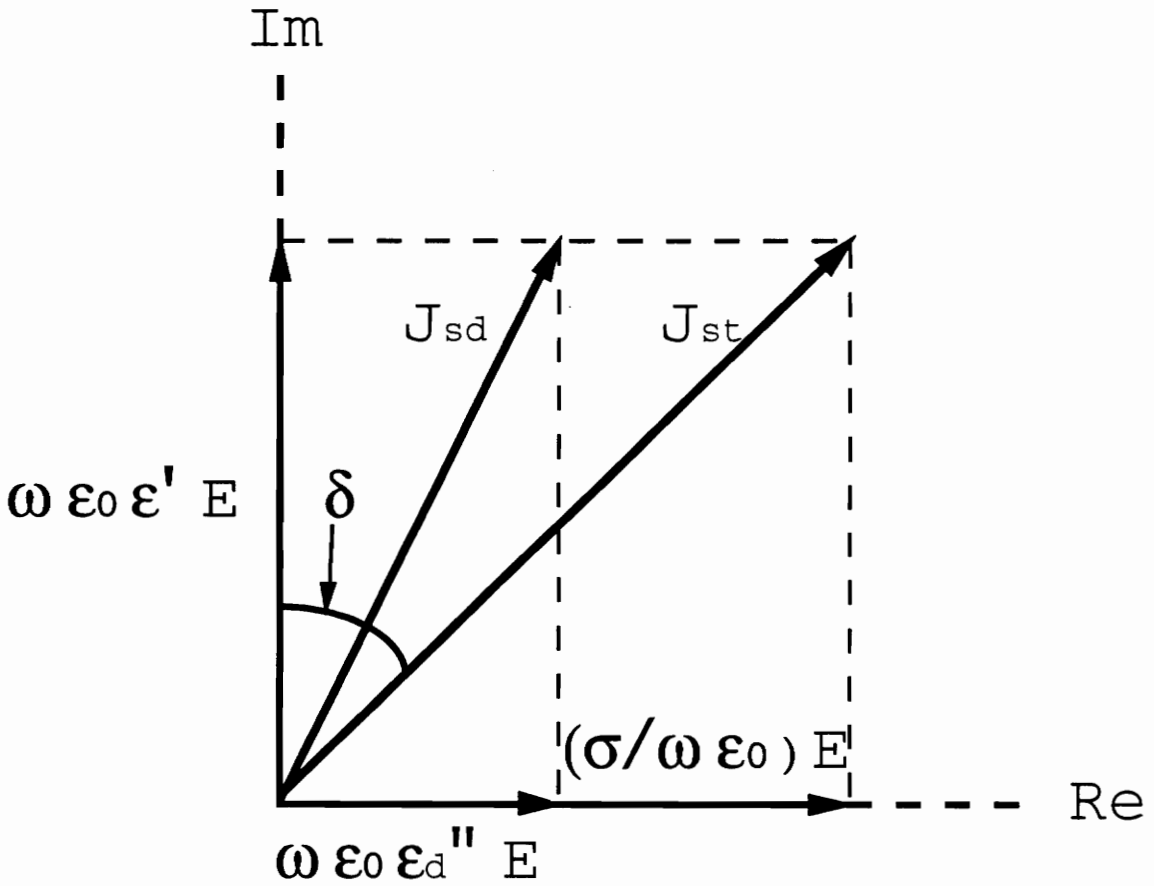


Figure A.1: Current density and electric field vectors with corresponding permittivity and conductivity related components. [13]

If an arbitrary volume  $V$  enclosed by surface  $S$  is assumed to contain no source currents, then Poynting's theorem states

$$\begin{aligned}
 -\int_S (\vec{E} \times \vec{H}) \cdot d\vec{s} &= \sigma \int_V |\vec{E}|^2 dV \\
 +\omega \int_V (\epsilon_d'' |\vec{E}|^2 + \mu'' |\vec{H}|^2) dV &+ j\omega \int_V (\mu' |\vec{H}|^2 - \epsilon' |\vec{E}|^2) dV
 \end{aligned}
 \tag{A.27}$$

The surface integral on the left side of Equation (A.27) represents the complex power flow out the closed volume; the sign change implies power influx. The quantity  $\vec{S} = \vec{E} \times \vec{H}$ ,

known as the Poynting vector, can be interpreted as the direction of instantaneous power flow. It follows that an EM wave with only  $E_x$  and  $H_y$  components will propagate power in the  $z$ -direction.

The first and second integrals on the right side of Equation (A.27) represent first the conductive, then the dielectric and magnetic dissipation. It should be pointed out that magnetic dissipation is appreciable only in ferromagnetic materials. These power losses represent the mechanisms responsible for EM heating. Note that while the conductive loss term does not explicitly depend upon frequency,  $\sigma$  is often a strong function of frequency. The dielectric loss power integral term depends explicitly upon frequency.

The final integral on the right side represents energy stored in the volume  $V$  by electric and magnetic fields. This term can be separated into often used, more common forms of time averaged energy storage equations

$$U_E = \frac{\epsilon'}{4} \int_V |\bar{E}|^2 dV \quad (\text{A.28a})$$

$$U_H = \frac{\mu'}{4} \int_V |\bar{H}|^2 dV \quad (\text{A.28b})$$

The complex power balance can be qualitatively stated as follows: the complex power flowing into a volume is either stored in electric or magnetic fields or is dissipated by conductive, dielectric, or ferromagnetic mechanisms.

#### **A.4 Plane Wave Reflection (Normal Incidence)**

The propagation of EM waves and the associated power storage and dissipation characteristics of general media have been discussed in previous sections. Any transitions between materials possessing different properties, such as air/dielectric or dielectric/dielectric interfaces, give rise

to reflections. A basic description of how material properties are related to reflection and transmission of EM waves will be given.

Recall the plane EM wave of Equations (A.20b) and (A.24) traveling in the positive  $z$  direction, and having only  $E_{xs}$  and  $H_{ys}$  components. Now consider this wave, propagating through free space, incident upon a lossy medium as shown in Figure A.2. Let the planar interface between the two media be at  $z = 0$ . The incident fields can be written ( $z < 0$ )

$$E_{xi} = E_{x0} e^{-j\beta_0 z} \quad (\text{A.29a})$$

$$H_{yi} = \frac{E_{x0}}{\eta_0} e^{-j\beta_0 z} \quad (\text{A.29b})$$

where  $\eta_0$  is the intrinsic impedance of free space and  $\beta_0$  is the phase constant of free space ( $\beta_0 = \omega\sqrt{\mu_0\epsilon_0}$ ). A reflected wave may also exist in the region  $z < 0$ ; the fields can be described by defining the electric field reflection coefficient  $\Gamma$  in the equations

$$E_{xr} = \Gamma E_{x0} e^{+j\beta z} \quad (\text{A.30a})$$

$$H_{yr} = \frac{-\Gamma}{\eta_0} E_{x0} e^{+j\beta z} \quad (\text{A.30b})$$

Note the positive exponential propagation terms, representing waves traveling in the negative  $z$  direction. The change in propagation direction necessitates the negative sign in Equation (A.30b) since the magnetic fields must satisfy the current-free boundary condition at the interface [48]. The reflected wave carries away a portion of the incident wave's energy, with the balance of the energy continuing to propagate through the lossy medium. These waves transmitted across the interface ( $z < 0$ ) can be described by the fields

$$E_{xt} = T_r E_{x0} e^{-\gamma_1 z} \quad (\text{A.31a})$$

$$H_{yt} = \frac{T_r}{\eta_1} E_{x0} e^{-\gamma_1 z} \quad (\text{A.31b})$$

where  $T_r$  is the electric field transmission coefficient, and  $\eta_1$  and  $\gamma_1$  are the complex intrinsic impedance and complex propagation constant of the medium, respectively.

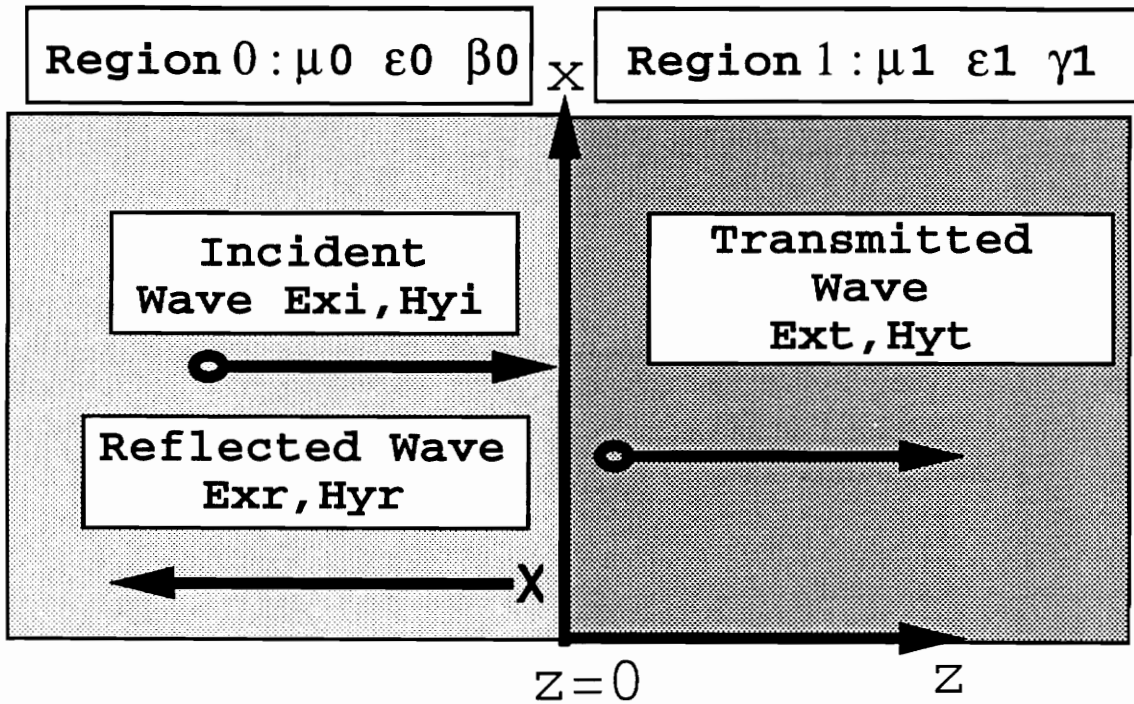


Figure A.2: Electromagnetic plane wave transmission and reflection from a planar interface.

The boundary value problem at the interface can now be solved for  $\Gamma$  and  $T_r$  by applying continuity requirements on the tangential field components. At  $z = 0$ , continuity of  $E_x$  implies that Equations (A.29a) and (A.30a) must sum to equal (A.31a); when divided by  $E_{x0}$  this yields

$$1 + \Gamma = T_r \quad (\text{A.32a})$$

Likewise, continuity of  $H_y$  in Equations (A.29b), (A.30b), and (A.31b) yields

$$\frac{1 - \Gamma}{\eta_0} = \frac{T_r}{\eta_1} \quad (\text{A.32b})$$

These two equations can be solved simultaneously, resulting in

$$\Gamma = \frac{\eta_1 - \eta_0}{\eta_1 + \eta_0} \quad (\text{A.33a})$$

$$T_r = \frac{2\eta_1}{\eta_1 + \eta_0} \quad (\text{A.33b})$$

### A.5 Standing Wave Ratio and Input Impedance

Reflection and transmission effects can be generalized to the interface of any two media, thus the intrinsic impedances in Equations (A.33a) and (A.33b) could be complex. This would lead to  $\Gamma$  being a complex quantity that is expressed as

$$\Gamma = |\Gamma| e^{j\phi} \quad (\text{A.34})$$

where  $|\Gamma|$  = the reflection magnitude  $0 \leq |\Gamma| \leq 1$

$\phi$  = the phase shift in the reflected wave

Note that the phase shift  $\phi$  arises from the relationships between the complex impedances of the two media [21]. The form of  $\Gamma$  in Equation (A.34) can be used in the analysis of the waves in the half space  $z < 0$  of Figure A.2. Summing Equations (A.29a) and (A.30a), and introducing Equation (A.34), results in

$$E_{xi} = E_x(z < 0) = \left[ e^{-j\beta_0 z} + |\Gamma| e^{j(\beta_0 z + \phi)} \right] E_{x0} \quad (\text{A.35})$$

The maximum value that the electric field in Equation (A.35) can have is

$$E_{xi,max} = e^{j\frac{\phi}{2}}(1 + |\Gamma|) E_{x0} \quad (A.36a)$$

which occurs where both of the propagation exponential terms in Equation (A.35) have the same phase [21]:

$$\begin{aligned} -\beta_0 z_{min} &= \beta_0 z_{min} + \phi + 2n\pi \\ &= \frac{\phi}{2} + n\pi \end{aligned} \quad (A.36b)$$

where  $n$  is any integer. Conversely, the electric field minima

$$E_{xi,min} = je^{j\frac{\phi}{2}}(1 - |\Gamma|) E_{x0} \quad (A.37a)$$

occur where the propagation exponential terms in Equation (A.35) have phase angles  $180^\circ(\pi$  radians) apart

$$\begin{aligned} -\beta_0 z_{max} &= -\beta_0 z_{max} + \phi + 2n\pi + \pi \\ &= \frac{\phi}{2} + n\pi + \frac{\pi}{2} \end{aligned} \quad (A.37b)$$

The ratio of the maximum to minimum electric fields is defined as the standing-wave ratio ( $s$ ):

$$s = \frac{E_{xi,max}}{E_{xi,min}} = \frac{1 + |\Gamma|}{1 - |\Gamma|} \quad (A.38)$$

Equations (A.36b) and (A.37b) imply that minima and maxima repeat at intervals of  $n\pi$ , or one-half of a sinusoidal period, thus at one-half wavelength of the EM wave. Furthermore, maxima and minima are separated by an angle of  $\pi/2$ , as expected in a rectified sine wave.

If an incident wave is partly reflected at a surface and partly transmitted into the second medium, then both a standing wave (resulting from the reflection) and a traveling wave (the component that crosses the interface) will be supported in the medium of incidence [21]. Standing waves

can be interpreted as sinusoidal,  $\sin(\beta z - \omega t)$ , in form, while traveling waves possess an exponential,  $e^{j(\omega t - \beta z)}$ , propagation form. These two waves are, in general, out of phase. Therefore, there will be non-zero values of  $E_{xi}$  at minimum points. The standing-wave ratio quantifies the magnitude of the wave resulting from the combined standing and traveling waves.

The analysis of reflection and standing waves having periodic maxima and minima leads to the question "How are the electric and magnetic fields described in space relative to the interface?" The electric ( $E_{xI}$ ) and magnetic ( $H_{yI}$ ) fields in medium I at a distance  $z = -\ell$  from the interface are, recalling Equation (A.35),

$$E_{xI} = \left( e^{-j\beta_I \ell} + \Gamma e^{j\beta_I \ell} \right) E_{x0} \quad (\text{A.39a})$$

$$H_{yI} = \left( e^{j\beta_I \ell} - \Gamma e^{-j\beta_I \ell} \right) \frac{E_{x0}}{\eta_I} \quad (\text{A.39b})$$

where  $\beta_I$  and  $\eta_I$  are the propagation phase constant and intrinsic impedance of medium I. The intrinsic impedance "looking in" toward the interface from  $z = -\ell$ , the input intrinsic impedance ( $\eta_{in}$ ), is defined by

$$\eta_{in} = \left. \frac{E_{xI}}{H_{yI}} \right|_{z=-\ell} = \eta_I \frac{e^{j\beta_I \ell} + \Gamma e^{-j\beta_I \ell}}{e^{j\beta_I \ell} - \Gamma e^{-j\beta_I \ell}} \quad (\text{A.40})$$

Recalling  $\Gamma$  from Equation (A.33a) and Euler's identity, Equation (A.40) becomes

$$\begin{aligned} \eta_{in} &= \eta_I \left[ \frac{(\eta_{II} + \eta_I)(\cos \beta_I \ell + j \sin \beta_I \ell) +}{(\eta_{II} + \eta_I)(\cos \beta_I \ell + j \sin \beta_I \ell) -} \right. \\ &\quad \left. \frac{(\eta_{II} - \eta_I)(\cos \beta_I \ell - j \sin \beta_I \ell)}{(\eta_{II} - \eta_I)(\cos \beta_I \ell - j \sin \beta_I \ell)} \right] \\ &= \eta_I \left[ \frac{\eta_{II} + j \eta_I \tan \beta_I \ell}{\eta_I + j \eta_{II} \tan \beta_I \ell} \right] \end{aligned} \quad (\text{A.41})$$

Where  $\eta_{II}$  is the intrinsic impedance of medium II. Note that when  $\eta_{II} = \eta_I$ ,  $\eta_{in} = \eta_I$  and there is no reflection; this is considered to be a "matched" condition. In the case of  $\eta_{II} = 0$ , (a perfect conductor),  $\eta_{in} = j \eta_I \tan \beta_I \ell$ . When  $\beta_I \ell = n\pi$ ,  $\eta_{in} = 0$ , thus  $E_{xI} = 0$ ; this is the location of an electric field null.

## A.6 Transmission Line Theory

In previous sections the analysis of EM plane waves applies to all frequencies, not just microwave frequencies. Where microwave frequency analysis departs from that of lower frequencies is in circuit and network modeling. Classical circuit theory is based upon "lumped-elements", or elements assumed to have very small dimensions relative to the wavelength of operation. Lumped-element circuits are time dependent only, with spatial separation and component dimensions neglected. Thus, all elements in parallel see the same voltage instantaneously and all components in series have the same current flowing through them at any moment in time.

Microwave frequency analysis, however, involves wavelengths on the same order as typical waveguide components. At 3 GHz the wavelength in freespace is 10 cm, shorter than most waveguide systems at that frequency. In such a case, the voltages in a 1 meter long waveguide would depend both upon time and position. Transmission line theory provides a means by which classical circuit theory concepts and formalisms can be coupled with plane wave EM field theory.

Instead of lumped-elements, the transmission line is assumed to contain distributed-parameters, that is, circuit elements defined per unit length. A typical small but finite length of transmission line is shown in Figure A.3. The length of this section is  $\Delta z$ , phasor voltage ( $V_S$ ) and current

( $I_s$ ) exist on the left end, while the same voltage and current changed by  $\Delta V_s$  and  $\Delta I_s$ , respectively, exist on the right end. The distributed parameters are defined as:

R = series resistance per unit length

L = series inductance per unit length

G = shunt conductance per unit length

C = shunt capacitance per unit length

Physically, L and C represent magnetic and electric field storage in a system, respectively, while R accounts for conductive impedance and loss, and G stands for dielectric loss in the material between the conductors. Kirchhoff's voltage law, when applied to the perimeter of the circuit in Figure A.3, leads to

$$V_s - R\Delta z I_s - L\Delta z \frac{dI_s}{dt} - (V_s + \Delta V_s) = 0 \quad (\text{A.42a})$$

and Kirchhoff's current law, when summed at node A, yields

$$I_s - C\Delta z \frac{d(V_s + \Delta V)}{dt} - G\Delta z (V_s + \Delta V_s) - (I_s + \Delta I_s) = 0 \quad (\text{A.42b})$$

Dividing Equations (A.42a) and (A.42b) by  $\Delta z$ , then taking the limit as  $\Delta z \rightarrow 0$  (therefore  $\Delta V_x$  and  $\Delta I_s$  both vanish), leads to the differential equations

$$\frac{dV_s}{dz} = -RI_s - L \frac{dI_s}{dt} = -(R + j\omega L) I_s \quad (\text{A.43a})$$

$$\frac{dI_s}{dz} = -GV_s - C \frac{dV_s}{dt} = -(G + j\omega C) V_s \quad (\text{A.43b})$$

Where time dependence of the voltage and current have been assumed to be sinusoidal i.e., they vary as  $e^{-j\omega t}$ .

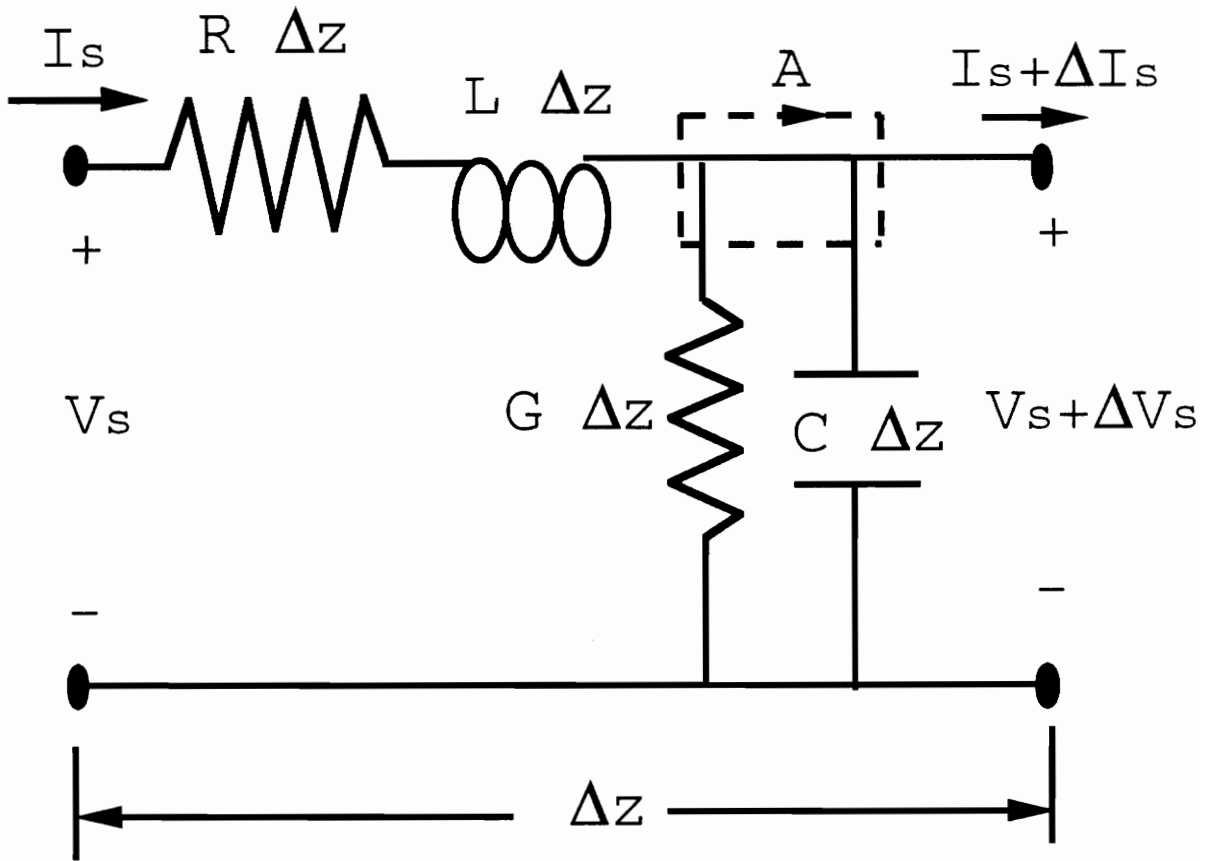


Figure A.3: Section of a lumped element transmission line.

Equations (A.43a) and (A.43b) are directly analogous to the one-dimensional results of Maxwell's curl equations in phasor form Equations (A.5a) and (A.5b) with conductivity:

$$\frac{dE_{xs}}{dz} = -j\omega\mu H_{ys} \quad (\text{A.44a})$$

$$\frac{dH_{ys}}{dz} = -(\sigma + j\omega\epsilon) E_{xs} \quad (\text{A.44b})$$

The analogy between Equations (A.43a) and (A.44a) associates  $V_s$  and  $E_{xs}$ , and  $L$  and  $\mu$ . The transmission line model includes  $R$ , which is not found in the form of the Maxwell's equations. The resistance  $R$  is analogous to field penetration into a real conductor and would require a separate application of

Maxwell's equations and satisfaction of boundary conditions. The transmission line analogy can be maintained, including the resistance  $R$ , by replacing  $j\omega\mu$  in (A.44a) with  $(R + j\omega L)$  [21]. In a similar manner, Equations (A.43b) and (A.44b) contain analog pairs:  $I_s$  and  $H_{ys}$ ,  $G$  and  $\sigma$ , and  $C$  and  $\epsilon$ .

The voltage  $V_s$  can be thought of as a propagating plane wave, analogous to  $E_{xs}$  in Equation (A.20b), as

$$V_s = V_0 e^{-\gamma z} \quad (\text{A.45})$$

A corresponding propagation constant can be defined, following Equation (A.23), as

$$\gamma = \sqrt{(R + j\omega L)(G + j\omega C)} \quad (\text{A.46})$$

The analog to intrinsic impedance  $\eta$  can be defined as the characteristic impedance  $Z_0$  of the transmission line where

$$I_s = \frac{V_0}{Z_0} e^{-\gamma z} \quad (\text{A.47})$$

Thus

$$Z_0 = \sqrt{\frac{j\omega\mu}{\sigma + j\omega\epsilon}} = \sqrt{\frac{R + j\omega L}{G + j\omega C}} \quad (\text{A.48})$$

Reflections from interfaces having different characteristic impedances are analogous to reflection phenomena discussed previously. Thus, following Equations (A.33a) and (A.33b), reflection ( $\Gamma$ ) and transmission ( $T_r$ ) coefficients can be written

$$\Gamma = \frac{Z_{02} - Z_{01}}{Z_{02} + Z_{01}} \quad (\text{A.49a})$$

$$T_r = \frac{2Z_{02}}{Z_{02} + Z_{01}} \quad (\text{A.49b})$$

Where  $Z_{01}$  and  $Z_{02}$  are the characteristic impedances of the media of incidence and transmission, respectively. Finally,

the input impedance ( $Z_{in}$ ) at  $z = -\ell$  of a transmission line or propagation constant  $\beta$  is analogous to the intrinsic input impedance  $\eta_{in}$  of Equation (A.41), and is written

$$Z_{in} = Z_0 \left[ \frac{Z_L + jZ_0 \tan \beta \ell}{Z_0 + Z_L \tan \beta \ell} \right] \quad (A.50)$$

Where  $Z_0$  is the characteristic impedance in Equation (A.48) and  $Z_L$  is the impedance representing the load on the transmission line, such as an antenna, emitter, or as in this work, a resonant cavity.

## APPENDIX B

### PROGRAM LISTINGS

#### B.1 Reflection Cavity Program

```
(* ----- PROGRAM "REFLECT" -----  
This Mathematica program computes the complex permittivity  
of a material given the Q and resonant frequency data  
from a reflection cavity system measurement of a dielectric  
material of known thickness.
```

The program prompts the user to choose between the WR-430 (LS-Band) and WR-90 (X-Band) waveguide cavities.

The user will be prompted to enter the empty cavity Q and fr, the sample loaded Q and fr, and the sample thickness.

The solution for the first root of the transcendental equation of interfacial impedances has a built in initial guess of 0.5. This guess has been found to be stable for low-loss materials of thickness around 1/4".

```
-----*)
```

```
(* ----- Select the Cavity Type Being Used ----- *)  
choose= Input[" Which measurement frequency?  
WR-430 = '1'  
WR-90 = '2' "];  
  
If[choose==1,  
  (*----- WR 430 Parameters --[cm]-----*)  
  a= 10.922 ;b= 5.461 ;  
  fc=1.372*10^9 (* cutoff frequency [Hz] *);  
  Print[ "You are using the WR-430 system, right?"]  
  
  ,If[choose==2,  
    (*----- WR 90 DIMENSIONS --[cm]-----*)  
    a= 2.286 ;b= 1.016 ;  
    fc=6.557*10^9 (* cutoff frequency [Hz] *);  
    Print[ "You are using the WR-90 system, right?"]  
  ,Print[ " Pick 1 or 2 only ! Interrupt and restart."]  
  ]  
];  
  
(*----- Input Q's and Resonant Frequencies ----*)  
Quo=Input["Enter Quo, the empty cavity Q"];  
fro=10^9*Input["Enter fro, the empty cavity resonant  
frequency [GHz]"];  
Qu1=Input["Enter Qu1, the filled cavity Q"];
```

```

fr1=10^9*Input["Enter fr1, the filled cavity resonant
frequency [GHz]"];
le=2.54*Input["Enter the sample thickness [cm]"];

(*----- Echo Entries -----*)
Print["Quo=",Quo];
Print["fro=",fro," [Hz]"];
Print["Qu1=",Qu1];
Print["fr1=",fr1," [Hz]"];
Print["Sample Length=",le," [cm]"];

(*----- Constants -----*)
c=2.998 10^10 ;(* light speed in free space [cm/s]*)
ho=376.7 ;(*intrinsic impedance [Ohms]*)
muo=4 Pi 10^(-9) ;(*free space permeability [H/cm]*)

(*----- Computing Length of Cavity -----*)
lamda=c/fro; (* free space wavelength [cm]*)
lamdag= (lamda/Sqrt[1-(fc/fro)^2]);(* guide wavelength
[cm]*)
lm=(3 lamdag/2); (* cavity length neglecting iris [cm]*)

(*----- Variables For e' Computation -----*)
lamc=2 a; (* cutoff wavelength [cm] *)
lo=lm-le; (* cavity length from iris to specimen face [cm]*)
krl=2 Pi Sqrt[fr1^2 -(c/lamc)^2]/c;(*propagation constant
[1/cm]*)
d=lm/3 ;(* one mode length [cm] *)

(*----- Resetting Variables -----*)
x=.;
xe=.;

(*----- Solve Transcendental Eqn.for ker1 ---*)
kx= -Tan[krl lo]/(krl le);
xe=x/.(FindRoot[Tan[x]/x ==kx,{x,.5},MaxIterations->20]);
ker1= xe/le; (* prop. const. for dielectric material*)

(*----- Dielectric Constant e' -----*)
e'=(c/fr1)^2 ((1/lamc^2) + (xe/(2 Pi le))^2 )//N;

(*----- Impedances -----*)
zro= 2 fro muo lm/3;
zrl= 2 Pi fr1 muo/krl;
zer1= 2 Pi fr1 muo/ker1;

(* ----- Wavelengths -----*)
lamro= c/fro;
lamr1= c/fr1;
lamer1= lamr1/Sqrt[e'];

```

he=ho/Sqrt[e']; (\*intrinsic impedance of specimen\*)

(\* --- Integration Results for Energy Terms ---\*)

```
s1= lo/2 - Sin[2 kr1 lo]/(4 kr1);
s2= lo/2 + Sin[2 kr1 lo]/(4 kr1);
s3= le/2 - Sin[2 ker1 le]/(4 ker1);
s4= le/2 + Sin[2 ker1 le]/(4 ker1);
s5= Sin[ ker1 le]^2/(2 ker1);
s6= -zro^2 (3 d/2);
s7= (3 d/2);
s8= -zr1^2 s1;
s9= s2;
s10= -( s4 zr1^2 Sin[kr1 lo]^2 +
        s3 zer1^2 Cos[kr1 lo]^2 +
        s5 zr1 zer1 Sin[2 kr1 lo] );
s11= ( s4 Cos[kr1 lo]^2 +
        s3 (zr1/zer1)^2 Sin[kr1 lo]^2 +
        s5 (zr1/zer1) Sin[2 kr1 lo] );
s12= s6;
s13= (2 +2 s7/b)-
      lamro^2 s6(1/b+2/a)/2/ho^2/a^2;
s14= s8;
s15= s10;
s16= ( 1+2 Cos[kr1 lo]^2+
      ( Cos[kr1 lo] Cos[ker1 le]-
      (zr1/zer1) Sin[kr1 lo] Sin[ker1 le])^2 )+
      2 (s9+s11)/b-
      lamr1^2 s8(1/b+2/a)/2/ho^2/a^2 -
      lamer1^2 s10(1/b+2/a)/2/he^2/a^2 ;
```

```
(*----- Loss Factor e'' -----*)
e''= (1/s15) ( (s14 +e' s15)/Qu1-
          s16 s12 Sqrt[fro/fr1]/s13/Quo )//N;
```

```
(* ---- Output the Results -----*)
Print[" e'=" ,e', " e''=" ,e'']
```

You are using the WR-90 system, right?

Quo=1532

fro=9.4577 10<sup>9</sup> [Hz]

Qu1=1126

fr1=9.3805 10<sup>9</sup> [Hz]

Sample Length=0.381[cm]

e' = 2.20659 e'' = 0.0116363

## B.2 Cavity Perturbation Program

```
(* ----- PROGRAM "PERTURB" -----  
This Mathematica program computes the complex permittivity  
of a material given the Q and resonant frequency data  
from a cavity perturbation system measurement of a dielectric  
material of known diameter.
```

The program prompts the user to choose between the WR-430 (LS-Band) and WR-90 (X-Band) waveguide cavities.

The user will be prompted to enter the empty cavity Q and fr, the sample loaded Q and fr, and the sample's effective diameter.

```
-----*)  
(* ----- Select the Cavity Type Being Used ----- *)  
choose= Input[" Which measurement frequency?  
WR-430 = '1'  
WR-90 = '2' "];  
  
If[choose==1,  
  (*----- WR 430 Parameters --[cm]-----*)  
  a= 10.922 ;  
  fc=1.372*10^9 (* cutoff frequency [Hz] *);  
  Print[ "You are using the WR-430 system, right?" ]  
  
  ,If[choose==2,  
    (*----- WR 90 DIMENSIONS --[cm]-----*)  
    a= 2.286 ;  
    fc=6.557*10^9 (* cutoff frequency [Hz] *);  
    Print[ "You are using the WR-90 system, right?" ]  
  ,Print[ " Pick 1 or 2 only ! Interrupt and restart." ]  
  ]  
];  
  
(*----- Input Q's and Resonant Frequencies ----*)  
Quo=Input["Enter Quo, the empty cavity Q"];  
fro=10^9*Input["Enter fro, the empty cavity resonant  
frequency [GHz]"];  
Qu1=Input["Enter Qu1, the filled cavity Q"];  
fr1=10^9*Input["Enter fr1, the filled cavity resonant  
frequency [GHz]"];  
d=2.54*Input["Enter the sample effective diameter [in]"];  
  
(*----- Echo Entries -----*)  
Print["Quo=", Quo];  
Print["fro=", fro, "[Hz]"];  
Print["Qu1=", Qu1];
```

```

Print["fr1=",fr1,"[Hz]"];
Print["Sample Diameter=",d,"[cm]"];

c=2.998 10^10      ;(* light speed in free space [cm/s]*)

(*----- Computing Length of Cavity -----*)
lamda=c/fro; (* free space wavelength [cm]*)
lamdag= (lamda/Sqrt[1-(fc/fro)^2]); (* guide wavelength
[cm]*)
lm=(3 lamdag/2); (* cavity length [cm]*)

(* ----- Shape factor -----*)
sf=4 a lm/Pi/d^2;

(*----- Compute the complex permittivity -----*)
e'=1+(sf/2) ( (fro-fr1)/fr1 )//N;
e''=((1/Qu1)-(1/Quo)) sf/4 //N;

(* ---- Output the Results -----*)
Print[" e'=" ,e'," e''=" ,e'']

```

You are using the WR-90 system, right?

```

Quo=2608
fro=9.45787 10^9 [Hz]

Qu1=1438
fr1=9.3124 10^9 [Hz]

Sample Diameter=0.3048[cm]

e'= 2.61458 e''= 0.0161218

```

## VITA

The author, Mitchell Lee Jackson, was born on November 26, 1965 in Portsmouth, Virginia. He lived in Chesapeake, Virginia and graduated from Deep Creek High School in 1984. He completed undergraduate studies at Virginia Polytechnic Institute and State University in 1989 and was awarded a Bachelor of Science degree in Engineering Science and Mechanics. In June 1993 he completed the requirements for a Master of Science degree in Engineering Mechanics. He is currently working toward a Ph.D. in Materials Engineering Science at Virginia Tech in the field of microwave processing of materials.

Mitchell L. Jackson